A numerical study of penetrative turbulence in convective boundary layers

by

© Mohammad Alamgir Hossain
B. Sc.(Hons), M. Sc.

A thesis submitted to the
School of Graduate Studies
in partial fulfillment of the
requirements for the degree of
Master of Science.

Department of Mathematics and Statistics
Memorial University of Newfoundland

May 2015

ST. JOHN'S NEWFOUNDLAND

Abstract

A weighted residual collocation method is investigated to study penetrative turbulence in the atmospheric boundary layer (ABL). In designing such a numerical model for the ABL, one needs to minimize or avoid artificial energy dissipation at the resolved scale, and parameterize the effect of unresolved turbulent mixing to account for the subgrid scale energy dissipation. In this research, the standard mesoscale filtering of conservation laws (mass, momentum, and energy) has been adopted based on the assumption that the characteristic scale of circulation is much less than the density scale hight of the atmosphere. Such mesoscale equations have been filtered with a Deslauriers-Dubuc (DD) interpolating wavelet system along with a Smagorinsky type eddy viscosity model. The time integration is performed by projecting the solution onto a Krylov subspace, and by solving the system with the GMRES (generalized minimal residual) algorithm. The numerical model is verified with the analytical solution of two-dimensional advection-diffusion phenomena, and with two benchmark simulations such as dry thermal rising in the neutrally stratified environment and stationary solutions of urban heat island circulation. The generation of internal waves by a turbulent buoyant element impinging upon the interface between the boundary layer and free atmosphere is characterized. Finally, penetrative turbulence due to differentially heated earth's surface is investigated for a wide range of surface heat flux variations, $25 \leq H_0 \leq 930$ W m^{-2}. Results indicate that the downscale energy cascade is associated with the onset of temporal oscillations in mesoscale circulation, although a fraction of kinetic energy is transferred by internal waves.

Acknowledgements

I would first like to thank my supervisor, Dr. Jahrul Alam for his consistent support, inspiration, and encouragement to explore new ideas throughout the duration of my study at the Memorial University of Newfoundland.

I would like to express my gratitude to the School of Graduate Studies (SGS) at Memorial University of Newfoundland, the Department of Mathematics and Statistics, and Dr. Jahrul Alam , for their financial support during my M.Sc. studies. I would also like to thank Jagannath University, Bangladesh for granting me a paid leave for the entire period of my studies in Canada.

I would like to acknowledge the Department of Mathematics and Statistics and, Memorial University of Newfoundland for high performance computing support. I would also like to acknowledge all of the members of our research group, faculty, staff, or other students at the Memorial University of Newfoundland who contributed to my learning. I am thankful to Mr. Robert Cahill for his help in proofreading the final draft.

Finally, I would like to thank my parents, my brothers and sister, and my wife for their support, love and encouragement.

Contents

List of Tables

List of Figures

Abbreviations

Symbol	Description
CFD	Computational fluid dynamics
CFL	Courant-Friedrichs-Lewy number
DD	Deslauriers & Dubuc
DNS	Direct Numerical Simulation
D & T	Dubois & Touzani (2009)
LES	Large Eddy Simulation
NSE	Navier-Stokes equations
NWP	Numerical Weather Prediction
PDE	Partial differential equation
RAMS	Regional Atmospheric Modeling System
SGS	Subgrid-scale
UHI	Urban Heat Island
WRF	Weather Research and Forecasting model

Nomenclature

Symbol	Units	Description
Independent variables		
x	m	Horizontal coordinate
z	m	Vertical coordinate
t	s	Time
Dependent variables		
$\boldsymbol{u}$	ms^{-1}	Velocity field
u	ms^{-1}	Horizontal velocity component
w	ms^{-1}	Vertical velocity component
p	hPa	Pressure
ρ	kgm^{-3}	Density
T	K	Temperature
θ	K	Potential temperature
b	ms^{-2}	Buoyancy for the dry atmosphere
E_p	$\mathrm{joule(J)}$	Potential energy
E_k	$\mathrm{joule(J)}$	Kinetic energy
E	$\mathrm{joule(J)}$	Total energy
Constants		
g	ms^{-2}	Accelaration due to gravity

θ_0	K	a reference temperature
β	Km^{-1}	Vertical gradient of synoptic-scale potential temperature
N	s^{-1}	Buoyancy frequency
K_M	$\mathrm{m}^2\mathrm{s}^{-1}$	Eddy viscosity coefficient
K_H	$\mathrm{m}^2\mathrm{s}^{-1}$	Eddy diffusivity of heat
c_p	$\mathrm{kJ/kg.K}$	Specific heat at constant pressue
p_0	hPa	Reference pressure (1000 hPa)
R	$\mathrm{Jkg}^{-1}\mathrm{K}^{-1}$	Gas constant for dry air
κ	$\mathrm{Wm}^{-1}\mathrm{K}^{-1}$	Thermal conductivity of air

Other symbols

$\Delta x, \Delta y, \Delta z$	Grid space along x, y, z-axis
ΔV	Grid volume
Δt	Time step
π	Exner function
δ_{ij}	Kronecker delta
τ_{ij}	Turbulent stresses
$\mathcal{N}$	Number of grid points
U	Velocity scale
H	Length scale
L_x	Size of the domain along x-axis
L_z	Size of the domain along z-axis
n_x	Number of grid points along x-axis
n_z	Number of grid points along z-axis

Non-dimensional parameters

Re	Reynolds number

Ra	Rayleigh number
Ri_b	Bulk Richardson number
Pr	Prandtl number
Fr	Froude number

Chapter 1

Introduction

1.1 Motivation and overall objective

This thesis investigates the problem of how a turbulent flow in the lower atmosphere penetrates into an overlying stably stratified environment (Deardorff *et al.*, 1968; Lane, 2008). This phenomenon is a characteristic of the daytime boundary layer (*i.e.* the convective boundary layer), and the study of such a penetrative convection or penetrative turbulence (Stull, 1976) is important for numerical weather prediction and the study of climate change. Generally speaking, the earth's atmosphere contains a stratified fluid, where the lowest region in contact with the surface, known as the atmospheric boundary layer (ABL), is mainly characterized by turbulence. The ABL turbulence is primarily induced by surface heating and wind shear, and is influenced by the diurnal cycle. In the daytime, turbulence is driven by convective destabilization (convective boundary layer), but in the night-time, wind shear is a primary mechanism to trigger turbulence (Blumen *et al.*, 2001). The free troposphere above the ABL is usually stably stratified (Gurvich & Kukharets, 2008). The effect of ABL turbulence may penetrate into the free troposphere through the entrainment of air from the overlying stably stratified region. This process transports momentum and

energy from the mixed region to the free troposphere, which affects boundary layer clouds (crucial for global climate change) (Lauer *et al.*, 2012) and may trigger clear air turbulence in the free troposphere (crucial for aviation safety) (Golding, 2002).

The interaction between turbulence and stratification is still poorly understood (Holford & Linden, 1999), although significant work has been done by several authors, for example, Waite & Bartello (2004), Lindborg (2006) etc. The researchers conjecture that knowledge of classical turbulence is insufficient to explain many aspects of the stratified turbulence (Fernando & Hunt, 1996). Atmospheric turbulence is often quasi-two-dimensional (Danilov & Gurarie, 2000) and supports an inverse energy cascade theory (Tung & Orlando, 2003). According to Lily's hypothesis (Lilly, 1983) of the pancake structure of stratified turbulence, the kinetic energy of, for example, a thunderstorm would cascade to a synoptic scale. However, the emergence of layering through a zigzag instability through the experimental results of Billant & Chomaz (2000) suggests the need for further investigation. For example, is turbulence in the atmosphere two-dimensional due to the presence of the inverse energy cascade, or three-dimensional due to the presence of vortex stretching? Indeed, it is not clear exactly how the onset of vertical motions in the atmosphere would destroy the quasi-two-dimensionality of turbulence and would stop the upscale energy transfer, although numerical modelling indicates a 3D regime when the vertical length scale exceeds approximately half of the forcing scale (Xia *et al.*, 2011).

In the atmosphere, stratification is caused by heating or cooling at the surface. If there are no major sources of wind shear, the classical theory of stratified turbulence suggests the suppression of mechanical turbulence by stable stratification. However, measurements of turbulence in the night-time atmospheric boundary layer appear to be episodes of turbulent "bursts" - a phenomenon that is called global intermittency (Mahrt, 1999; Ansorge & Mellado, 2014). The study of penetrative turbulence may help to explain global intermittency. Such an intermittency imposes challenges of numerical weather prediction (NWP); e.g. it

turns boundary layer mixing to be too difficult to be parameterized. A full understanding of intermittent turbulence from observation and flux measurements is also difficult because of the lack of accurate measurement technology. Hence, turbulence remains an unresolved problem, and the very complex features of stratified turbulence in the atmosphere have yet to be elucidated.

1.2 Aim and scope of the thesis

This thesis presents a novel computational model for investigating penetrative turbulence associated with differential heating in the ABL. I have published the numerical development in an article co-authored with J. Alam, R. Walsh, and A. Rose (see, Chapter 3). This thesis continues to extend the method presented in that article (*e.g.* Alam *et al.* (2014)), and aims to simulate a nonhydrostatic ABL phenomena in the presence of penetrative convection, stratified turbulence, and internal waves. It is worth mentioning that the numerical modeling of turbulence remains a challenging endeavor. For example, most nonhydrostatic numerical models, such as the WRF model (Skamarock *et al.*, 2005), use higher order upwind-biased explicit numerical schemes for which the artificial dissipation may be minimized with higher order discretization. Such upwind-biased higher order methods overshoot the dissipative scales, particularly when the effect of turbulence is filtered indirectly with such a method at the scale of boundary layer eddies (see the discussion in Wyngaard, 2004). In contrast, the present research studies a multiscale wavelet decomposition for filtering large eddies, where the advection terms are discretized without any artificial dissipation – thanks to the DD wavelets (Deslauriers & Dubuc, 1989) and the Krylov subspace.

As a short-term research, a validation of the proposed numerical model for simulating the penetrative turbulent convection in the ABL has been covered in this thesis. First, the

upward penetration of an isolated buoyant element into the surrounding atmosphere has been investigated because there exists a number of references simulating this case when the atmosphere is neutral and dry, and thus, it helps to understand the present numerical development. In addition, such a penetrative convection in the stable environment helps to understand the transfer of kinetic energy by internal waves (Lane, 2008). Second, more realistic than the first case, an idealized convective boundary layer has been simulated, where turbulent convective air mixes in a large horizontal area due to the differential surface heating; this convective mixed layer is capped with an inversion layer below the stably stratified atmosphere. Similar phenomena was investigated by Zhang *et al.* (2014) using the WRF-LES model. A long-term object of this test case aims to model how surface heating initiates temporal oscillations in mesoscale circulations through the mechanisms of downscale energy cascade as well as energy transfer by internal waves.

The rest of this chapter covers a literature review with introductory descriptions, and concludes with an outline for the rest of the thesis.

1.3 Review of related materials

1.3.1 Nonhydrostatic atmospheric model

Nonhydrostatic effects are important to simulate small-scale atmospheric flows such as eddies in the atmospheric boundary layer (ABL) having length scales of order a few kilometers or less, for example, to capture important numerical weather prediction (NWP) phenomena such as tornadoes, thunderstorms, hurricanes etc. Nonhydrostatic models were initially developed as a research tool for small-scale meteorological phenomena such as nonlinear mountain waves. Because of the development of computational fluid dynamics and the evolution of computer technology today, several nonhydrostatic models have been

developed and are applied to numerical simulations and operational NWP such as the UK Met Office (UKMO), Deutscher Wetterdienst (DWD) of Germany, the Japan Meteorological Agency (JMA), the National Center for Environmental Prediction (NCEP) of the USA, etc. The Weather Research and Forecasting (WRF) model, for example, is currently in operational use at NCEP and other centers.

There are several models used to evaluate computationally nonhydrostatic effects in the atmosphere. Defant (1951) utilized to analyze the magnitude of nonhydrostatic effects in a linear model for local thermally-induced circulations. To investigate the adequacy of the hydrostatic assumption for sea breeze circulations over a flat surface along with nonlinear analog, Martin & Pielke (1983) used the Defant model. Bryan & Fritsch (2002) presented a benchmark solution for testing the accuracy, efficiency, and efficacy of the moist nonhydrostatic numerical model.

Based on the conservation of mass, nonhydrostatic models can be classified in three ways: anelastic model, quasi compressible model and fully compressible model (see, Saito *et al.*, 2007). The anelastic model was invented by Ogura & Phillips (1962) in order to filter sound waves without assuming hydrostatic balance. The Boussinesq equations are a simplified version of the anelastic equations which are valid only for relatively shallow motion. Pseudo-incompressible approximation is an improvement on the anelastic continuity equation proposed by Durran (1989). In this approximation, the effect of the thermal expansion of air is incorporated by assuming that the perturbation pressure is negligible to the reference pressure. The quasi-compressible model predicts the pressure from divergence and considers the compressibility of air. A typical example of the quasi-compressible model is the Regional Atmospheric Modeling System (RAMS) proposed by Pielke *et al.* (1992). In the fully compressible model, the compressible conservation of mass is used, and Tapp & White (1976) designed the first non-hydrostatic compressible model for mesoscale studies.

In this thesis, a quasi-compressible model is incorporated for a dry atmosphere, which

is similar to Bryan & Fritsch (2002) for a dry atmosphere.

1.3.2 Turbulence in the atmospheric boundary layer

The atmosphere consists of several atmospheric layers. Near the earth's surface around $1\ \mathrm{km}$ of the atmospheric layer is the atmospheric boundary layer or planetary boundary layer (PBL). The pioneering work of boundary layer was done by Prandtl (1905) which is now known as the "boundary layer theory". The airflow within the boundary layer consists of mean wind, waves and turbulence. Turbulence is a type of fluid flow in which the fluid undergoes irregular fluctuations or mixing. Because of the shear in the mean wind and the temperature stratification, turbulence occurs in the atmospheric boundary layer. Turbulence can be depicted as consisting of irregular swirls of motions called eddies. The upper layer of the boundary layer in the atmosphere, which is usually non-turbulent, is often called free atmosphere. The troposphere and the structure of the planetary boundary layer are shown in figure 1.1. These pictures are incorporated from Stull (1988).

The PBL can be separated into four component layers; the surface layer, the mixed layer, the stable (Nocturnal) layer and the residual layer, which is shown in figure 1.1(right). The surface layer is closest to the earth where eddy fluxes are relatively constant. In this sub-layer, wind speed becomes zero in the earth's surface and the vertical profile of the wind is logarithmic. The mixed layer is created during the surface heating by the sun. Due to this surface heating, convective motion is created which leads to significant turbulent mixing in this sub-layer. Above the mixed layer is the stable layer which resists the upward movement of air parcel from the mixed layer. However, this mixed layer extinguishes when the solar heating dies out. After sunset, convective motion sharply decreases and a stable layer is formed near the surface layer, which is also called the nocturnal boundary layer and the remaining part of the mixed layer is called the residual layer. The approximate height

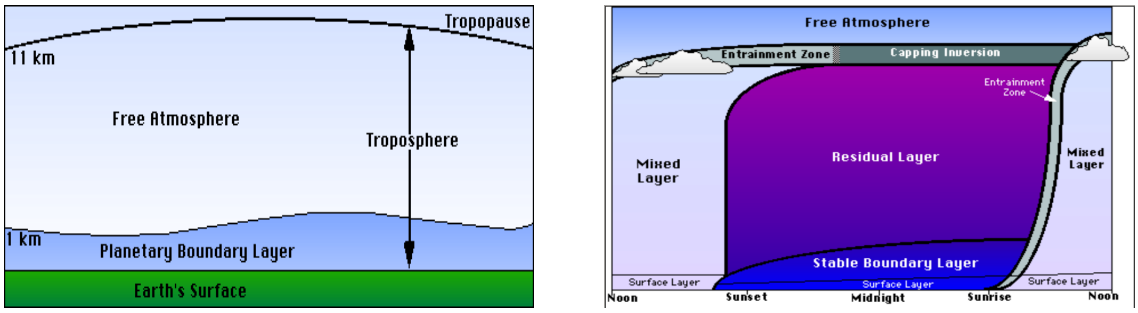

Figure 1.1: A boundary layer (blue) near the surface and the free atmosphere (picture on the left). Structure of the boundary layer in time (picture on the right) (adapted from Stull, 1988).

of the residual layer is the height of the mixed layer during the daytime.

The stability of the atmosphere can be defined as a basis of the vertical gradient of potential temperature (θ). If $\frac{\partial \theta}{\partial z}$ is positive, negative or zero then the atmosphere is stable, unstable or neutral respectively (see Kundu *et al.*, 2012, p. 20).

1.3.3 Representative models to study penetrative turbulence

Two atmospheric phenomena have been chosen to study the penetrative turbulence for two forms which are described in §1.2. Thermal rising in the atmosphere is considered as a relatively isolated buoyant element and the urban heat island circulation is considered as a turbulent convection in a large horizontal area.

1.3.3.1 Thermal rising in the atmosphere

The evolution of dry thermals in a stratified atmosphere has been investigated to study the development of a nonhydrostatic atmospheric model. As the earth is heated by the sun, thermals rise upward from the surface. A thermal cools as it rises, losing some of its buoyancy. A deep stable layer restricts the continued vertical growth of a thermal. This dry convection

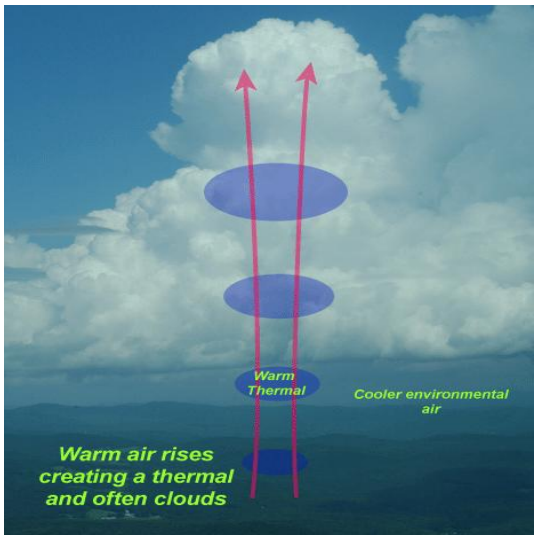

Figure 1.2: Thermal rising in the atmosphere (adapted from Atkins, 2006).

can also generate internal waves that can transport momentum and energy from the source to the region of large distances. A cartoon of a thermal rising is presented in Figure 1.2. Numerical simulation of a rising thermal in the atmosphere is investigated by the references of Carpenter *et al.* (1990), Tripoli (1992), Wicker & Skamarock (1998), Bryan & Fritsch (2002), Lane (2008), Alam (2011), etc. The early progress, focused primarily on flows in neutral environments, is made using analytic models (e.g., Morton *et al.*, 1956), laboratory experiments (e.g., Deardorff *et al.*, 1968) and numerical simulations (e.g., Ogura, 1962).

1.3.3.2 Urban Heat Island Circulation

The population of the planet Earth is increasing exponentially. Along with the increasing population, technology is also developing rapidly. Population pressure has direct and indirect effects on the environment. One such effect is urbanization. Urban areas consist of many high rise buildings, roads, houses, industries and other infrastructures and often lack of green areas. As a result, an urban area is significantly warmer than its surrounding rural areas due to human activities. The heat that is absorbed during the day is re-emitted after

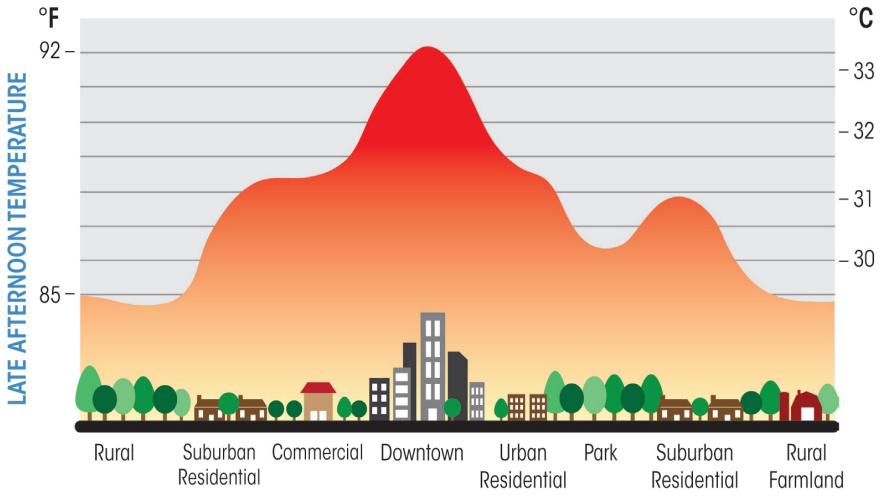

Figure 1.3: Urban Heat Island Profile (adapted from C3Headlines, 2012).

sunset which creates high-temperature differences between urban and rural areas. This urban area is called an urban heat island (UHI). Heat islands in cities usually have a mean temperature that is 8 to 10 degrees higher than the surrounding rural areas. A cartoon of the urban heat island profile is shown in Figure 1.3. This differential heating of the earth's surface gives rise to atmospheric circulations over a wide range of spatial and temporal scales. In this circulation, the lower atmospheric boundary layer faces turbulence mixing. Because of its importance in environmental problems, theoretical models (e.g. Nino & Mori, 2005; Ueda, 1983), laboratory experiments (e.g. Kimura, 1975; Lu *et al.*, 1997*a*,*b*), and numerical simulations (e.g. Baik *et al.*, 2001; Delage & Taylor, 1970; Dubois & Touzani, 2009; Richiardone & Brusasca, 1989*a*; Zhang *et al.*, 2014), were considered. Furthermore, numerous observational studies also have been conducted (e.g. Moeng, 1984).

A simple expression to predict the diurnal evolution of the urban-rural temperature difference is proposed by Richiardone & Brusasca (1989*b*). Using a nonlinear model (ARPS) and a two-layer linear analytical model, the effects of atmospheric boundary-layer stability on urban heat island-induced circulation are numerically and theoretically investigated by

Baik *et al.* (2007). In Dubois & Touzani (2009), a numerical study of heat island flows for stationary solutions at Rayleigh number, $Ra \leq 10^5$ is presented. In their simulation, despite the increase in computational resources, their proposed direct numerical simulation on finer grids remain unreachable. To remove this difficulty, Dubois & Touzani (2009) proposed to apply a thermal sponge layer in the vicinity of the vertical boundaries. Turbulent heat fluxes in urban areas are investigated by Grimmond & Oke (2002). Zhang *et al.* (2014) used the large-eddy simulation mode of the WRF model for simulating UHI circulation. They also applied the background wind along with UHI circulation.

1.4 Outline

The thesis is organised as follows. In Chapter 2 the governing equations and a subgrid scale methodology for parameterizing the effect of turbulence are presented. In Chapter 3 the numerical methodology is described, and a two-dimensional heat equation and a two-dimensional advection-diffusion equation are examined with this methodology. In Chapter 4 numerical simulations of the penetrative turbulence due to an isolated buoyant element are presented for the neutral and stable environment of the dry atmosphere. In Chapter 5 numerical simulations of another form of penetrative turbulence due to the differentially heated large horizontal area are presented. In this Chapter, UHI circulation is considered as a representative model of heterogeneous surface heating. Finally, conclusions are drawn and perspectives for future works on these simulations are discussed in Chapter 6.

Chapter 2

Mathematical model

This chapter presents the dynamical core, as well as a subgrid scale methodology for parameterizing the effect of turbulence. An important contribution of this thesis includes a novel approach of filtering mesoscale dynamics based on the Deslauriers-Dubac wavelet. It may be useful to study a large eddy simulation type methodology before presenting the wavelet method of Chapter 3.

2.1 Atmospheric scales

Let us begin with the wide range of atmospheric scales. Based on the atmospheric kinetic energy spectrum, three categories of atmospheric motions are suggested: (a) synoptic or large scale, (b) mesoscale, and (c) microscale (see, Lin, 2007). The mesoscale appears as the scale on which energy is transferred from large scale to microscale and vice versa. As demonstrated in Figure 2.1, mesoscale dynamics span a horizontal scale approximately from $2\ \mathrm{km}$ to $200\ \mathrm{km}$. From a dynamical perspective, mesoscale concerns processes with time scales ranging from the buoyancy oscillation ($2\pi/N$, where $N = \sqrt{\frac{g}{\theta_0}\beta}$ is the buoyancy frequency, β is the vertical gradient of synoptic-scale potential temperature and θ_0 is a

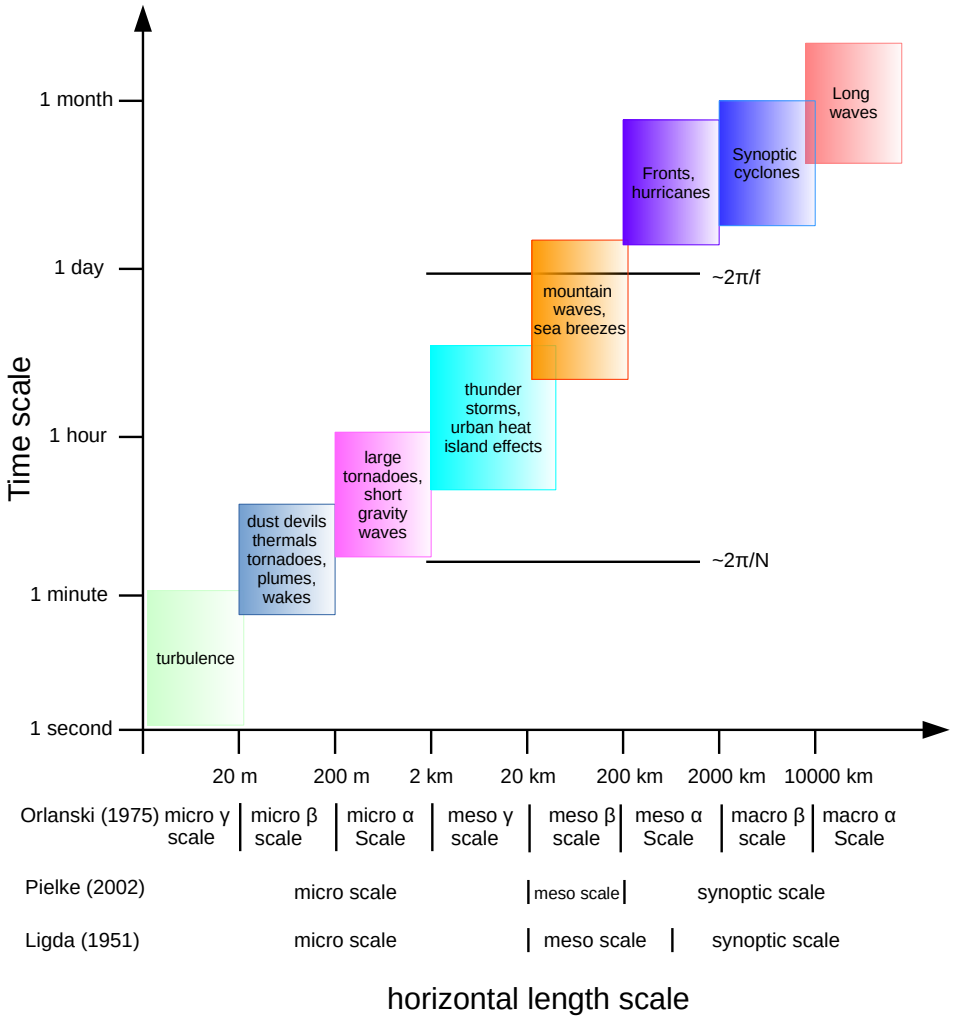

Figure 2.1: The spatial and temporal scales of various weather phenomena (adapted from Torn, 2014).

reference temperature) to a pendulum day ($2\pi/f$, where f is the Coriolis parameter). Typical atmospheric values of these frequencies are: $N \sim 10^{-2}$ s^{-1} (see Kundu *et al.*, 2012, p. 625) and $f \sim 10^{-4}$ s^{-1} (see Kundu *et al.*, 2012, p. 630). For example, sea breezes occur on a time scale of about 1 day and spatial scales of 10 to 100 km. Other examples of

mesoscale phenomena are mountain waves, inertia-gravity waves, heat island circulation, thunderstorms, density currents, squall lines, fronts etc. Further details of atmospheric scales are discussed by Ligda (1951), Pielke (2002) and Orlanski (1975).

2.2 Governing equations for mesoscale models

The following first principle conservation laws are filtered at mesoscale, where the motion is expressed with three components of wind velocity $\boldsymbol{u} = (u, v, w)$, temperature (T), pressure (p), and density (ρ). The set of a fully compressible fluid system can be written as, (Batchelor, 1967; Kundu *et al.*, 2012; Lin, 2007; Pielke, 2002)

conservation of mass

$$\frac{\partial \rho}{\partial t} + \nabla . \rho \boldsymbol{u} = 0, \tag{2.1}$$

conservation of momentum

$$\frac{\partial \boldsymbol{u}}{\partial t} + \boldsymbol{u} . \nabla \boldsymbol{u} = -\frac{1}{\rho} \nabla p - g\boldsymbol{k} - 2\boldsymbol{\Omega} \times \boldsymbol{u}, \tag{2.2}$$

conservation of energy

$$\frac{\partial \theta}{\partial t} + \boldsymbol{u} . \nabla \theta = S_\theta, \tag{2.3}$$

and the equation of state

$$p = \rho R T. \tag{2.4}$$

Here, $\boldsymbol{\Omega}$ is the angular velocity of the earth's rotation, S_θ is a source or a sink of θ, $\boldsymbol{k}$ is a unit vector in the vertical direction, and R is the gas constant for dry air. The potential temperature is defined by

$$\theta = T(p_0/p)^{R/C_p}, \tag{2.5}$$

where c_p is the specific heat at constant pressure, and p_0 is the reference pressure (usually 1000 hPa). Note that I have considered a dry atmosphere and the long term goal is to prepare a complete model including moisture.

2.3 Mesoscale perturbation of prognostic quantities

In order to represent the atmosphere accurately, equations (2.1) - (2.3) must be evaluated to spatial scales on the order of about 1 cm and to temporal scales of 1 second or so. Mesoscale circulations have horizontal extent on the order of 10 km to 100 km or more and the vertical extent up to the order of 10 km. So, equations (2.1) - (2.3) need to solve at $10^{18} - 10^{20}$ locations in order to capture a mesoscale phenomena accurately (see, chapter 4, Pielke, 2002). Unfortunately, there is no existing computing system which can support this huge computation. In this circumstance, we need to integrate the conservation equations for specified spatial and temporal scales based on the range of our available computing support as well as an acceptable time constraint.

The first step is to consider a space-time average (see, chap 4, Pielke, 2002), such that

$$\bar{u}_i = \frac{1}{\Delta t \Delta V} \int_t^{t+\Delta t} \int_V^{V+\Delta V} u_i \, \mathrm{d}V \, \mathrm{d}t \tag{2.6}$$

is the resolve part of

$$u_i = \bar{u}_i + u_i'',$$

where the unresolved part is a subgrid scale quantity u_i''. Applying the definition (2.6) on the product of velocity components, $u_i u_j$, we obtain

$$\overline{u_i u_j} = \overline{(\bar{u}_i + u_i'')(\bar{u}_j + u_j'')} = \overline{\bar{u}_i \bar{u}_j} + \overline{\bar{u}_i u_j''} + \overline{u_i'' \bar{u}_j} + \overline{u_i'' u_j''}. \tag{2.7}$$

If the operation (2.7) is chosen as

$$\overline{u_i u_j} = \bar{u}_i \bar{u}_j + \overline{u_i'' u_j''}$$

then this decomposition is often called Reynolds decomposition, and $\overline{u_i'' u_j''}$ is called Reynold stress (see, chap 4, Pielke (2002)). The space-time average (2.6) can be considered as an ensemble average in the grid volume ΔV at time interval Δt where the velocity vector in

a given turbulent flow is considered m realizations, say $u_i^{(n)}(\mathbf{x}, t)$, where $\mathbf{x} \in \Delta V$ and $t \in [0,\ \Delta t]$, then the ensemble average of $\{u_i^{(n)}(\mathbf{x}, t)\}$ would be, $\bar{u}_i = \frac{1}{m}\sum_{n=1}^{m} u_i^{(n)}(\mathbf{x}, t)$.

In mesoscale modelling (Pielke, 2002), when the mean quantity $\bar{u}_i$ contains a synoptic scale contribution, we can write

$$u_i = u_{i0} + u_i' + u_i''.$$

Here, synoptic scale component u_{i0} corresponds to a layer-wise structure at scales much larger than that of the mesoscale representative elementary volume and u_i' is the mesoscale perturbation from u_{i0}.

2.4 A treatment for the pressure field

In the dynamical system (2.1 - 2.4), the absence of a prognostic equation for pressure (p) introduces a major computational challenge. The method adopted in this section is similar to what is used in the regional atmospheric modelling system (RAMS) which is a comprehensive non-hydrostatic model (see, Pielke *et al.*, 1992). Define the exner function

$$\pi = \frac{T}{\theta},$$

which is the same as

$$\pi = \left(\frac{p}{p_0}\right)^{R/C_p}.$$

We get

$$\frac{1}{\rho}\frac{\partial p}{\partial x_i} = \theta\frac{\partial \pi}{\partial x_i}. \tag{2.8}$$

Applying the concept of Reynolds decomposition in (2.8) with $\pi = \bar{\pi} + \pi''$ and $\theta = \bar{\theta} + \theta''$, we obtain

$$\overline{\frac{1}{\rho}\frac{\partial p}{\partial x_i}} = \bar{\theta}\frac{\partial \bar{\pi}}{\partial x_i} + \overline{\theta''\frac{\partial \pi''}{\partial x_i}}, \tag{2.9}$$

where the second term on the right hand side of eq. (2.9) is usually neglected (see, pp. 53, Pielke, 2002). Then, for $\bar{\pi} = \pi_0 + \pi'$ and $\bar{\theta} = \theta_0 + \theta'$, the following two assumptions are common. First,

$$\theta_0 \left(1 + \frac{\theta'}{\theta_0}\right) \approx \theta_0,$$

and second, the synoptic-scale pressure field is hydrostatic, i.e. $\frac{\partial p_0}{\partial z} = -\rho_0 g$. Then

$$\theta_0 \frac{\partial \pi_0}{\partial z} = -g.$$

Thus

$$\overline{\frac{1}{\rho}\frac{\partial p}{\partial x_i}} + g\delta_{i3} = \theta_0 \frac{\partial \pi'}{\partial x_i} + \theta_0 \left(\frac{\partial \pi_0}{\partial x}\delta_{i1} + \frac{\partial \pi_0}{\partial y}\delta_{i2}\right) - \frac{\theta'}{\theta_0} g\delta_{i3}. \tag{2.10}$$

In other words, the mesoscale perturbation θ' is dominated with respect to a characteristic scale of gravity wave. In this approach, for a dry atmospheric condition we can show that,

$$\frac{\partial \pi'}{\partial t} + \frac{\partial}{\partial x_j}(u_j \pi') = 0 \tag{2.11}$$

which can be replaced for the equations (2.1) and (2.4). The use of eq. (2.11) eliminates the costly part of solving an elliptic equation.

2.5 Conservation of Momentum

In this section, the mean state in a turbulent flow are derived from the equation of motion (2.2). The contribution of turbulent fluctuations appears in equation (2.2) as a correlation of velocity-component fluctuations.

First, apply the decomposition $\rho = \bar{\rho} + \rho''$ and $u_i = \bar{u}_i + u_i''$ in the mesoscale momentum equation (2.2) which are defined in the definition (2.6). Second, using the definition of eq. (2.6) with the properties of Renolds average: $\overline{u_i + u_j} = \overline{u_i} + \overline{u_j}$, $\overline{u_i'} = 0$, $\overline{\overline{u_i}} = \overline{u_i}$, $\overline{\frac{\partial u_i}{\partial t}} = \frac{\partial \bar{u}_i}{\partial t}$, $\overline{\frac{\partial u_i}{\partial x}} = \frac{\partial \bar{u}_i}{\partial x}$ eq. (2.2) becomes

$$\frac{\partial \bar{u}_i}{\partial t} + \bar{u}_j \frac{\partial \bar{u}_i}{\partial x_j} = -\overline{\frac{1}{\rho}\frac{\partial p}{\partial x}} + \frac{1}{\bar{\rho}}\frac{\partial}{\partial x_j}\bar{\rho}\overline{u_i'' u_j''} - g\delta_{i3} - 2\epsilon_{ijk}\Omega_j \bar{u}_k. \tag{2.12}$$

Apply the equation (2.10) and $\bar{\rho} = \rho_0 + \rho'$ where $|\rho'|/\rho_0 \ll 1$ in (2.12) becomes

$$\frac{\partial \bar{u}_i}{\partial t} + \bar{u}_j \frac{\partial \bar{u}_i}{\partial x_j} = -\theta_0 \frac{\partial \pi'}{\partial x_i} - \theta_0 \left(\frac{\partial \pi_0}{\partial x} \delta_{i1} + \frac{\partial \pi_0}{\partial y} \delta_{i2} \right) - \frac{1}{\rho_0} \frac{\partial}{\partial x_j} \rho_0 \overline{u_i'' u_j''} + \frac{\theta'}{\theta_0} g \delta_{i3} - 2\epsilon_{ijk} \Omega_j \bar{u}_k. \tag{2.13}$$

The remaining subgrid-scale correlation term, $\overline{u_i'' u_j''}$, represents the contribution of turbulent fluctuations and is called the turbulent velocity flux which is denoted by τ_{ij}. Specifically, the terms $\overline{u''w''}$, $\overline{v''w''}$ are the vertical turbulent fluxes of horizontal momentum, and $\overline{u''v''}$ is the meridional turbulent flux of zonal momentum.

2.6 Conservation of Energy

The same way, we can apply the decomposition, $\theta = \bar{\theta} + \theta''$ in energy eq. (2.3)

$$\frac{\partial}{\partial t}(\bar{\theta} + \theta'') + \frac{\partial}{\partial x_j}(\bar{u}_j + u_j'')(\bar{\theta} + \theta'') = S_\theta. \tag{2.14}$$

Applying the averaging (2.6) to the eq. (2.14)

$$\frac{\partial \bar{\theta}}{\partial t} + \bar{u}_j \frac{\partial \bar{\theta}}{\partial x_j} = \bar{S}_\theta - \frac{1}{\rho_0} \frac{\partial}{\partial x_j} \rho_0 \overline{u_j'' \theta''}. \tag{2.15}$$

The terms $\overline{u_j'' \theta''}$ are the turbulent heat fluxes which can be denoted as $\tau_{\theta j}$. Again apply the decomposition, $\bar{\theta} = \theta_0 + \bar{\theta}(z) + \theta'$, eq. (2.15) becomes

$$\frac{\partial \theta'}{\partial t} + \bar{u}_j \frac{\partial \theta'}{\partial x_j} + u_i \frac{\partial \bar{\theta}}{\partial x_i} \delta_{i3} = \bar{S}_\theta - \frac{1}{\rho_0} \frac{\partial}{\partial x_j} \rho_0 \overline{u_j'' \theta''}, \tag{2.16}$$

where the term involving turbulent heat fluxes, $\overline{u_j'' \theta''}$, on the right hand side of (2.16) must be parameterized.

2.7 Subgrid-scale turbulence modelling

Turbulent stresses that appear in eq. (2.13) and (2.16) can be modelled in the following ways:

2.7.1 Basic concept for turbulence modelling

The turbulent stress, τ_{ij}, may be modeled following the phenomena of how the viscous stress would play a first principle role in the atmospheric boundary layer (Kundu *et al.*, 2012). As a result, the simplest resonable assumption is that the turbulent stress is proportional to the symmetric mean strain rate tensor (see Lilly, 1966),

$$\tau_{ij} = -K_M \left(\frac{\partial \bar{u}_i}{\partial x_j} + \frac{\partial \bar{u}_j}{\partial x_i} \right), \tag{2.17}$$

where K_M is called the eddy viscosity coefficient, variable in space and time.

2.7.2 Large eddy simulation (LES)

LES is a popular approach for simulating turbulent flows in which the eddy viscosity coefficient (K_M) can be approximated in a way that small eddies are modeled using a subgrid-scale (SGS) model, and large eddies are solved explicitly. The model of Smagorinsky (1963) is a popular eddy viscosity approach in which turbulent stresses are defined as (see, Alam & Islam, 2015):

$$\tau_{ij}^{LES} = -K_M S_{ij}, \tag{2.18}$$

where $\tau_{ij}^{LES} = \tau_{ij} - (1/3)\tau_{kk}\delta_{ij}$ and S_{ij} is the filtered strain rate tensor defined as

$$S_{ij}(x, y, z, t) = \frac{1}{2} \left(\frac{\partial \bar{u}_i}{\partial x_j} + \frac{\partial \bar{u}_j}{\partial x_i} \right).$$

The assumption proposed by Smagorinsky (1963) for K_M is:

$$K_M = 2(C_s \Delta)^2 \left(2 S_{ij} S_{ij}\right)^{\frac{1}{2}}, \tag{2.19}$$

where C_s is a dimensionless constant which is often called the Smagorinsky constant, and the filtered scale is defined by $\Delta = (\Delta x\ \Delta y\ \Delta z)^{1/3}$, where $\Delta x,\ \Delta y$ and Δz are the length of x, y and z direction, respectively, of the filtered cell. A typical value of C_s is 0.18 (e.g.

Deardorff, 1970; Senocak *et al.*, 2007). Using dimensional arguments Deardorff (1970) derived that

$$K_M = C_s^{4/3}\,\bar{\epsilon}^{1/3}\,\Delta^{4/3}, \tag{2.20}$$

where $\bar{\epsilon}$ is the rate of dissipation of turbulent energy within a local grid volume.

2.7.3 Mesoscale approach

The subgrid scale momentum flux terms can be parameterized as (See, Chap. 5 Pielke, 2002)

$$\frac{\partial \tau_{ij}}{\partial x_j} = \frac{\partial}{\partial x_j}\left(-K_M \frac{\partial \bar{u}_i}{\partial x_j}\right),$$

$$\frac{\partial \tau_{\theta j}}{\partial x_j} = \frac{\partial}{\partial x_j}\left(-K_H \frac{\partial \bar{\theta}}{\partial x_j}\right),$$

where K_M is called the exchange coefficient of momentum or simply eddy viscosity, and K_H is called the exchange coefficient or eddy diffusivity of heat. This approach of the parameterization of momentum and heat is called K-*theory*.

2.7.4 Is LES appropriate for mesoscale turbulence?

Let the scale of averaging in (2.6) be Δ, and that of the boundary layer eddies be L_E. A necessary assumption is that the scale Δ needs to be much smaller than the scale of the phenomenon to be simulated. For a mesoscale phenomena (*e.g.* $L_x \sim 200\mathrm{km}$, $\Delta \sim 10\ \mathrm{km}$), if the numerical grid satisfies this assumption then the numerical method works as an implicit filter for the mesoscale dynamics. In order to take (2.6) as an averaging process for LES, the action of (2.6) has to be like a low pass filter, so that a significant factor of the boundary layer eddies are resolved. This point would be more clear by considering the following discussion presented in Wyngaard (2004):

When $L_E << \Delta$, eq. (2.7) can be written as $\overline{u_i u_j} = \bar{u}_i \bar{u}_j + \overline{u_i'' u_j''}$ by applying the Reynolds assumptions $\overline{u_i''} = 0$ then $\overline{u_i'' \bar{u}_j} = \overline{u_i''}\ \bar{u}_j = 0$ and $\overline{\bar{u}_i \bar{u}_j} = \bar{u}_i \bar{u}_j$. In this case, mesoscale modeling is appropriate and the turbulent stresses are defined as

$$\tau_{ij}^{meso} = \overline{u_i'' u_j''}. \tag{2.21}$$

Thus boundary layer eddies are entirely parameterized.

When $L_E >> \Delta$, Large Eddy Simulation (LES) is appropriate where

$$\tau_{ij}^{LES} = \overline{u_i u_j} - \bar{u}_i \bar{u}_j, \tag{2.22}$$

such that $\tau_{ij}^{LES} = \tau_{ij}^{meso} + L_{ij} + C_{ij}$, the Leondard tensor $L_{ij} = \overline{\bar{u}_i \bar{u}_j} - \bar{u}_i \bar{u}_j$ and the Clark tensor $C_{ij} = \overline{u_i'' \bar{u}_j} + \overline{\bar{u}_i u_j''}$. Hence, the LES approach may not be applicable for turbulence modelling at mesoscale although most cloud resolving mesoscale models adopt the LES method.

In order to capture micro scale phenomena in mesoscale (*e.g.* turbulence), an appropriate filtering technique is essential. In this thesis, mesoscale equations are filtered using the Deslauriers-Dubac wavelet (see, Chapter 3), and the eddy viscosity is estimated based on equation (2.20).

2.8 Governing equations

The governing equations for a stratified flow in a dry atmosphere at mesoscale are given by the equations (2.11), (2.13) and (2.16). These equations can be written in the following form, where the prime ($'$) and over bar ($^-$) from dependent variables have been dropped for simplicity,

$$\frac{\partial \pi}{\partial t} + u_j \frac{\partial \pi}{\partial x_j} = -\pi \frac{\partial u_i}{\partial x_i}, \tag{2.23}$$

$$\frac{\partial u_i}{\partial t} + u_j \frac{\partial u_i}{\partial x_j} = -\theta_0 \frac{\partial \pi}{\partial x_i} - \theta_0 \left(\frac{\partial \pi_0}{\partial x} \delta_{i1} + \frac{\partial \pi_0}{\partial y} \delta_{i2} \right) + \frac{\partial \tau_{ij}}{\partial x_j} + \frac{\theta}{\theta_0} g \delta_{i3} - 2\epsilon_{ijk} \Omega_j u_k, \quad (2.24)$$

$$\frac{\partial \theta}{\partial t} + u_j \frac{\partial \theta}{\partial x_j} + w\beta = \frac{\partial \tau_{\theta j}}{\partial x_j}, \quad (2.25)$$

where $\beta = \partial \bar{\theta} / \partial z$. From section 2.7 and the eddy motion in the atmosphere proposed by Taylor (1915) subgrid scale stress term in eq. (2.24) can be parametrized as

$$\frac{\partial \tau_{ij}}{\partial x_j} = K_{M_h} \left(\frac{\partial^2 u_i}{\partial x^2} + \frac{\partial^2 u_i}{\partial y^2} \right) + K_{M_v} \frac{\partial^2 u_i}{\partial z^2}, \quad (2.26)$$

$$\text{and} \quad \frac{\partial \tau_{\theta j}}{\partial x_j} = K_H \frac{\partial^2 \theta}{\partial x_j^2}, \quad (2.27)$$

where K_{M_h} and K_{M_v} are horizontal and vertical eddy viscosity, respectively, for momentum, and K_{M_v} is much smaller than K_{M_h}. These eddy viscosities are much larger than molecular viscosities; typically suggested values are $K_{M_v} \sim 10$ m^2 s^{-1} and $K_{M_h} \sim 10^5$ m^2 s^{-1} for the lower atmosphere (see, Kundu *et al.*, 2012).

2.9 Linearization of model equations and mesoscale waves

In the atmosphere, when an air parcel is displaced from its original position then it may return to its original position because of a restoring force. This movement of air parcels may generate atmospheric waves. We can observe mainly the following three types of waves: (a) sound or acoustic waves, (b) mesoscale waves and (c) planetary waves (see, Lin, 2007). For these three types of waves, the restoring forces are compression force, buoyancy force and Coriolis force, respectively. Mesoscale waves can be generated any one of the following sources: orography, surface heating or cooling, moist convection, density current etc. In mesoscale, when the environment is stable everywhere then gravity

waves can be generated due to a heat source, and it propagates upward and downwards which is also called vertically propagating waves. In a stably stratified environment when the buoyancy frequency is N, the oscillation period of the air parcel is $T = \frac{2\pi}{N}$.

Considering two-dimensional ($\frac{\partial}{\partial y} = 0$), nonrotating, adiabatic, boussinesq flow with uniform stratification then the temperature equation (2.25) can be linearized as

$$\frac{\partial \theta}{\partial t} + u_0 \frac{\partial \theta}{\partial x} + \frac{N^2 \theta_0}{g} w = 0 \tag{2.28}$$

and equations (2.23)-(2.25) can be linearized and combined as a single equation which is a simplified form of the Taylor-Goldstein equation is as follows:

$$\left(\frac{\partial}{\partial t} + u_0 \frac{\partial}{\partial x}\right)^2 \left(\frac{\partial^2 w}{\partial x^2} + \frac{\partial^2 w}{\partial x^2}\right) + N^2 \frac{\partial^2 w}{\partial x^2} = 0. \tag{2.29}$$

Assuming

$$\theta(x, z, t) = \tilde{\theta}(z) e^{i(kx - \omega t)},$$

$$w(x, z, t) = \tilde{w}(z) e^{i(kx - \omega t)},$$

where ω is wave frequency, $k = \frac{2\pi}{L_x}$ is the horizontal wave number and L_x is the horizontal length scale. Substitute these into (2.28) and (2.29), respectively, then (2.28) becomes

$$-i\omega\tilde{\theta} + iu_0 k\tilde{\theta} + \frac{N^2 \theta_0}{g}\tilde{w} = 0,$$

which implies

$$\text{buoyancy}, b \left(= \frac{g\tilde{\theta}}{\theta_0}\right) = i\frac{N^2}{\Omega}\tilde{w},$$

and (2.29) becomes

$$\frac{\partial^2 \tilde{w}}{\partial z^2} + \left(\frac{N^2}{\Omega^2} - 1\right) k^2 \tilde{w} = 0, \tag{2.30}$$

where $\Omega = \omega - ku_0$, is the intrinsic (Doppler-shifted) frequency of the wave. Equation (2.30) has the following two solutions:

$$\tilde{w} = c_1 e^{ik\sqrt{N^2/\Omega^2 - 1}\, z} + c_2 e^{-ik\sqrt{N^2/\Omega^2 - 1}\, z}, \qquad \text{for } N^2/\Omega^2 > 1, \tag{2.31}$$

$$\tilde{w} = c_3 e^{k\sqrt{1-N^2/\Omega^2}\ z} + c_4 e^{-k\sqrt{1-N^2/\Omega^2}\ z}, \qquad \text{for } N^2/\Omega^2 < 1. \tag{2.32}$$

Equation (2.31) is sinusoidal so it represents vertically propagating waves and eq. (2.32) represents evanescent waves.

If the stratification of the fluid is uniform and the disturbance is sinusoidal in the vertical i.e. $\tilde{w}(z) = w_0 e^{imz}$ where $m = \frac{2\pi}{L_z}$ is vertical wave number and L_z is the vertical length scale then from eq. (2.30) we can obtain the dispersion relation for internal gravity waves which can be written as

$$\omega = N \cos\alpha, \tag{2.33}$$

where $\alpha = \tan^{-1}(m/k)$ is the angle between the phase velocity vector and the horizontal direction. Moreover, the wave frequency lies in $f < \omega < N$, and this relation indicates that the maximum possible frequency of internal waves in a stratified fluid is N.

2.10 Summary

In this chapter, a filtered mathematical model has been explained briefly for investigating nonhydrostatic mesoscale phenomena due to penetrative turbulence in a dry atmosphere. Moreover, subgrid scale parameterization of turbulence stress terms, based on Smagorinsky type large eddy simulation methodology, has been presented in this chapter and linearized model equations have been described to analyse the mesoscale waves in the free atmospheric.

In the next chapter, numerical methodology is described, and a two-dimensional heat equation and a two-dimensional advection-diffusion equation are examined with this methodology.

Chapter 3

Numerical methodology

A weighted residual collocation method based on a diadic mesh refinement technique has been developed through this research. A detailed description of this method is presented in a joint article (Alam *et al.*, 2014), which is published in the international journal of numerical methods in fluids. This chapter summarizes the method, presents some primary results which are not discussed in the published article, and explains the benefits of this method for simulating non-hydrostatic mesoscale circulations. Moreover, this thesis continues to extend the method presented in that article (Alam *et al.*, 2014) for simulating a nonhydrostatic ABL phenomena in the presence of penetrative convection, stratified turbulence, and internal waves. The simulated results of this extended method are presented in Chapter 4 and 5. This numerical methodology is based on a wavelet basis, a set $\{\varphi_k(\boldsymbol{x})\}$ of interpolating scaling functions, the principle of multiresolution approximation (see, pp 267, Mallat, 2009), and the subdivision scheme that was developed by Deslauriers & Dubuc (1989) (*hereinafter*, DD subdivision). Each two dimensional scaling function, $\varphi_k(\boldsymbol{x})$, is an extension of the one dimensional uniformly continuous fundamental function $\varphi_k(x)$ (Deslauriers & Dubuc, 1989). The extension is achieved by applying the DD subdivision on a two-dimensional mesh (see Deslauriers *et al.*, 1991). In Alam *et al.* (2014), a method

for approximating the partial derivatives was developed. The model equations, which are presented in §2.8, are discretized by considering a trial solution that is a linear combination of the set of basis functions $\{\varphi_k(\boldsymbol{x})\}$ (see Finlayson, 1972). Theoretical details of the method of weighted residual with respect to a trial solution is given by Finlayson (1972). In this thesis, a fully implicit second order time integration scheme is studied, where the simultaneous dependence of mass, momentum, and energy conservation laws in the spatial domain is approximated through an iterative process. As a result, a large system of coupled nonlinear equations is solved by the Newton-Krylov method (Alam, 2011; Kelly *et al.*, 2009). Alam (2011) and Alam & Islam (2015) verified the efficiency of the Newton-Krylov method for simulating the dynamics of a dry atmosphere. In this chapter, heat equation and Burger's equations are solved on a two-dimensional mesh because exact solutions of these equations can be obtained.

3.1 Wavelets

The distinguishing feature about wavelets is that they are localized in space and scale with a zero average, which allows local variations of the problem to be analyzed at various levels of resolution. Wavelet basis are composed of two kinds of functions: scaling functions (φ) and wavelet functions (ψ). The spaces generated by scaling and wavelet functions are complementary and both are based on the same mother function. In the following expressions, known as the two-scale relation,

$$\varphi(x) = \sum_{k=0}^{p-1} c_k \varphi(2x - k), \tag{3.1a}$$

$$\psi(x) = \sum_{k=0}^{p-1} (-1)^k c_{p-1-k} \varphi(2x - k), \tag{3.1b}$$

where c_k are the scaling function filter coefficients, and p is the Daubechies wavelet order (Mallat, 1989). In general, there are no analytical expressions for scaling functions and

wavelet functions, which can be obtained using iterative or recursive procedures like eq. (3.1). The translation and dilation of $\varphi(x)$ can construct a basis $\{\varphi_k(x)\}$ which may use as trial functions to approximate the solution of partial differential equation (PDE). Mallat (1989) showed that a function $u(x)$ can be approximated on such a basis $\{\varphi_k(x)\}$.

3.2 The collocation method

Collocation methods are special cases of weighted residual methods (Finlayson, 1972) which have an important application for simulating Navier-Stokes equations (*e.g.* Subich *et al.*, 2013; Ranjan & Pantano, 2013). To briefly present the method of weighted residual, using the DD subdivision scheme, consider the PDE for $u(\boldsymbol{x}, t)$

$$\frac{\partial u}{\partial t} - \nabla^2 u = f \quad \text{such that} \quad \boldsymbol{x} \in \Omega \subseteq \mathbb{R}^2, t > 0,$$

which is subject to

$$u(\boldsymbol{x}, 0) = \mathcal{U}_0(\boldsymbol{x}) \quad \text{for} \quad \boldsymbol{x} \in \Omega \quad \text{and}$$

$$u(\boldsymbol{x}, t) = \mathcal{U}_1(\boldsymbol{x}, t) \quad \boldsymbol{x} \in \partial\Omega, \quad t \geq 0.$$

Assume a trial solution of the form

$$u^s(\boldsymbol{x}, t) = \sum_{k=0}^{\mathcal{N}-1} c_k(t)\varphi_k(\boldsymbol{x}), \tag{3.2}$$

where s is the level of resolution. As the number $\mathcal{N}$ increases in successive approximations (e.g., Finlayson, 1972), the residual,

$$\mathcal{R}(\boldsymbol{x}, t) = u(\boldsymbol{x}, t) - \sum_{k=0}^{\mathcal{N}-1} c_k(t)\varphi_k(\boldsymbol{x}),$$

for a fixed t becomes smaller, and finally, vanishes for $\mathcal{N} \to \infty$; i.e. the exact solution is recovered at $\mathcal{N} \to \infty$. This estimate is equivalent to the multiresolution approximation of

Mallat (1989) where $\{\varphi_k(x)\}$ developed through a multiresolution subdivision. Now, for a choice of the dual basis $\tilde{\varphi}_k(\boldsymbol{x})$, the weighted integral of the residual,

$$\langle \mathcal{R}(\boldsymbol{x},t), \tilde{\varphi}_k(\boldsymbol{x})\rangle = \int_\Omega \mathcal{R}(\boldsymbol{x},t)\tilde{\varphi}_k(\boldsymbol{x})dx,$$

and that for the PDE,

$$\left\langle \frac{\partial u^s}{\partial t} - \nabla^2 u^s - f,\ \tilde{\varphi}_k(\boldsymbol{x}) \right\rangle, \tag{3.3}$$

are both set equal to zero. The trial solution $u^s(\boldsymbol{x},t)$ can be chosen from the following nested approximation spaces

$$\nu^0 \subseteq \ldots \subseteq \nu^{s-1} \subseteq \nu^s \subseteq \nu^{s+1} \ldots. \quad \text{and} \quad \cup_{s=0}^{\infty} \nu^s = L_2(\bar{\Omega})$$

where each ν^s has a basis $\{\varphi_k(\boldsymbol{x})\}$ and contains functions which may not oscillate frequency larger than 2^{s-1}. The collection of approximation spaces $\{\nu^s\}$ is called a multiresolution approximation space (Sweldens, 1998). A dual multiresolution approximation is a collection of spaces $\{\tilde{\nu}^s\}$ with a basis $\{\tilde{\varphi}_k(\boldsymbol{x})\}$, where $\langle \varphi_k(\boldsymbol{x}), \tilde{\varphi}_j(\boldsymbol{x})\rangle = \delta_{k,j}$. The trial function $u^s(\boldsymbol{x},t)$ defined by (3.2) is called the multiresolution projection of $u(\boldsymbol{x},t)$ onto the space ν^s, where $\mathcal{N}$ is the dimension of ν^s and $c_k(t) = \langle u(\boldsymbol{x},t), \tilde{\varphi}(\boldsymbol{x})\rangle$.

Note that the superscript s can be dropped for simplicity, and one may use u^n to represent the numerical solution at n-th time step. The dual basis $\{\tilde{\varphi}_k(\boldsymbol{x})\}$ can be chosen in several ways. Once the choice is made, and a time discretization is chosen, eq. (3.3) becomes a set of $\mathcal{N}$ coupled algebraic equations, which can be expressed conveniently

$$\mathcal{L}(u^{n+1}) = f(u^n). \tag{3.4}$$

In this present work, we have taken $\tilde{\varphi}_k(\boldsymbol{x}) = \delta(\boldsymbol{x} - \boldsymbol{x_k})$, for which the residual (3.3) vanishes on a finite number ($\mathcal{N}$) of collocation points. Following is a brief description of the DD subdivision method, which develops $\{\varphi_k(\boldsymbol{x})\}$.

Dyadic mesh: A one-dimensional mesh is a set of nodes on a real line, which can be defined as a dyadic subdivision,

$$\mathcal{G}^s = \{x_k^s \in \mathbb{R} : x_k^s = k2^{-s}, k \in \mathbb{Z}\}, \quad s \in \mathbb{Z}_{\geq 0}$$

which is shown in Figure 3.1a, where x_k^s are the nodes and s is the level of resolution. In this case, $x_k^{s-1} = x_{2k}^s$ and

$$\mathcal{G}^0 \subseteq ... \subseteq \mathcal{G}^{s-1} \subseteq \mathcal{G}^s \subseteq \mathcal{G}^{s+1} ... \quad \text{and} \quad \lim_{s\to\infty} \mathcal{G}^s = \overline{\Omega}.$$

Such a mesh, $\mathcal{G}^s$, is associated with the function space ν^s. Similarly, a nested sequence of dyadic mesh can be constructed in two-dimensional space where the set of nodes can be written as,

$$\mathcal{G}^s = \{(x_k^s, y_l^s) \in \mathbb{R}^2 : x_k^s = k2^{-s} \text{ and } y_l^s = l2^{-s} \text{ and } k, l \in \mathbb{Z}\}, \quad s \in \mathbb{Z}_{\geq 0}$$

which is shown in Figure 3.1b. The number of nodes in $\mathcal{G}^s$ is $\mathcal{N}$. Let $\mathcal{G}^0$ be a two dimensional mesh with $n_x \times n_y$ nodes. In this mesh, the number of nodes $\mathcal{N} = [(n_x - 1)2^s + 1] \times [(n_y - 1)2^s + 1]$.

A brief outline of the construction of the basis $\varphi_k(x)$ is given in the following section, more details of which is also given in Alam *et al.* (2014).

3.3 Interpolating scaling function

Let c_k^0 (= $c_k(0)$) be the original sample values. Now we can create a sequence of sample values recursively using interpolating polynomials. We use $2p$ samples and build a polynomial of degree $2p - 1$. For linear interpolation, define a refined sequence of sample values recursively as

$$c_{2k}^{s+1} = c_k^s, \qquad c_{2k+1}^{s+1} = (c_k^s + c_{k+1}^s)/2$$

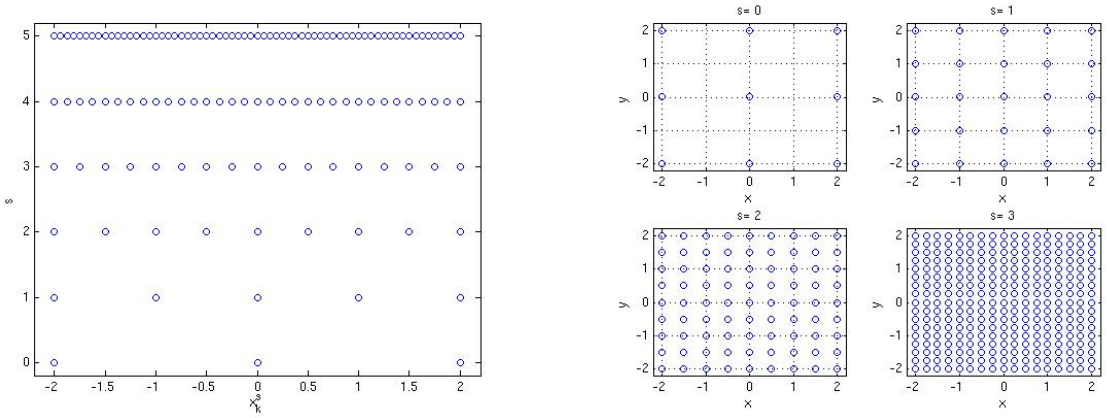

(a) One dimensional diadic mesh

(b) Two dimensional diadic mesh

Figure 3.1: Diadic mesh in one and two dimensional domain.

and place the c_k^s at locations $x_k^s = k2^{-s}$. Similarly, we can define the cubic polynomial $p(x)$ which interpolates four neighbouring values in which two from left and two from right

$$c_{k-1}^s = p(x_{k-1}^s), \qquad c_k^s = p(x_k^s),$$

$$c_{k+1}^s = p(x_{k+1}^s), \qquad c_{k+2}^s = p(x_{k+2}^s).$$

Then the new samples for next refine level are:

$$c_{2k}^{s+1} = c_k^s \quad \text{and} \quad c_{2k+1}^{s+1} = p(x_{2k+1}^{s+1}).$$

In Figure 3.2, on the left a diagram shows the filling in of "in between" samples by linear interpolation between neighboring samples. On the right, the same idea is applied to higher order interpolation using two neighbors to either side and the unique cubic polynomial which interpolates these. This process is repeated an infinitum to define the limit function. This was described by Sweldens & Schröder (1996) in details.

For one dimensional mesh points which is shown in Figure (3.1a), set $c_k^0 = 0, k \neq 0$ and $c_0^0 = 1$. Now, run the interpolating subdivision to infinity. Then the resulting function is $\varphi(x)$ is called the scaling function. The iterative process from $s = 0$ to $s = 5$ are shown

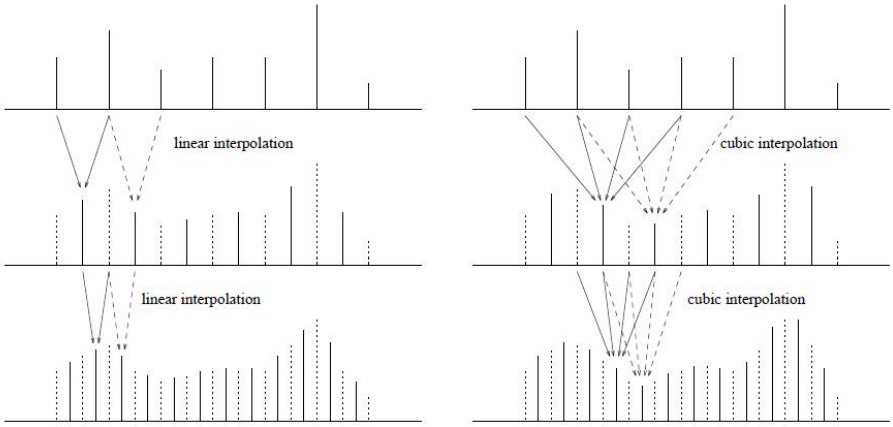

Figure 3.2: Examples of interpolating subdivision (adapted from Sweldens & Schröder, 1996).

in Figure 3.3a to 3.3f. Similarly, we can construct the scaling functions for two or higher dimensions.

If the scaling function $\varphi(\boldsymbol{x})$ is built on a two-dimensional mesh, then its one-dimensional restriction is exactly the fundamental function $\varphi(x)$ of Deslauriers & Dubuc (1989), which has the following properties (see Alam *et al.*, 2014).

- $\varphi(x)$ is an interpolating polynomial, which vanishes outside of $[x_{-2p+1}, x_{2p-1}]$, where p is an integer. Moreover, $\varphi(x_0) = 1$ and $\varphi(x)$ has exactly $4p-2$ zeros in the interval $[x_{-2p+1}, x_{2p-1}]$.

- $\varphi(x)$ is symmetric about $x = x_0$; i.e. $\varphi(x)$ is an even function.

- $\varphi(x)$ is uniformly continuous for all p on any finite interval, and is differentiable for $p > 1$. Moreover, $\varphi(x)$ has at least two continuous derivatives for $p = 3$.

- $\varphi(x)$ is translated to construct a basis $\{\varphi_k(x)\}$ that satisfies $\varphi_k(x_j) = \delta_{kj}$ and reproduces polynomials up to degree $2p - 1$.

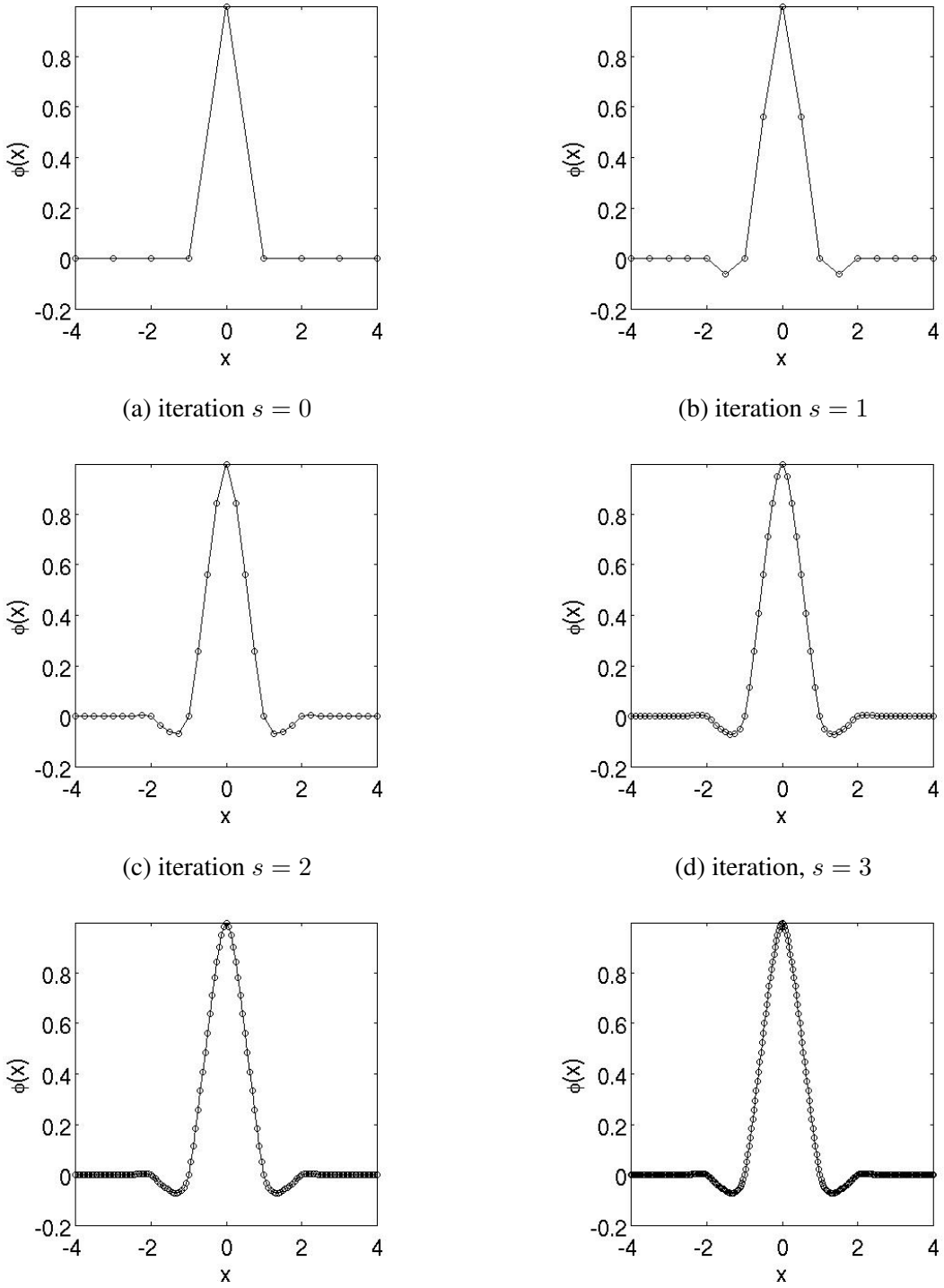

(a) iteration $s = 0$

(b) iteration $s = 1$

(c) iteration $s = 2$

(d) iteration, $s = 3$

(e) iteration, $s = 4$

(f) iteration, $s = 5$

Figure 3.3: A one-dimensional scaling function, $\varphi(x)$, generated with a cubic interpolation process. We see that the interpolation tends to a unique function.

- For the even function

$$f(x) = \begin{cases} 1 & \text{for} \quad x = x_k \\ 0 & \text{for} \quad x > x_{k+2p-1} \text{ and } x < x_{k-2p+1} \end{cases}$$

having $4p-2$ zeros within its support $[x_{k-2p+1}, x_{k+2p-1}]$, we have

$$f(x) = \sum_{k=-4p+2}^{4p-2} c_k \varphi_k(x).$$

This property is also known as the two scale relation because $f(x)$ is defined on $\mathcal{G}^s$ and $\varphi_k(x)$ is defined on $\mathcal{G}^{s+1}$.

3.4 Differentiation

In this section, we study the weighted residual collocation method for the numerical differentiation of the trial solution (3.2) on the basis of the scaling function. In a collocation method, one aims to compute $\frac{\partial}{\partial x} u^s(\boldsymbol{x}, t)$ (e.g. for fixed y) at all nodes x_k such that

$$\langle \frac{\partial}{\partial x} u^s(\boldsymbol{x}, t), \delta(\boldsymbol{x} - \boldsymbol{x_k}) \rangle = 0$$

on a mesh $\mathcal{G}^s$. This is done by using some properties of $\varphi_k(\boldsymbol{x})$, and the trial solution (3.2); i.e. (for simplicity the superscript s is dropped)

$$\frac{\partial}{\partial x} u(\boldsymbol{x}, t) = \sum_{k=0}^{\mathcal{N}-1} c_k(t) \varphi_k'(\boldsymbol{x}). \tag{3.5}$$

Since $\varphi_k(x)$ (for fixed y) is an even function with respect to $x = x_k$, and $\varphi_k(x)$ has exactly $4p-2$ zeros within its support $[x_{k-2p+1}, x_{k+2p-1}]$, the following statements are true. (i) The 1st derivative $\varphi_k'(x)$ is an odd function, (ii) it vanishes at x_k, i.e. $\varphi_k'(x_k) = 0$, (iii) $\varphi_k'(x)$ takes nonzero values on at most $4p-2$ zeros of $\varphi_k(x)$ in (x_{k-2p+1}, x_{k+2p-1}), and $\varphi_k'(x)$ vanishes for all other $x \notin (x_{k-2p+1}, x_{k+2p-1})$ (see, Deslauriers & Dubuc, 1989).

Using these properties, combining $\langle \frac{\partial}{\partial x} u(\boldsymbol{x}, t),\ \tilde{\varphi}(\boldsymbol{x}) \rangle$ with eq (3.5) results into

$$\frac{\partial}{\partial x} u(x_k, t) = \sum_{j=k-2p+1}^{j=k+2p-1} c_j(t) \varphi_k'(x_j) \tag{3.6}$$

To evaluate the right side of (3.6), let us obtain the nodal value of $\varphi_k(x)$ for $x \in [x_{k-2p+1}\ , x_{k+2p-1}]$ from the interpolating process, without knowing the actual mathematical form of $\varphi_k(x)$, using the barycentric formula

$$\varphi_k(x) = \frac{w_k(x)}{\sum_{i=k-2p+1}^{k+2p-1} w_i(x)}$$

at x_j for $j = k-2p+1, ..., k+2p-1$ (see Berrut & Trefethen, 2004). The weights $w_k(x)$ are associated with $2p+1$ nodes, and are extended from the iterative interpolation process that derives $\varphi(x)$. In order to employ weighted residual collocation method, the weights $w_k(x)$ and $\zeta(x)$ are defined as,

$$\frac{1}{w_k(x)} = (x - x_k) \prod_{j \neq k} (x_k - x_j)$$

and

$$\zeta(x) = \sum_l w_l(x)(x - x_j)$$

and assume the weighted inner product

$$\langle [\varphi_k(x)\zeta(x)]',\ \tilde{\varphi}_k(x) \rangle = 0.$$

Then the first derivative of scaling function can be computed as (see Alam *et al.*, 2014)

$$\varphi_k'(x_j) = \begin{cases} \frac{w_k(x)}{w_j(x)(x_k - x_j)} & \text{for} \quad k \neq j \\ -\sum_{k \neq j} \varphi_k'(x_j) & \text{for} \quad k = j. \end{cases}$$

It is clear that, knowing the ingredients, w_k's, of the iterative interpolation, we are able to compute derivatives of $\varphi_k(x)$ exactly on all nodes. Similarly, for the second derivative,

$$\frac{\partial^2}{\partial x^2} u(\boldsymbol{x}, t) = \sum_{k=0}^{\mathcal{N}-1} c_k(t) \varphi_k''(\boldsymbol{x}), \tag{3.7}$$

at x_j for $j = k - 2p + 1, ..., k + 2p - 1$, we get

$$\frac{\partial^2}{\partial x^2} u(x_j, t) = \sum_{j=k-2p+1}^{j=k+2p-1} c_k(t) \varphi_k''(x_j). \tag{3.8}$$

The second derivative of scaling function can be computed by using the following expression (see Alam *et al.*, 2014)

$$\varphi_k''(x_j) = \begin{cases} -2\varphi_k'(x_j) \left[\sum_{i \neq k} \varphi_k'(x_i) - \frac{1}{x_j - x_k} \right] & \text{for} \quad k \neq j \\ -\sum_{k \neq j} \varphi_k''(x_j) & \text{for} \quad k = j. \end{cases}$$

3.5 Numerical examples

In this section, we examine the proposed spatial discretization methodology with two examples, a two dimensional heat equation and a two dimensional advection-diffusion equation, where a Krylov method has been used to solve the discrete system. More specifically, we have employed the restarted generalized minimal residual (GMRES) algorithm. We examine numerical accuracy of these examples where the solution can be derived analytically.

3.5.1 Two dimensional heat equation

Consider a thin rectangular plate made of some thermally conductive material. Let $u(x, y, t)$ be the temperature of the plate at position (x, y) and time t. For a fixed t, the height of the surface $z = u(x, y, t)$ gives the temperature of the plate at time t and position (x, y). Under ideal assumptions (e.g. uniform density, uniform specific heat, perfect insulation, no internal heat source etc.) u satisfies the following two dimensional heat equation

$$u_t = (\kappa u_x)_x + (\kappa u_y)_y + \psi \tag{3.9}$$

for $0 < x < a$ and $0 < y < b$, where $\kappa(x, y) > 0$ is a diffusion or heat conduction coefficient that may vary with x and y, and $\psi(x, y, t)$ is an external heat source. The

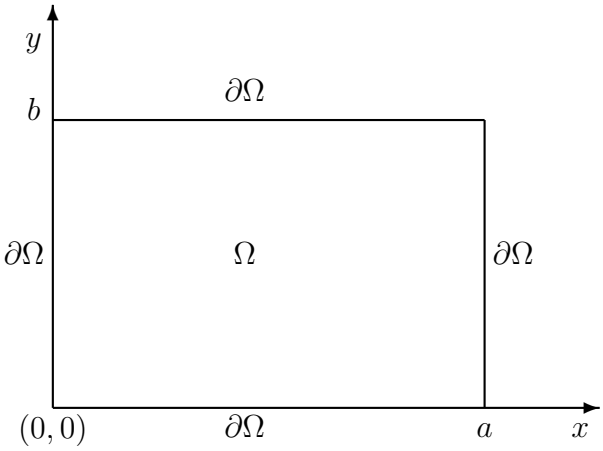

Figure 3.4: Rectangular plate $[0, a] \times [0, b]$.

solution $u(x, y, t)$ generally will vary with time as well as space. We also need initial condition $u(x, y, 0)$ in Ω and boundary conditions on the boundaries $\partial\Omega$. Domain of this model is shown in Figure (3.4). For constant $\kappa > 0$, eq. (3.9) can be written as,

$$u_t = \kappa(u_{xx} + u_{yy}) + \psi \tag{3.10}$$

Consider a case without external heat source i.e. $\psi(x, y) = 0$. Then the discretized equation, $\mathcal{L}(u^{n+1}) = f(u^n)$, such that

$$-\kappa\nabla^2 u^{n+1} + \frac{2}{\Delta t}u^{n+1} = \kappa\nabla^2 u^n + \frac{2}{\Delta t}u^n \tag{3.11}$$

has been obtained by discretizing (3.10) in time with a Trapezoidal method. The discretized system (3.11) is solved by using cubic interpolation and the level of resolution, $s = 5$. So the number of grid points are $(2^{s+1} + 1) \times (2^{s+1} + 1)$ i.e., 65×65. In this example, choose the initial condition,

$$u(x, y, 0) = e^{-\frac{(x-x_0)^2+(y-y_0)^2}{\sigma}}$$

then the exact solution of the heat equation is

$$u(x, y, t) = \frac{1}{1 + 4t\kappa/\sigma} e^{-\frac{(x-x_0)^2+(y-y_0)^2}{\sigma+4t\kappa}}.$$

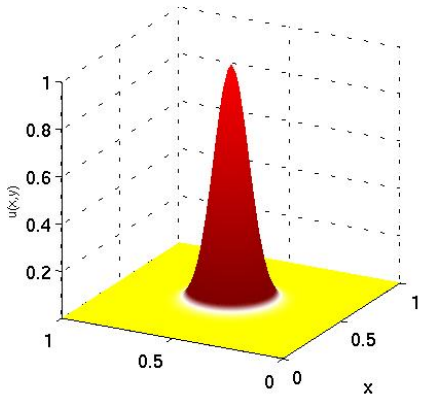

(a) time, $t = 0$

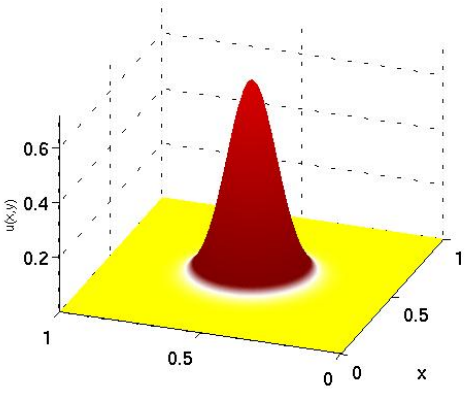

(b) time, $t = 0.1$

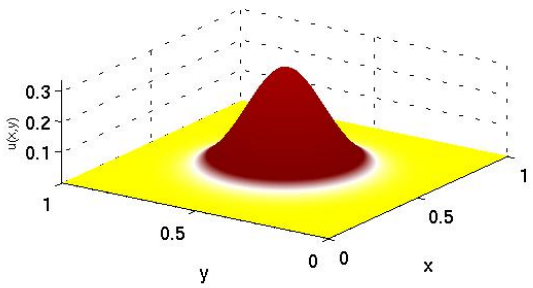

(c) time, $t = 0.5$

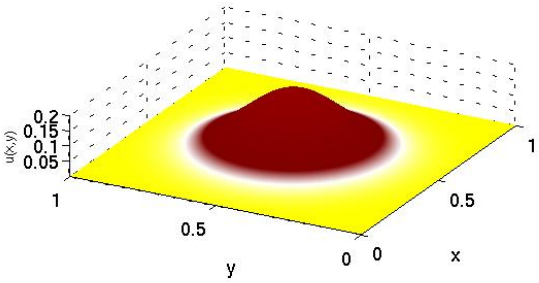

(d) time, $t = 1.0$

Figure 3.5: Heat diffusion of eq. (3.10) at $\kappa = 0.01$.

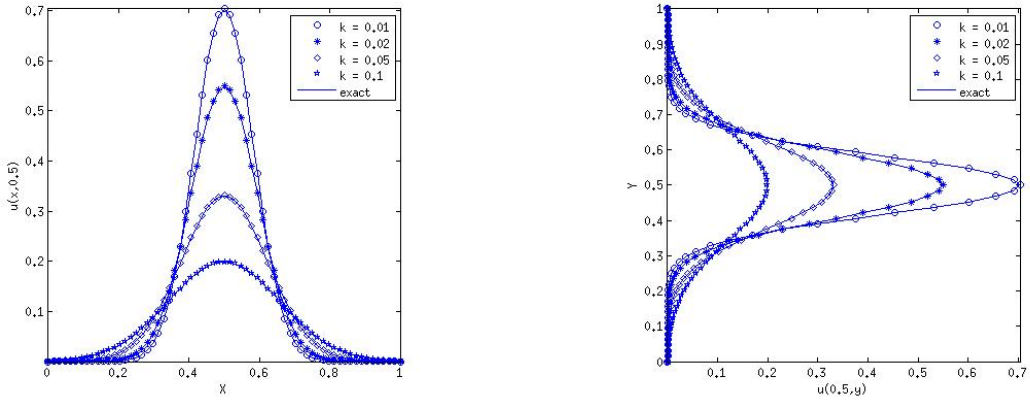

(a) $u(x, 0.5)$ along the line $y = 0.5$

(b) $u(0.5, y)$ along the line $x = 0.5$

Figure 3.6: Temperature along the center line of eq. (3.10) at $t = 0.1$.

Consider the domain $[0, 1] \times [0, 1]$, $(x_0, y_0) = (0.5, 0.5)$, $\sigma = 0.01$ and $\Delta t = 0.001$. In Figure (3.5), numerical solutions are calculated at four different times: (a) t=0; (b) t=0.1; (c) t=0.5; (d) t=1.0, using heat diffusion constant $\kappa = 0.01$ where the temperature decreases with time. Numerical solution and the exact solution, along the center line at $t = 0.1$ and $\kappa = 0.01, 0.02, 0.05$ and 0.1, are shown in Figure 3.6. The maximum error at $t = 0.1$ and $\kappa = 0.01, 0.02, 0.05$ and 0.1 are 0.000531, 0.000799, 0.001223 and 0.001329, respectively. This example analyzed with a time step, Δt, between 10^{-3} and 5×10^{-1}, where for each Δt, the resolution varies between 33×33 and 257×257. The maximum absolute errors for these various simulations for $\Delta t = 0.1$ and $\kappa = 10^{-2}$ are shown in Table 3.1.

3.5.2 A dynamical core for simulating two-dimensional flows

In this section, we solve the following two-dimensional advection-diffusion equation:

$$\frac{\partial \boldsymbol{u}}{\partial t} + \boldsymbol{u}.\nabla \boldsymbol{u} = \nu \nabla^2 \boldsymbol{u} \tag{3.12}$$

where $\boldsymbol{u} = [u, v]^T$. This non-linear advection-diffusion equation is often called two-dimensional Burger's equation because of its similarity with the Burger's equation. Many

Δt	33×33	65×65	129×129	257×257
0.5	2.57×10^{-2}	2.83×10^{-2}	2.89×10^{-2}	2.91×10^{-2}
10^{-1}	1.07×10^{-3}	7.4×10^{-5}	4.12×10^{-4}	3.9×10^{-4}
10^{-2}	1.42×10^{-3}	3.88×10^{-4}	9.3×10^{-5}	4.0×10^{-6}
10^{-3}	1.59×10^{-3}	3.93×10^{-4}	9.8×10^{-5}	8.0×10^{-6}

Table 3.1: Maximum absolute errors for different resolution and different Δt at $t = 1.0$, $\kappa = 10^{-2}$.

authors consider (3.12) as a proof of concept for their numerical scheme. Kannan & Wang (2012) and Liao (2010) used the Hopf-Cole transformation to eliminate the nonlinear term and as a result, solved a diffusion equation in order to obtain the solution of (3.12). Xie *et al.* (2010) studied a compact finite difference scheme for Burger's equation. Zhu *et al.* (2010) examined the adomian decomposition method for solving Equation (3.12). Thus, a number of reference studies are available, showing that on the avenue of solving (3.12), the search for the best method of solving 3.12 remains active.

The time discretized nonlinear system of equations, $\mathcal{L}(\boldsymbol{u}^{n+1}) = \boldsymbol{f}$, such that

$$-\nu\nabla^2\boldsymbol{u}^{n+1} + \boldsymbol{u}^{n+1}.\nabla\boldsymbol{u}^{n+1} + \frac{2}{\Delta t}\boldsymbol{u}^{n+1} = \nu\nabla^2\boldsymbol{u}^{n} - \boldsymbol{u}^{n}.\nabla\boldsymbol{u}^{n} + \frac{2}{\Delta t}\boldsymbol{u}^{n} \tag{3.13}$$

has been obtained by discretizing (3.12) in time with a Trapezoidal method. Evaluating the inner product $\langle \mathcal{L}(\boldsymbol{u}^{n+1}) - f, \tilde{\varphi}(\boldsymbol{x} - \boldsymbol{x_k})\rangle = 0$, a simultaneous nonlinear system $\mathcal{L}(\boldsymbol{u}^{n+1}(\boldsymbol{x_k})) = f(\boldsymbol{x_k})$ of $2\mathcal{N}$ algebraic equations is obtained. The discrete nonlinear system $\mathcal{L}(\boldsymbol{u}) = \boldsymbol{f}$, for simplicity, has been solved with the Newton's method (see Ortega & Rheinboldt, 1970),

$$\boldsymbol{u}^{n+1} = \boldsymbol{u}^{n} + \Delta\boldsymbol{u}$$

$$\text{such that} \quad \mathcal{J}(\boldsymbol{u}^{n})\Delta\boldsymbol{u} = f - \mathcal{L}(\boldsymbol{u}^{n})$$

where one needs to compute the Jacobian matrix $\mathcal{J}(\boldsymbol{u}^{n})$ at each iteration n. Clearly on a

mesh of $\mathcal{N}$ nodes, the computation of the product $\mathcal{J}(\boldsymbol{u}^n)\Delta\boldsymbol{u}$ between the Jacobian matrix $\mathcal{J}(\boldsymbol{u}^n)$ and the error vector $\Delta\boldsymbol{u}$ requires $\mathcal{O}(\mathcal{N}^2)$ operations. Therefore for large scale CFD applications, the implicit treatment of the the advection term is too expensive. To reduce this computational complexity as an $\mathcal{O}(\mathcal{N})$, we have considered the Frechet derivative,

$$\lim_{\eta\Delta\boldsymbol{u}\to 0} \frac{\|\mathcal{L}(\boldsymbol{u}^n + \eta\Delta\boldsymbol{u}) - \mathcal{L}(\boldsymbol{u}^n) - \mathcal{J}(\boldsymbol{u}^n)\Delta\boldsymbol{u}\|}{\|\eta\Delta\boldsymbol{u}\|}$$

which leads to the following approximation

$$\mathcal{J}(\boldsymbol{u}^n)\Delta\boldsymbol{u} \approx \frac{\mathcal{L}(\boldsymbol{u}^n + \eta\Delta\boldsymbol{u}) - \mathcal{L}(\boldsymbol{u}^n)}{\eta}$$

and as a result, $\mathcal{J}(\boldsymbol{u}^n)\Delta\boldsymbol{u}$ can be approximated with $\mathcal{O}(\mathcal{N})$ operations, where η is a small number. Numerical experiments of this thesis suggested that $\eta \leq 10^{-4}$ is sufficient. Knoll & Keyes (2004) have been reviewed this approach of solving nonlinear system of equations for multiphysics problems, in the area of CFD, it is a not commonly adopted technique. A representative example is presented below.

Using the same initial and boundary conditions as that of the reference solution (e.g. problem 1) presented by Zhu *et al.* (2010), eq. (3.12) has been solved in the domain $[0,1]\times[0,1]$, where the exact solutions are given by

$$\left.\begin{aligned} u(x,y,t) &= \tfrac{3}{4} - \tfrac{1}{4(1+e^{(-t-4x+4y)/(32\nu)})} \\ v(x,y,t) &= \tfrac{3}{4} + \tfrac{1}{4(1+e^{(-t-4x+4y)/(32\nu)})}. \end{aligned}\right\} \tag{3.14}$$

We have analyzed this example with a time step, Δt, between 10^{-1} and 10^{-4}, where for each Δt, the resolution varies between 33×33 and 129×129. Thus, we have $12.8\times10^{-3} \leq$ CFL ≤ 12.8. With CFL $= 12.8$, $\Delta t = 10^{-1}$, and $\nu = 1.25\times10^{-2}$, the maximum absolute error is 5.05×10^{-4}. In comparison, Zhu *et al.* (2010) reported a maximum absolute error 7.5×10^{-4} with $\Delta t = 10^{-4}$ and $\nu = 1.25\times10^{-2}$. This comparison, with a Δt that is 10^3 times larger than what was used by Zhu *et al.* (2010), indicates that the present collocation

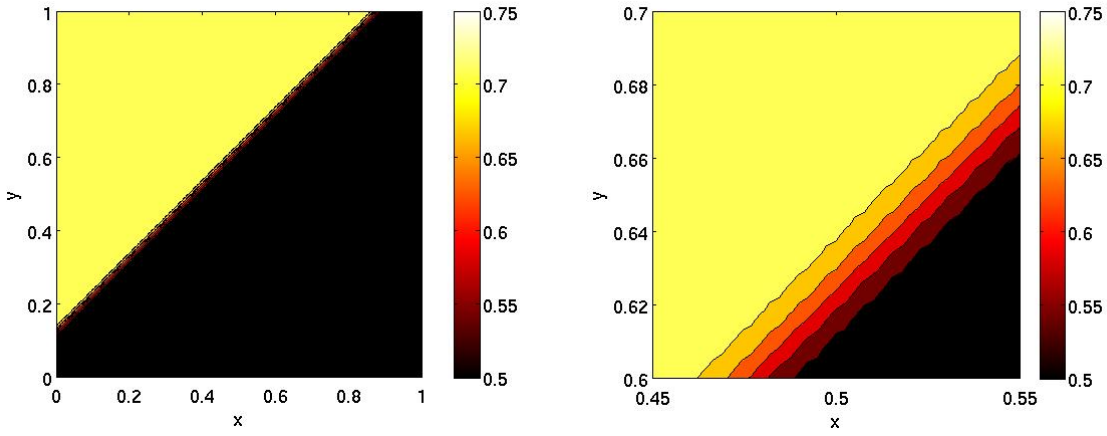

(a) $u(x, y, t)$

(b) $u(x, y, t)$ (magnified view)

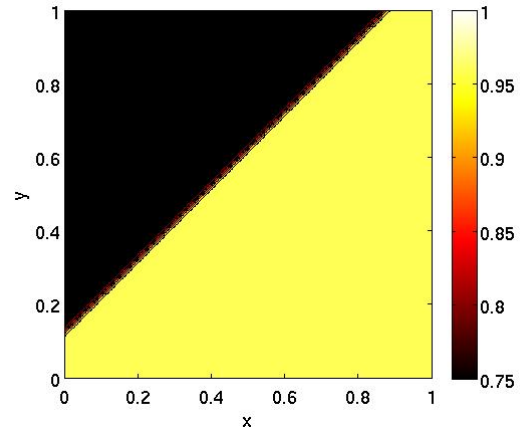

(c) $v(x, y, t)$

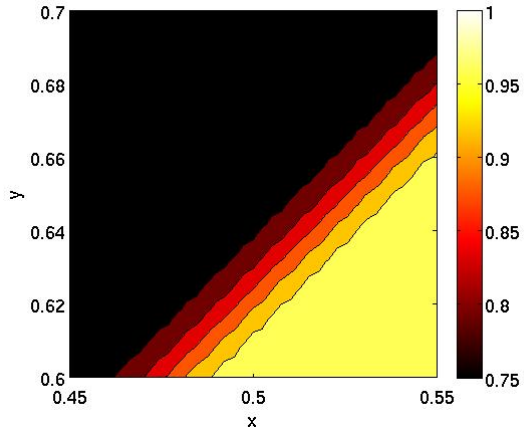

(d) $v(x, y, t)$ (magnified view)

Figure 3.7: A numerical illustration of approximation solutions of (a) (b) $u(x, y, t)$, (c) (d) $v(x, y, t)$ at $\nu = 10^{-3}$ and $t = 0.5$. (b) and (d) are the magnified view of $u(x, y, 0.5)$ and $v(x, y, 0.5)$, respectively, for a portion of the whole domain to visualize the sharp change region of the solution.

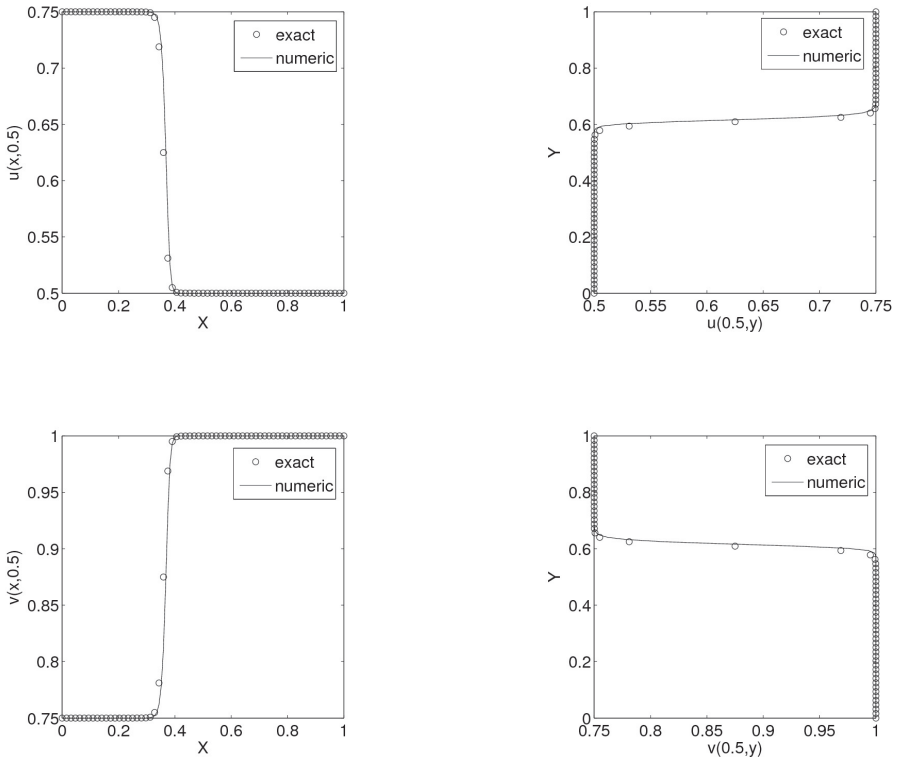

Figure 3.8: Numerical solution of (3.12) (a) $u(x, 0.5)$, (b) $u(0.5, y)$, (c) $v(x, 0.5)$, and (d) $v(0.5, y)$ at $\nu = 10^{-3}$ and $t = 0.5$.

method is able to refine the mesh at CFL $= 12.8$ without reducing the time step. For this high CFL, the error bound is equivalent to that of the scheme of Zhu *et al.* (2010). This explains the performance of the method presented by Alam *et al.* (2014) for the nonlinear advection-diffusion problem. This example puts some hint on the benefits of the proposed method.

We have also analysed the different values of ν. When $0 < \nu \ll 1$, there is a sharp change in the solution and the numerical solution become more challenging. Numerical solutions of $u(x, y)$ and $v(x, y)$ at $t = 0.5$ with $\Delta t = 10^{-3}$ and $\nu = 10^{-3}$ are shown in Figure 3.7a, 3.7b and Figure 3.7c, 3.7d, respectively. In Figure 3.8, we compare numerical solution with the exact solution (e.g., Zhu *et al.*, 2010). The plots include $u(x, 0.5)$, $u(0.5, y)$,

$v(x, 0.5)$ and $v(0.5, y)$ at $t = 0.5$ with $\Delta t = 10^{-3}$ and $\nu = 10^{-3}$. The excellent agreement between the exact and the numerical solutions with no visible oscillation encourages the methodology to the field of Computational Fluid Dynamics.

3.6 Summary

In this chapter, a weighted residual collocation method based on a diadic mesh refinement technique has been developed. A detailed description of this method is presented in Alam *et al.* (2014). A fully implicit numerical scheme has been implemented for time integration. This fully implicit discrete system is solved by projecting the solution onto a Krylov subspace. The computational complexity of this Jacobian-free Krylov method is $\mathcal{O}(\mathcal{N})$ where $\mathcal{N}$ is the number of grid-points. The excellent agreement of exact solution and numerical solution in Figure 3.6 and 3.8 is an evidence that the presented method is able to simulate a flow without artificial dissipation. This numerical method supports non-dissipative advection scheme which is an advantage of this method for simulating non-hydrostatic mesoscale circulations and which also supports a large CFL number.

In the following two chapters, this multi-scale numerical model is extended for simulating a nonhydrostatic ABL phenomena in the presence of penetrative convection, stratified turbulence, and internal waves.

Chapter 4

Penetrative convection for an isolated buoyant element

This chapter presents a form of penetrative convection in a dry atmosphere, where a relatively isolated buoyant element penetrates into an overlying stably stratified layer of fluid. To investigate this phenomenon, a thermal bubble is placed in the lower level of the atmosphere in the absence of air flow. The design of the dry thermal simulation is analogous to the simulation used by Tripoli (1992), Wicker & Skamarock (1998) and Bryan & Fritsch (2002). To describe the evolution of thermals, neutral and stable environments are considered in the dry atmosphere. During the evolution of a thermal, it interacts with its environment which involves entrainment and detrainment. Moreover, this dry convection generates internal waves that can transport momentum and energy to regions far from heat sources. Simulations for the neutrally stable environment agree with the results of Tripoli (1992), Wicker & Skamarock (1998) and Bryan & Fritsch (2002) and are verified by energy conservation, which are also shown in (Alam *et al.*, 2014) as well as in this chapter. In addition, the generation of internal waves by penetrative convection is explained for a uniformly stable environment.

4.1 Scaling analysis and parameterization

Equations (2.23) - (2.25) have been solved by considering a two-dimensional flow along with the following parameterization:

$$\frac{\partial \tau_{ij}}{\partial x_j} = K_M \frac{\partial^2 u_i}{\partial x_j^2}, \quad \text{and} \quad \frac{\partial \tau_{\theta j}}{\partial x_j} = K_H \frac{\partial^2 \theta}{\partial x_j^2},$$

where K_M is the eddy viscosity coefficient and K_H is the eddy diffusivity of heat.

Length scale, (H), is considered as the size of the element that penetrates the environment, and U is the velocity scale. The time derivative and the nonlinear advection of u_i may be estimated as

$$\frac{\partial u_i}{\partial t},\ u_j \frac{\partial u_i}{\partial x_j} \sim \frac{U^2}{H}.$$

The Coriolis force $\sim\ fU$ is neglected in comparison to the nonlinear advection terms, which are of order $\frac{U^2}{H}$.

The temperature scale $\Delta\theta$ is considered as

$$\Delta\theta \sim \frac{H H_0}{\kappa},$$

where $H_0 = \kappa \frac{\partial \theta}{\partial z}|_{z=0}$ is the initial heat flux on the surface. The time derivative and the nonlinear term of the potential temperature can be estimated as

$$\frac{\partial \theta}{\partial t},\ u_j \frac{\partial \theta}{\partial x_j} \sim \frac{\Delta\theta\, U}{H}.$$

Reynolds number, Re can be defined as

$$\frac{u_j \frac{\partial u_i}{\partial x_j}}{\frac{\partial \tau_{ij}}{\partial x_j}} \sim Re\ =\ \frac{UH}{K_M}, \quad \text{and} \quad \frac{u_j \frac{\partial \theta}{\partial x_j}}{\frac{\partial \tau_{\theta j}}{\partial x_j}} \sim \frac{UH}{K_H}\ =\ Re\, Pr,$$

where Prandtl number, $Pr = K_M/K_H$.

A list of all dimensional variables and constants, and non-dimensional parameters are presented in Table 4.1 and 4.2, respectively.

Symbol	Name of variables and constants	unit
θ	perturbation of potential temperature	K
θ_0	a reference temperature	K
β	vertical gradient of synoptic-scale potential temperature	Km^{-1}
α	thermal expansion coefficient	K^{-1}
g	acceleration due to gravity	ms^{-2}
$N = \sqrt{\frac{g}{\theta_0}\beta}$	buoyancy frequency	s^{-1}
K_M	eddy viscosity coefficient	$\mathrm{m}^2\mathrm{s}^{-1}$
K_H	eddy diffusivity of heat	$\mathrm{m}^2\mathrm{s}^{-1}$
$b = g\frac{\theta}{\theta_0}$	buoyancy for the dry atmosphere	ms^{-2}
$H_0 = \kappa\frac{\partial\theta}{\partial z}\|_{surface}$	surface heat flux	Wm^{-2}
κ	thermal conductivity of air	$\mathrm{Wm}^{-1}\mathrm{K}^{-1}$

Table 4.1: List of dimensional variables and constants.

Name of parameters	Definition
Turbulent Prandtl number, Pr	$\frac{K_M}{K_H}$
Reynolds number, Re	$\frac{UH}{K_M}$
Rayleigh number, Ra (Favre-Marinet & Tardu, 2013)	$\frac{g\alpha H_0}{K_M K_H \kappa} H^4$
Bulk Richardson number for stratified, Ri_b	$\frac{N^2 H^2}{U^2}$
Bulk Richardson number for neutral, Ri_b	$\frac{g\Delta\theta}{\theta_0 U^2}$
Froude number, Fr	$\frac{U}{HN}$

Table 4.2: List of non-dimensional parameters.

4.2 Problem description

This section presents the design of numerical experiments for penetrative convection in the atmosphere for relatively isolated buoyant elements. The simulation is two dimensional, with a domain of horizontal length 20 km and vertical length 10 km, which is the average height of the troposphere. The interior of the domain is denoted by Ω and the boundaries of the domain are denoted by $\partial\Omega$. The boundary conditions are Dirichlet type on the ground and Neumann type for all other boundaries. A schematic view of a thermal rising is presented in Figure 4.1. The initial environment is calm i.e. initial velocity is zero everywhere and the constant potential temperature is 300 K. The vertical variation of the actual and the potential temperature for the neutral environment are shown in Figure 4.1(a). A warm perturbation temperature θ is placed at the center of the domain, which is specified by

$$\theta(x, z, 0) = \exp(-((x - x_c)^2 + (z - z_c)^2)/\xi)$$

where, $x_c = 0$ km, $z_c = 2$ km and $\xi = 1$. That is, the maximum buoyancy is placed at the center of the thermal, which decreases exponentially to 0 outside the edge of the thermal. This warm perturbation creates a stable region on the lower half of the warm place and an unstable region on the upper half of the warm place, which is shown in Figure 4.1(b). The interaction of buoyancy force and gravity force in the warm region is presented in Figure 4.1(c). The buoyancy force is larger than the gravity force, and as a result warm air parcels move up which causes penetrative turbulence. The expected air flow for this thermal perturbation is presented in Figure 4.1(d).

As demonstrated schematically in Figure 4.1, the buoyant element is expected to initiate a counter clockwise circulation near the left half of the element. Similarly, at the right half plane, it initiates clockwise circulation. This is because whenever a moving fluid enters a quiescent region of the same fluid a shear is created between two regions, and

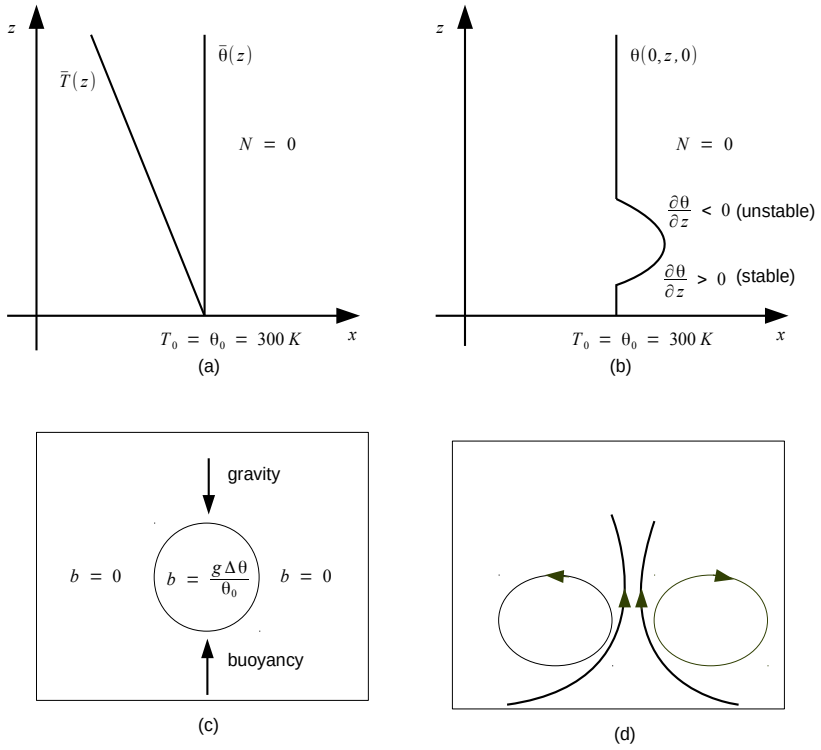

Figure 4.1: (a) vertical variation of the actual and potential temperature, (b) introduce a perturbation for potential temperature, (c) effect of buoyancy and gravity and (d) expected circulation.

this causes turbulence and mixing. Since the motion in this case is primarily vertical, to first order $\frac{\partial u}{\partial z} \sim 0$, $\frac{\partial w}{\partial x} > 0$ on the left and $\frac{\partial w}{\partial x} < 0$ on the right. So spanwise vorticity, $\omega \sim \frac{\partial w}{\partial x} - \frac{\partial u}{\partial z} > 0$ on the left and $\omega \sim \frac{\partial w}{\partial x} - \frac{\partial u}{\partial z} < 0$ on the right. These cyclonic and anticyclonic circulations are primarily agents to initiate heat, mass and momentum transfer, causing turbulence mixing.

4.3 Results

4.3.1 Reference model

A simulation presented by Bryan & Fritsch (2002), Wicker & Skamarock (1998) and Carpenter *et al.* (1990) is considered as a reference model. The initial temperature perturbation of the present model is a Gaussian function; however, a square of a cosine function is used in the reference model. The governing equations of the reference model presented by Bryan & Fritsch (2002) are similar to the equations (2.23-2.25) for the dry atmosphere. The boundary conditions of the reference model are implemented by constructing three artificial zones beyond the physical boundaries of the domain. However, the boundary conditions of the present model do not require these artificial zones due to the novel discretization process which is described in Chapter 3.

4.3.2 Case design of numerical experiments

Two cases of thermal evolution are considered. In the first case, a neutrally stratified environment is considered which is similar to the dry warm thermal simulation presented by Bryan & Fritsch (2002), and in the second case, a stable environment is considered which is similar to the model of dry thermals in a stable environment presented by Lane (2008). The first case deals with the vertical motion of a buoyant element, where the lapse rate of temperature is 10^0 C/km for neutral stratification. This is an idealization of the atmosphere, and the main purpose is to verify the present numerical model. Such idealization helps to compare the present result with the reference model presented in section 4.3.1.

If the eddy viscosity is the limiting factor, then the convective velocity w can be estimated by comparing

$$K_M \frac{\partial^2 w}{\partial z^2} \sim \frac{g\theta}{\theta_0}$$

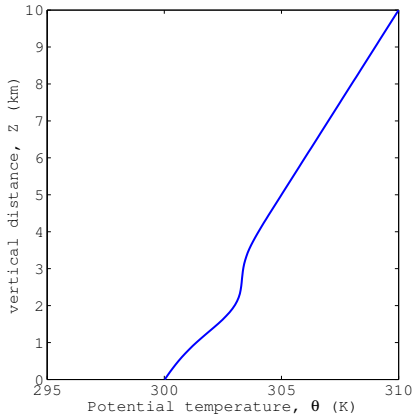

Figure 4.2: The initial vertical variation of the potential temperature in stable atmosphere.

which implies

$$w \sim \frac{g\Delta\theta H^2}{\theta_0 K_M}.$$

To examine the flow dependence of eddy viscosities, two sub-cases, Case I and Case II, are designed based on different eddy viscosities. For these different eddy viscosities, I will examine whether the present model is able to resolve the flow or not. In case I, the turbulent Prandtl number $Pr = 0.71$ is fixed and four eddy viscosities such as $K_M = 10,\ 5\ ,\ 2.5$ and $1.0\ \mathrm{m^2 s^{-1}}$ for $\theta_0 = 300\ \mathrm{K}$ are considered. For case II, three eddy viscosities, such as, $K_M = 10, 5$ and $2.5\ \mathrm{m^2 s^{-1}}$ for $K_H = 5\ \mathrm{m^2 s^{-1}}$, $\theta_0 = 300\ \mathrm{K}$ are considered. The corresponding values of K_H, Re, and Ra are presented in Table 4.4. The simulations have been done by using the number of grid points $\mathcal{N} = 129 \times 129$, 257×257 and 513×513 and Δt is between 0.01 to 0.5. The minimum grid sizes corresponding to K_M for $Pr = 0.71$ are presented in Table 4.3. The number of grid points $\mathcal{N} = 513 \times 513$ i.e. $39\ \mathrm{m}$ horizontal grid spacing and $19.5\ \mathrm{m}$ vertical grid spacing are used for the presented results.

In the second case, a stable environment is considered instead of a neutral environment. The initial vertical variation of the potential temperature in a stable atmosphere is shown in Figure 4.2. The aim of this case is to observe the internal waves due to penetrative convec-

K_M $(\mathrm{m^2 s^{-1}})$	Resolution
10	257×257
5	257×257
2.5	513×513
1.0	513×513

Table 4.3: Minimum grid size corresponding to K_M for $Pr = 0.71$.

tion. The wave frequency of the internal wave is correlated with buoyancy frequency. To study this case, six different buoyancy frequencies are considered, and the other parameters are fixed. The representative parameters in this case are listed in Table 4.5. In this case, the number of grid points $\mathcal{N} = 257 \times 257$ are used.

4.3.3 Penetrative turbulent convection in a neutral environment

This section deals with penetrative convection in a neutral environment, i.e. the atmosphere consists of air parcels all having the same internal energy. The temperature decreases vertically at the adiabatic lapse rate, and the stratification parameter vanishes, $N = 0$. At initial stage, the thermal plume begins to rise. After a certain period of time, two 'rotors' develop on the sides of the thermal and the perturb temperature decreases as a function of time. The results of two cases are considered here. Potential temperature perturbation (θ) for $\theta_0 = 300$ K, $K_M = 10\ \mathrm{m^2 s^{-1}}$ and $K_H = 14.1\ \mathrm{m^2 s^{-1}}$ at $t = 0,\ 400,\ 600,\ 800,\ 1000$ and 1200 s are shown in Figure 4.3. The thermal rises and expands over time, which is similar to the results of dry thermal rising presented in Wicker & Skamarock (1998) and Bryan & Fritsch (2002). In Bryan & Fritsch (2002), $\theta_{min} = -0.144409K$ and $\theta_{max} = 2.07178K$ at $\theta_0 = 300$ K for dry thermal simulation. These extreme values are closer to the present case for $K_M = 1.0\ \mathrm{m^2 s^{-1}}$ and

	K_M ($\mathrm{m^2 s^{-1}}$)	K_H ($\mathrm{m^2 s^{-1}}$)	Re	Ra	Pr
Case I	10	14.1	2.5×10^3	4.44×10^6	0.71
	5	7.04	5.0×10^3	1.78×10^7	0.71
	2.5	3.52	1.0×10^4	7.1×10^7	0.71
	1.0	1.41	2.5×10^4	4.44×10^8	0.71
Case II	10	5	2.5×10^3	4.44×10^6	0.5
	5	5	5.0×10^3	1.78×10^7	1.0
	2.5	5	1.0×10^4	7.1×10^7	2.0

Table 4.4: Representative parameters for the simulations of a neutral environment case where Re is Reynolds number, Ra is Rayleigh number, Pr is Prandtl number and $Ri_b = 0.1$ is the bulk Richardson number.

Ri_b	Fr	N ($\mathrm{s^{-1}}$)
1.0	1.0	2.5×10^{-2}
0.25	2.0	1.25×10^{-2}
0.2	2.24	1.12×10^{-2}
0.16	2.5	1.0×10^{-2}
0.1	3.16	7.9×10^{-3}
0.05	4.47	5.6×10^{-3}

(a) Ri_b, Fr and N

Name of parameters	values
K_M	$10\ \mathrm{m^2 s^{-1}}$
K_H	$14.1\ \mathrm{m^2 s^{-1}}$
Reynolds number, Re	2.5×10^3
Rayleigh number, Ra	4.44×10^6
Prandtl number, Pr	0.71

(b) Other parameters

Table 4.5: Representative parameters for the simulations of the stable environment case.

K_M	10 m^2s^{-1}	5 m^2s^{-1}	2.5 m^2s^{-1}	1.0 m^2s^{-1}	B & F
$\theta_{\min}$(K)	-0.000632	-0.003814	-0.009359	-0.133971	-0.144409
$\theta_{\max}$(K)	1.408749	1.629635	1.843659	2.138108	2.07178
$u_{\min}(ms^{-1})$	-9.511412	-10.058257	-10.636190	-11.667357	-
$u_{\max}(ms^{-1})$	9.512040	10.059020	10.637147	11.668235	-
$w_{\min}(ms^{-1})$	-6.360285	-6.527770	-6.596165	-6.627753	-8.58069
$w_{\max}(ms^{-1})$	15.352078	15.599483	15.833058	16.018170	14.5396
$\omega_{\min}(s^{-1})$	-0.065906	-0.095523	-0.137061	-0.188188	-
$\omega_{\max}(s^{-1})$	0.065906	0.095523	0.137049	0.188187	-

Table 4.6: Extreme values of dry thermal simulation for $Pr = 0.71$, $\theta_0 = 300$ K at $t = 1000$ s. Extreme values are compared with that from Bryan & Fritsch (2002) (B & F).

$K_H = 1.41$ m^2s^{-1}. Temperature perturbations for $K_M = 10$ m^2s^{-1}, $K_M = 5$ m^2s^{-1} and $K_M = 2.5$ m^2s^{-1} are presented in Figure 4.4. Magnitude of temperature perturbation increases as eddy viscosity decreases as well as the magnitude of the extreme values of perturb temperature increases a little when eddy viscosity decreases for a fixed time. The movement of the 'rotors' is slightly faster when the eddy viscosity K_M becomes smaller. When K_M decreases, the bubble slightly moves up, and for $K_M = 10,\ 5,\ 2.5$ m^2s^{-1} at $t = 1000$ s it reaches about $8.04,\ 8.08,\ 8.15$ km, respectively.

In case II, three different eddy viscosities such as $K_M = 10, 5$ and 2.5 m^2s^{-1} for fixed $K_H = 5$ m^2s^{-1}, $\theta_0 = 300$ K are considered. The temperature perturbation profile for Case II is similar to Case I. The corresponding values of K_H, Re, and Ra are presented in the Case II section in Table 4.4. In this case, the change in temperature perturbation is not significant as in Case I.

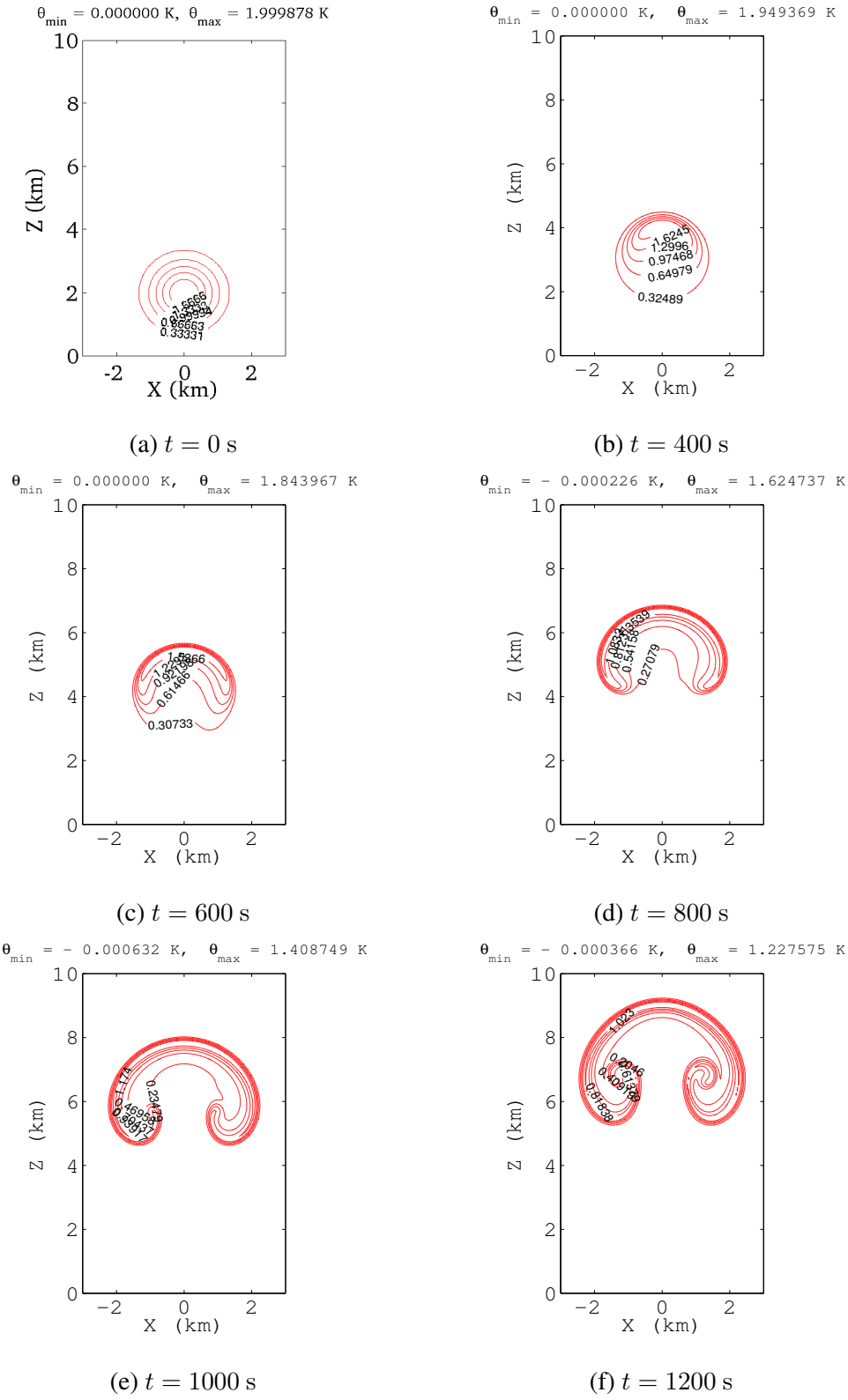

(a) $t = 0$ s (b) $t = 400$ s

(c) $t = 600$ s (d) $t = 800$ s

(e) $t = 1000$ s (f) $t = 1200$ s

Figure 4.3: Perturbation of potential temperature (θ) for $\theta_0 = 300$ K, $K_M = 10$ m^{2}s^{-1} and $K_H = 14.1$ m^{2}s^{-1} at (a) $t = 0$ s, (b) $t = 400$ s, (c) $t = 600$ s, (d) $t = 800$ s, (e) $t = 1000$ s and (f) $t = 1200$ s is contoured.

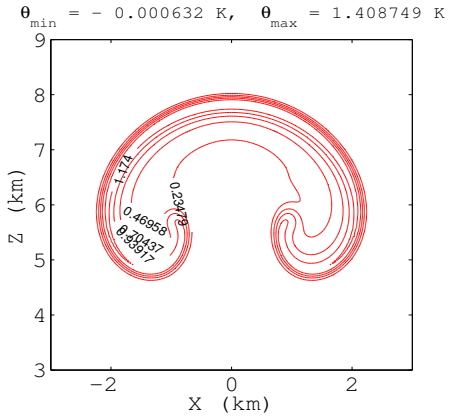

(a)

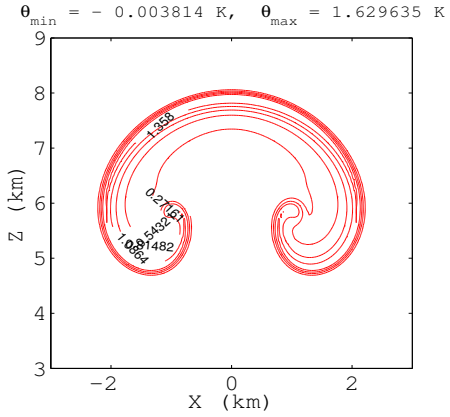

(b)

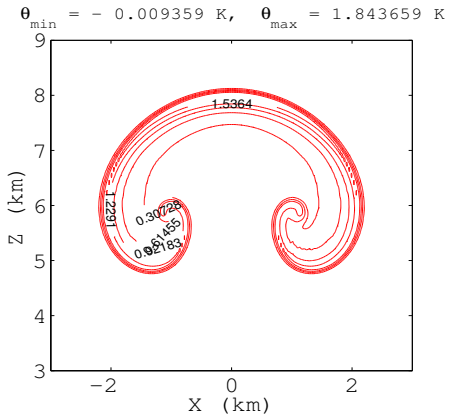

(c)

Figure 4.4: Perturbation of potential temperature (θ) for $\theta_0 = 300$ K, $Pr = 0.71$, (a) $K_M = 10$ m^{2}s^{-1}, $K_H = 14.1$ m^{2}s^{-1}; (b) $K_M = 5$ m^{2}s^{-1}, $K_H = 7.04$ m^{2}s^{-1} and (c) $K_M = 2.5$ m^{2}s^{-1}, $K_H = 3.52$ m^{2}s^{-1} at 1000 s is contoured.

K_M	10 m^2s^{-1}	5 m^2s^{-1}	2.5 m^2s^{-1}
$\theta_{\min}$(K)	-0.0061	-0.0062	-0.0063
$\theta_{\max}$(K)	1.7138	1.7268	1.7371
$u_{\min}(ms^{-1})$	-9.7735	-10.1486	-10.4817
$u_{\max}(ms^{-1})$	9.7744	10.1494	10.4824
$w_{\min}(ms^{-1})$	-6.5080	-6.5204	-6.5481
$w_{\max}(ms^{-1})$	15.4442	15.6334	15.8046
$\omega_{\min}(s^{-1})$	-0.0849	-0.1053	-0.1271
$\omega_{\max}(s^{-1})$	0.0849	0.1053	0.1271

Table 4.7: Extreme values of dry thermal simulation for fixed $K_H = 5\ m^2s^{-1}$, $\theta_0 = 300$ K at $t = 1000$ s.

4.3.4 Entrainment in a neutral environment

The mixing of air which causes this thermal rising is determined by the velocity induced by the turbulent vorticities and is called entrainment. Horizontal velocity and vertical velocity are presented in Figure 4.5 based on the representative parameters for Case I in Table 4.4. Red, blue and yellow colors represent positive, negative and zero, respectively, from Figure 4.5 to onwards for a contour plot. Velocity profiles are symmetric about $x = 0$. The extreme values of horizontal velocity, vertical velocity and temperature perturbation for different eddy viscosities are shown in Table 4.6. For comparison, maximum and minimum values of vertical velocity and temperature perturbation from Bryan & Fritsch (2002) for dry simulation are also presented in Table 4.6. The magnitude of velocity components slightly increases as eddy viscosity decreases. In this table, the vertical velocities for $K_M = 10, 5, 2.5, 1\ m^2s^{-1}$ are $15.352078, 15.599483$, 15.833058 and $16.018170\ ms^{-1}$, respectively. When the thermal rises it pulls surrounding fluid. It is a frictional effect and

hence is associated with vorticity. The vertical velocity has no significant change; however, the eddy viscosity changes by about a factor of 2. The vorticity, $\omega = \partial w/\partial x - \partial u/\partial z$, of the eddy viscosities, $K_M = 10, 5, 1\ \mathrm{m^2 s^{-1}}$, are shown in Figure 4.7. In this figure, the blue color represents clockwise rotation and the red color represents the counter-clockwise rotation. The vorticity and velocity profiles for Case II are similar to the profiles of Case I. The extreme values for Case II are presented in Table 4.7. The changes in velocities and vorticities for different eddy viscosities are also not remarkable like in Case I. Hence, it can be concluded that in a situation where turbulence penetrates upward, the main characteristics of the flow do not depend on eddy viscosities.

In order to provide further insight into the quality of this simulation, the stream lines at $t = 400,\ 600,\ 800, 1000, 1200$ s for $K_M = 10\ \mathrm{m^2 s^{-1}}$ are presented in Figure 4.6. These contour plots exhibit the vertical migration of two counter rotating patterns, where the left vortex is counter clockwise, and the right vortex is clockwise.

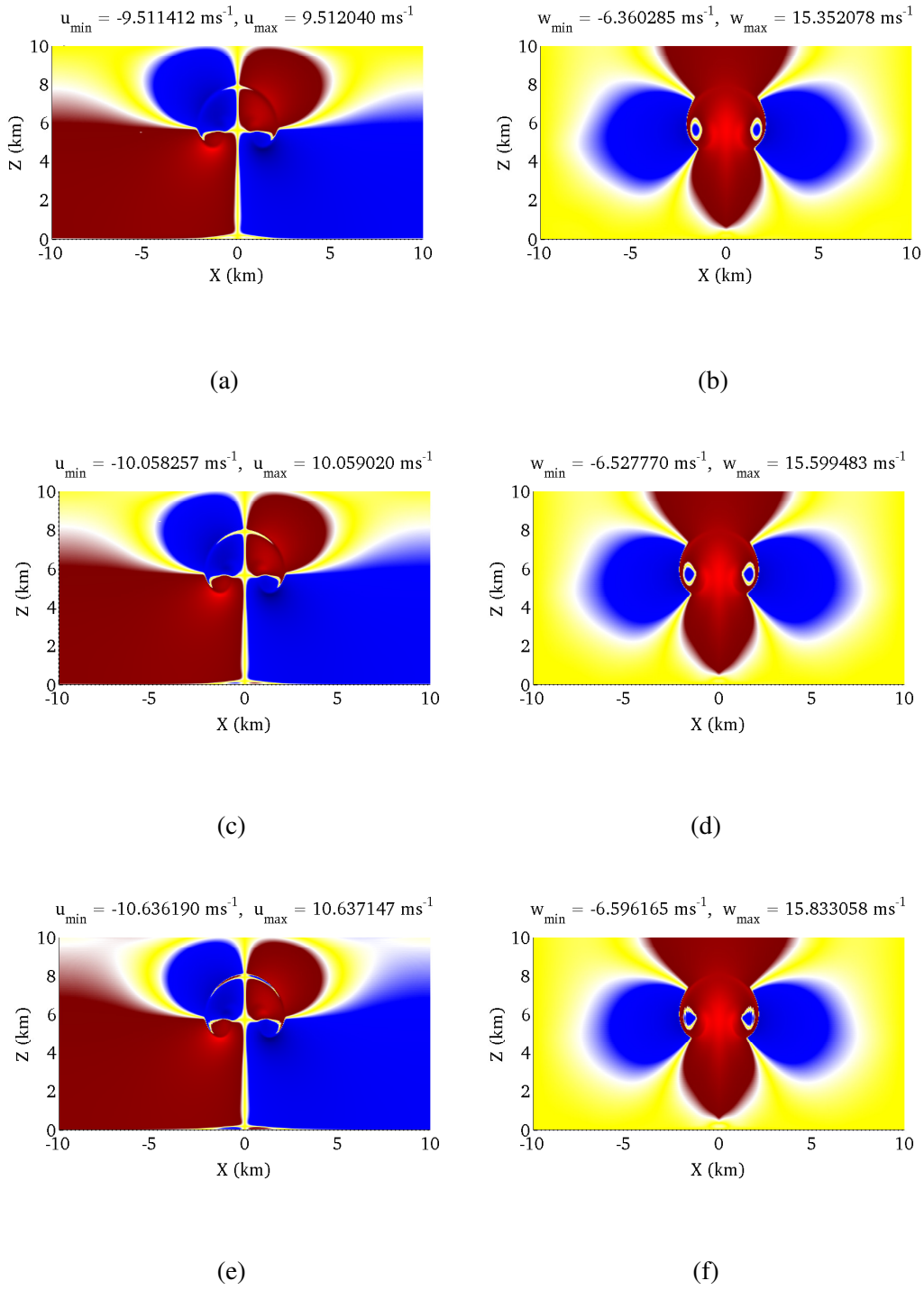

Figure 4.5: Horizontal velocity (u) ms^{-1} for (a) $K_M = 10\ \mathrm{m}^2\mathrm{s}^{-1}$, (c) $K_M = 5\ \mathrm{m}^2\mathrm{s}^{-1}$ and (e) $K_M = 2.5\ \mathrm{m}^2\mathrm{s}^{-1}$ and vertical velocity (w) ms^{-1} for (b) $K_M = 10\ \mathrm{m}^2\mathrm{s}^{-1}$, (d) $K_M = 5\ \mathrm{m}^2\mathrm{s}^{-1}$ and (f) $K_M = 2.5\ \mathrm{m}^2\mathrm{s}^{-1}$ at $Pr = 0.71$, $\theta_0 = 300$ K and 1000 s. Unless otherwise stated red, blue and yellow colors represent positive, negative and zero, respectively.

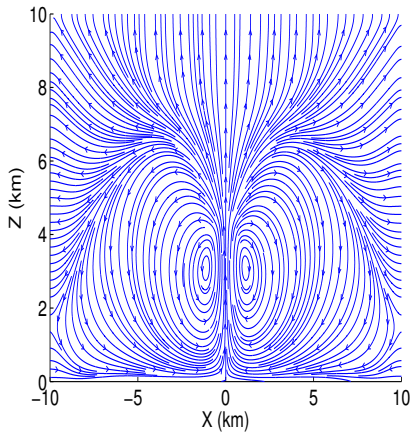

(a) $t = 400$ s

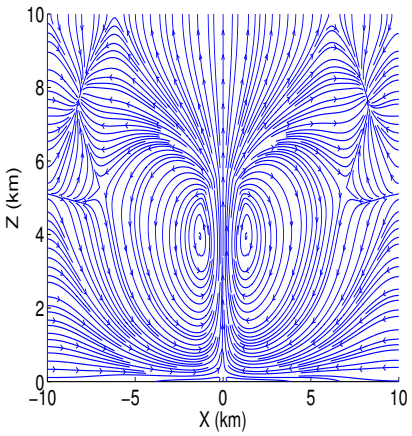

(b) $t = 600$ s

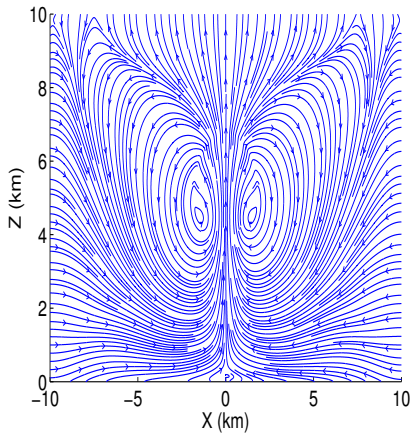

(c) $t = 800$ s

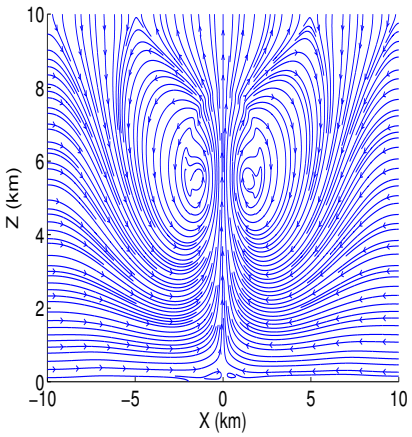

(d) $t = 1000$ s

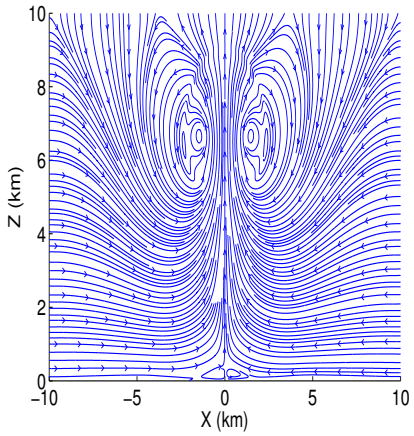

(e) $t = 1200$ s

Figure 4.6: Streamlines for the dry thermal rising for $\theta_0 = 300$ K, $K_M = 10$ m^{2}s^{-1}, $Pr = 0.71$ at $t = 400,\ 600,\ 800,\ 1000,\ 1200$ s.

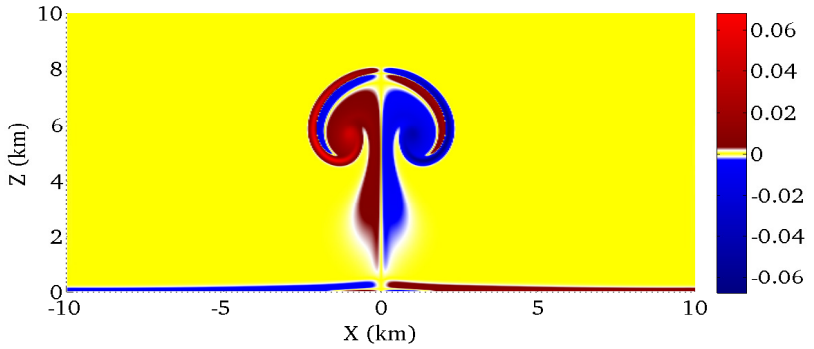

(a)

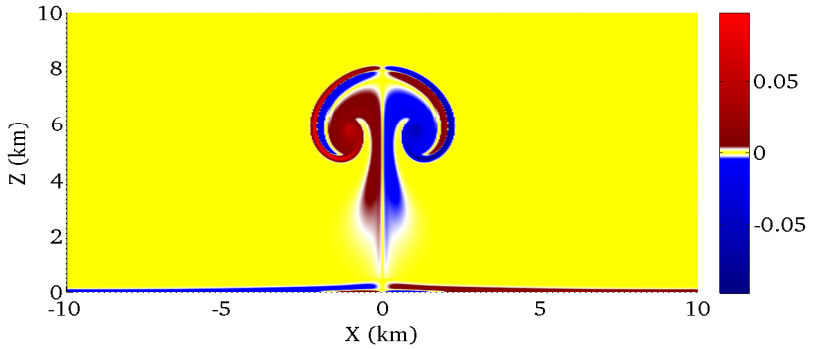

(b)

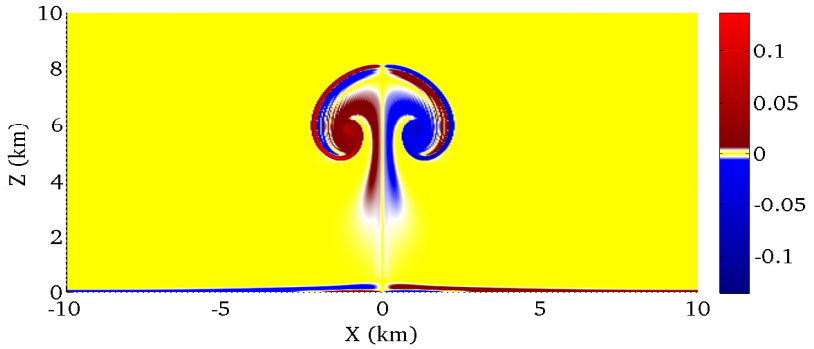

(c)

Figure 4.7: Spanwise vorticity (ω) s^{-1} for $\theta_0 = 300$ K, $Pr = 0.71$, (a) $K_M = 10$ $\mathrm{m}^2\mathrm{s}^{-1}$, (b) $K_M = 5$ $\mathrm{m}^2\mathrm{s}^{-1}$ and (c) $K_M = 1$ $\mathrm{m}^2\mathrm{s}^{-1}$ at 1000 s.

4.3.5 Stable environment

This section deals with the dynamics of a thermal rising in a stable environment. When a warm air parcel is placed in a stable environment it rises adiabatically and it expands and releases temperature. When a parcel reaches its maximum level of expansion, where the temperature of this air parcel is lower than the surrounding air, it descends towards its original level but it overshoots this level due to the momentum gained, and continues to its warmest level adiabatically. Again it overshoots upward. This process continues until the temperature of the warm air parcel and the surrounding air becomes the same. Linear theory suggests that (see Lin, 2007, p. 187)

$$\frac{2\pi}{N} > \frac{L}{U}$$

for the evanescent flow regime. When $\frac{2\pi}{N} >> \frac{L}{U}$ the buoyancy force become extremely weaker, and in this case

$$w(x,z) = W(x)e^{-k|z|}.$$

On the other hand,

$$\frac{2\pi}{N} < \frac{L}{U}$$

for the vertical propagating wave regime. For the considered length scale $L \sim 1$ km, velocity scale $U \sim 10$ ms^{-1} and the values of N presented in Table 4.5a implies $\frac{2\pi}{N} > \frac{L}{U}$ which represents the evanescent flow regime.

The profiles of the vertical velocity at $x = 0$, (a) $t = 600$ s, (b) $t = 800$ s, (c) $t = 1000$ s and (d) $t = 1200$ s in a stratified environment are shown in Figure 4.8a, 4.8b, 4.8c and 4.8d, respectively. Figure 4.8 shows $w(0,z)$ is about the same and vanishes for $N = 7.9 \times 10^{-3}$ s^{-1} and $N = 5.6 \times 10^{-3}$ s^{-1} for which $\frac{2\pi}{N}$ increases. Similarly, the profiles of the potential temperature at the same position and time are shown in Figure 4.9. The amplitude of the disturbance of vertical velocity and the perturbation of potential

temperature decreases with time. The amplitude of the disturbance of vertical velocity is larger for larger N. However, the amplitude of the perturbation of potential temperature is larger for smaller N.

The diameter of the initial perturbed potential temperature is $4\ \mathrm{km}$ and the maximum perturbed potential temperature is placed at the position $(0\ \mathrm{km}, 2\ \mathrm{km})$. In Figure 4.8 and 4.9, the maximum perturbation of vertical velocity and potential temperature appear around $2\ \mathrm{km}$ vertical height. In contrast to neutral case where warm air rises up adiabatically, warm air in the stable environment is overshoot. Figure 4.8 and 4.9 indicate this overshooting place is around $5\ \mathrm{km}$ from the surface.

4.3.6 Internal wave excitation in a stratified environment

In this section, the internal mesoscale waves due to penetrative convection are investigated in a stably stratified environment. Due to this penetration, the vertical velocity is evolved. For $U \sim 10\ \mathrm{ms}^{-1}$ and $N \sim 1.0 \times 10^{-2}\ \mathrm{s}^{-1}$ implies the vertical wavelength, $L_z = \frac{2\pi U}{N} \sim 6.25\ \mathrm{km}$. The evolution of vertical velocity at $x = 0$, $z = 6.25\ \mathrm{km}$ in the stable case where $N = 2.5 \times 10^{-2}, 1.25 \times 10^{-2}, 1.12 \times 10^{-2}, 1.0 \times 10^{-2}, 7.9 \times 10^{-3}, 5.6 \times 10^{-3}$ are shown in Figure 4.10. For each N, the corresponding bulk Richardson numbers Ri_b are presented in Table 4.5a. The amplitude of the waves decreases as N decreases. For the large value of N, waves are damping oscillatory, and the damping factor is reduced while the value of N decreases. The waves for the fixed horizontal position $x = 0$ and the different vertical positions $z = 1.25, 2.5, 3.75, 5.0, 6.25, 7.5, 8.75\ \mathrm{km}$ are presented in Figure 4.11. To compare the amplitude of the waves, the waves in different vertical positions are shown in same frame, which are depicted in Figure 4.11a, 4.11c, and 4.11e and Figure 4.11b, 4.11d, and 4.11f show the waves in different vertical positions. In the lower height, waves are damping oscillatory, and the damping factor reduces with an increase of height. The

N (s^{-1})	ω/N	α
2.5×10^{-2}	0.999	2.56^0
1.25×10^{-2}	0.997	4.44^0
1.12×10^{-2}	0.985	9.94^0
1.0×10^{-2}	0.977	12.3^0
7.9×10^{-3}	0.962	15.8^0
5.6×10^{-3}	0.929	21.7^0

Table 4.8: ω/N at $z = 6.25$ km.

thermal dynamics and detrainment to reduce the amplitude and horizontal gradient of the potential temperature, thereby reducing the amplitude of the internal waves. Therefore, the thermal behaves like a damped oscillator, which is also suggested by Morton *et al.* (1956).

At $Ri_b = 1.0$, waves at a small height become extinct after a certain period of time; however, the waves of upper vertical heights are propagating. In a critical bulk Richardson number, $Ri_b = 0.25$ or a Richardson number lower than the critical number, say $Ri_b = 0.16$, the waves do not behave like this. In this case, the waves do not die out and they can propagate in the upper layers in the atmosphere. In Figure 4.10, wave frequency(ω) is computed and the ratios of wave frequency and buoyancy frequency (ω/N) at $z = 6.25$ km are shown in Table 4.8. The frequency ω is marginally less than that of the environment. The angle (α) between the phase velocity vector and the horizontal direction are also presented in Table 4.8. This angle is computed by using the dispersion relation which is stated in eq. (2.33). In this table, the wave frequency lies in $\omega < N$, and the maximum possible frequency of internal waves in a stratified fluid is N. The angle (α) increases as buoyancy frequency decreases. For a given stratification, waves with constant $\omega < N$ propagate at a fixed angle to the horizontal axis.

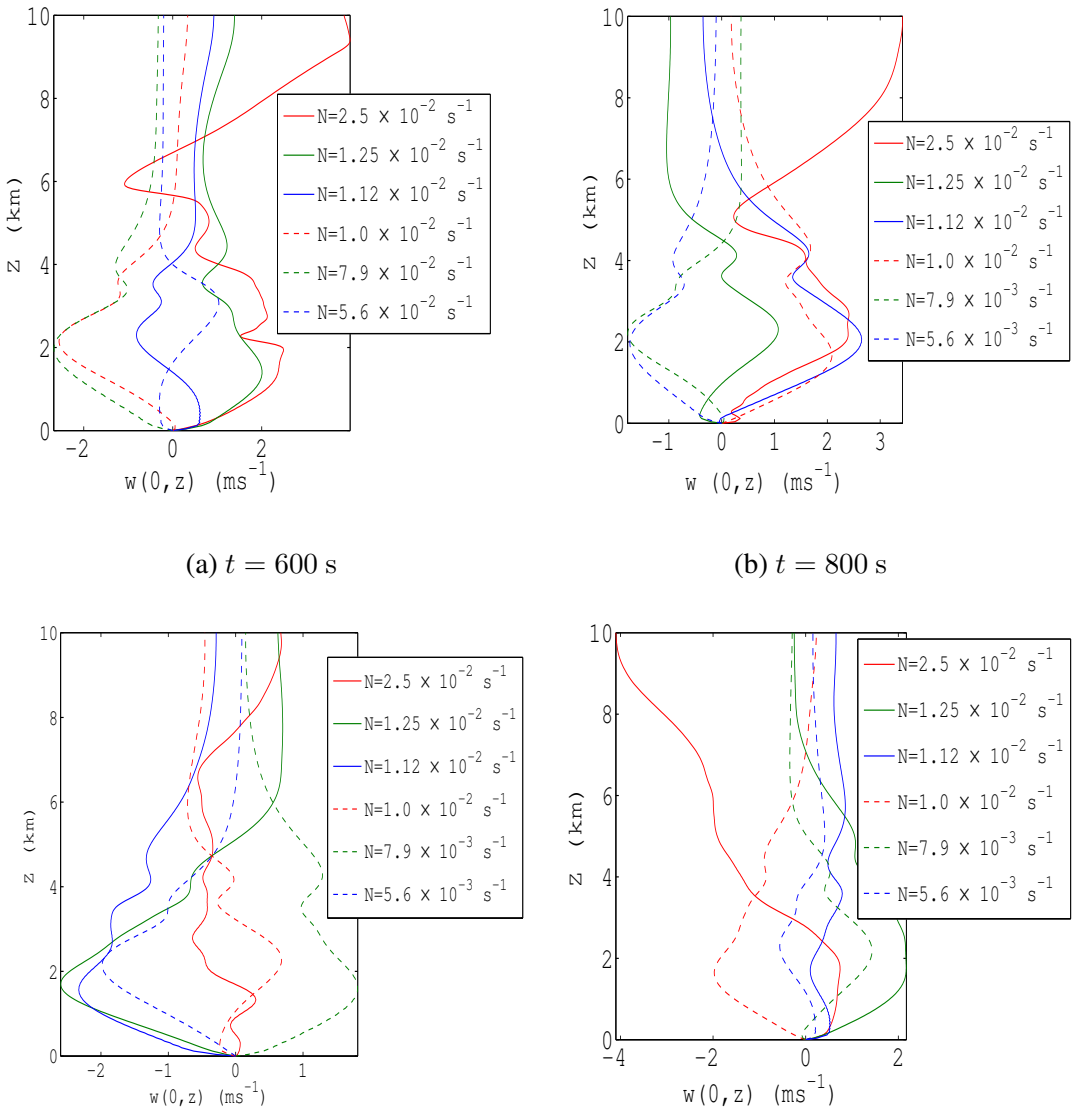

(a) $t = 600$ s

(b) $t = 800$ s

(c) $t = 1000$ s

(d) $t = 1200$ s

Figure 4.8: Profiles of the vertical velocity at $x = 0$, (a) $t = 600$ s, (b)$t = 800$ s, (c) $t = 1000$ s and (d) $t = 1200$ s for $K_M = 10$ m^{2}s^{-1}, $K_H = 14.1$ m^{2}s^{-1} in a stratified environment.

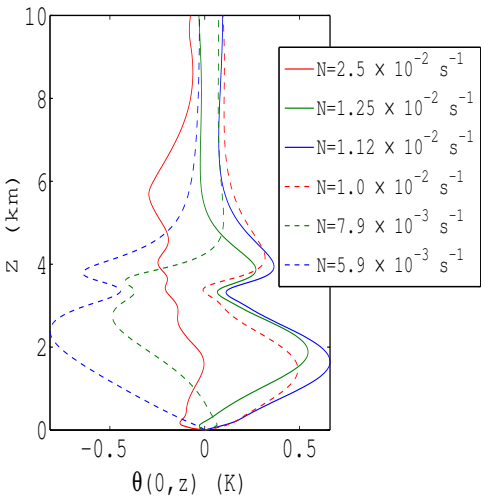

(a) $t = 600$ s

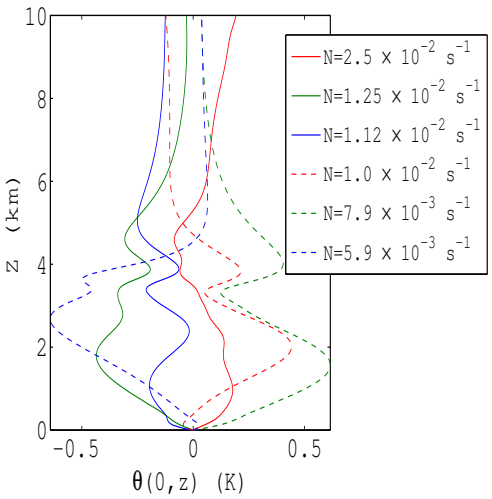

(b) $t = 800$ s

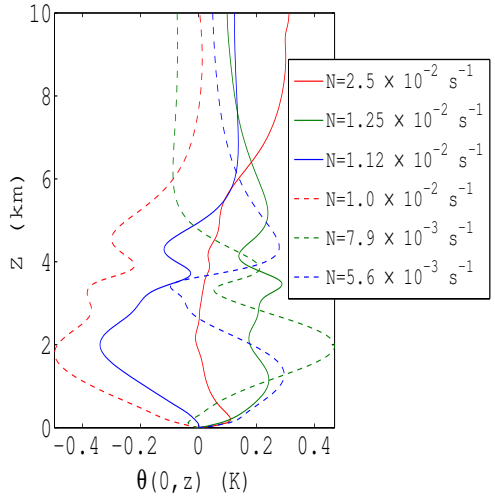

(c) $t = 1000$ s

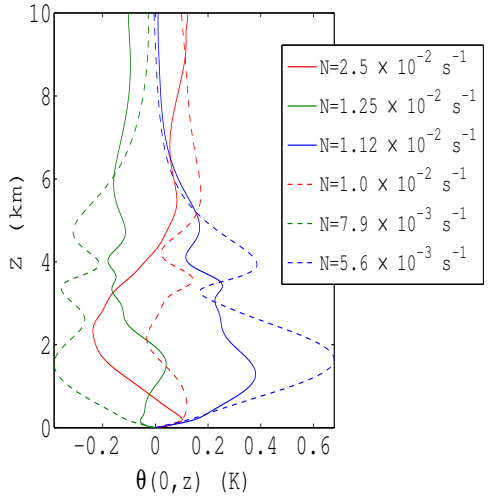

(d) $t = 1200$ s

Figure 4.9: Profiles of the potential temperature at $x = 0$, (a) $t = 600$ s, (b)$t = 800$ s, (c) $t = 1000$ s and (d) $t = 1200$ s for $K_M = 10$ m^{2}s^{-1}, $K_H = 14.1$ m^{2}s^{-1} in a stratified environment.

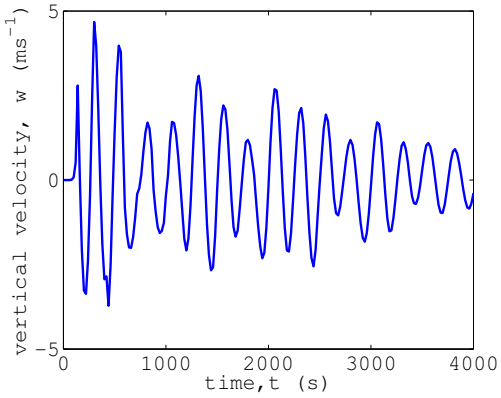

(a) $N = 2.5 \times 10^{-2}\ \mathrm{s}^{-1}$

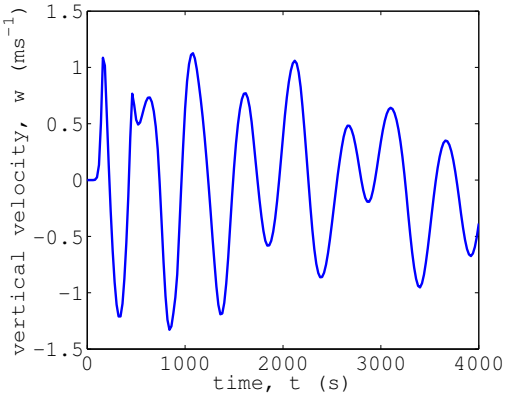

(b) $N = 1.25 \times 10^{-2}\ \mathrm{s}^{-1}$

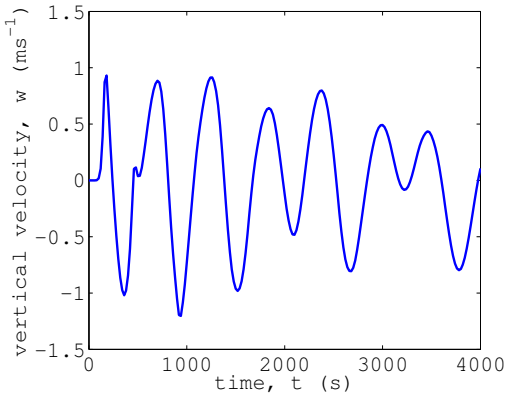

(c) $N = 1.12 \times 10^{-2}\ \mathrm{s}^{-1}$

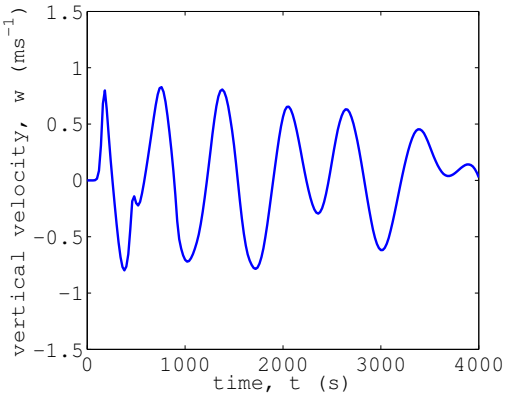

(d) $N = 1.0 \times 10^{-2}\ \mathrm{s}^{-1}$

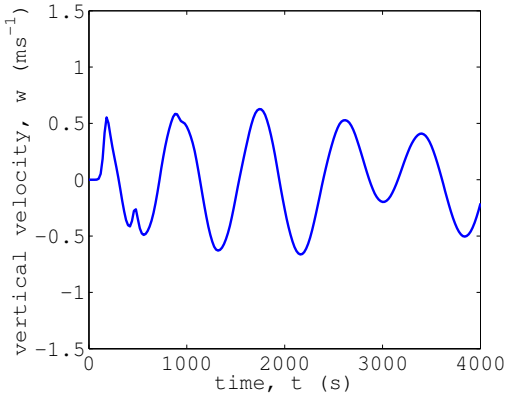

(e) $N = 7.9 \times 10^{-3}\ \mathrm{s}^{-1}$

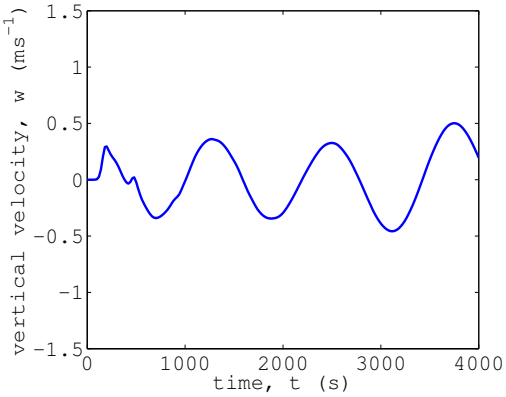

(f) $N = 5.6 \times 10^{-3}\ \mathrm{s}^{-1}$

Figure 4.10: Evolution of vertical velocity at $x = 0$, $z = 6.25$ km for the stable case (a) $N = 2.5 \times 10^{-2}\ \mathrm{s}^{-1}$, (b) $N = 1.25 \times 10^{-2}\ \mathrm{s}^{-1}$, (c) $N = 1.12 \times 10^{-2}\ \mathrm{s}^{-1}$, (d) $N = 1.0 \times 10^{-2}\ \mathrm{s}^{-1}$, (e) $N = 7.9 \times 10^{-3}\ \mathrm{s}^{-1}$ and (f) $N = 5.6 \times 10^{-3}\ \mathrm{s}^{-1}$. The corresponding dispersion relation is evaluated in Table 4.8.

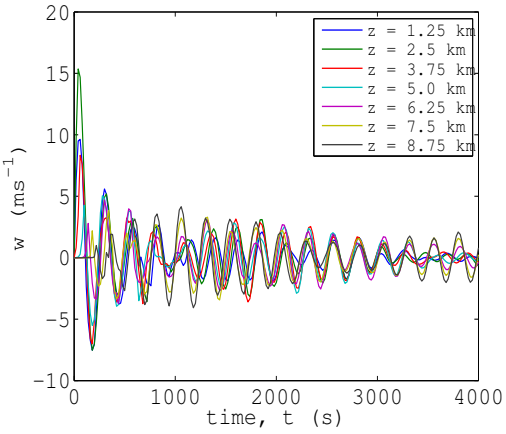

(a) $Ri_b = 1.0,\ N = 2.5 \times 10^{-2}\ \mathrm{s}^{-1}$

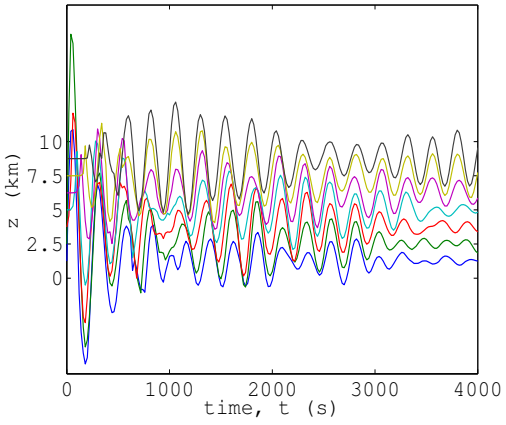

(b) $Ri_b = 1.0, N = 2.5 \times 10^{-2}\ \mathrm{s}^{-1}$

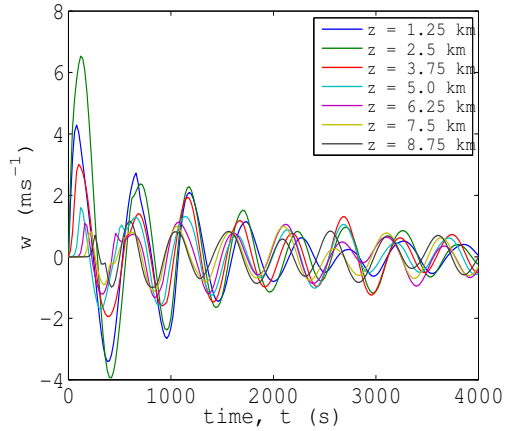

(c) $Ri_b = 0.25,\ N = 1.25 \times 10^{-3}\ \mathrm{s}^{-1}$

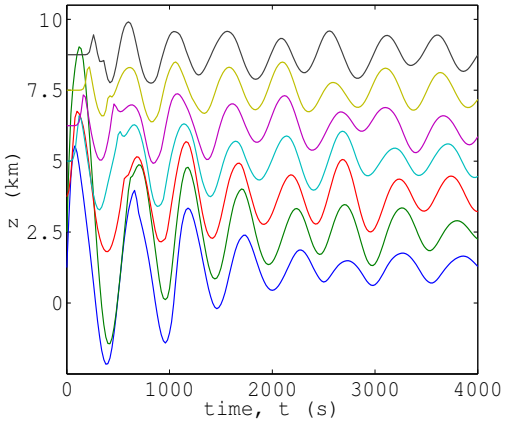

(d) $Ri_b = 0.25,\ N = 1.25 \times 10^{-3}\ \mathrm{s}^{-1}$

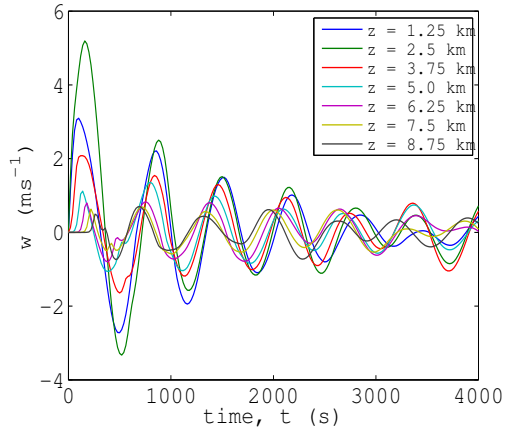

(e) $Ri_b = 0.16,\ N = 1.0 \times 10^{-2}\ \mathrm{s}^{-1}$

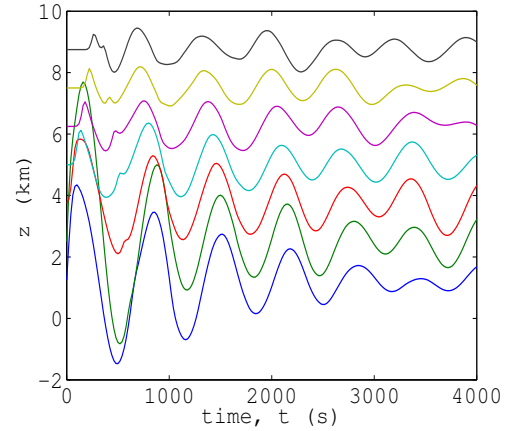

(f) $Ri_b = 0.16,\ N = 1.0 \times 10^{-2}\ \mathrm{s}^{-1}$

Figure 4.11: Evolution of vertical velocity at $x = 0$, $z = 1.25, 2.5, 3.75, 5.0, 6.25, 7.5, 8.75$ km for the stable environment and (a) (c) (e) shows the amplitude of the waves and (b) (d) (f) shows the waves in different vertical positions.

4.3.7 Energy balance

The following energy balance laws of the kinetic and potential energies

$$E_k = \frac{1}{2}\int_\Omega (u^2 + w^2)\mathrm{d}V, \qquad \text{and} \qquad E_p = \int_\Omega (z_{max} - z)\theta \mathrm{d}V$$

satisfy

$$\frac{\mathrm{d}E_k}{\mathrm{d}t} = \int_\Omega w\theta \mathrm{d}V - K_M\epsilon\,, \qquad \epsilon = \int_\Omega |\Delta u|^2 + |\Delta w|^2 \mathrm{d}V$$

and

$$\frac{\mathrm{d}E_p}{\mathrm{d}t} = -\int_\Omega w\theta \mathrm{d}V + K_H \frac{\theta_{\max} - \theta_{\min}}{z_{\max} - z_{\min}},$$

respectively (see, Winters & Young, 2009). These energy equations quantify the rate of production of E_p, the conversion from E_p to E_k, and the rate of kinetic energy dissipation, ϵ, thereby making a steady state energy balance.

An objective of this energy balance experiment is to verify whether the present method demonstrates conservation of energy, which is one important aspect of efficient numerical approaches for atmospheric modelling. The normalized energy plot in Figure 4.12 provides a more quantitative measure on the accuracy of the simulation. The time evolution of E_p, E_k and total energy, $E = E_p + E_k$ have been reported in Figure 4.12. Clearly, the potential energy, E_p, decreases with time as a result of the potential energy conversion into kinetic energy, E_k, as well as the total energy, E remains approximately constant; moreover, this is an advantage of this model that there is so little dissipation in this model. In Figure 4.12, it is also clear that the conversion rate increases when eddy viscosity, K_M, decreases as well as potential energy and kinetic energy are the same for $K_M = 10,\ 5$ and $1\ \mathrm{m^2 s^{-1}}$ at $t = 1007,\ 986$ and 936 s, respectively. The result of the energy conservation in Figure 4.12 has an excellent agreement with the corresponding result reported by Carpenter *et al.* (1990).

The energy curves in the case of a stable environment are shown in Figure 4.13. In this

case, the normalized energy curves are presented. In each curve kinetic energy initially increases and reaches its peak. At the same time, the potential energy decreases, and it is converted to the kinetic energy. The total energy is also shown in Figure 4.13. This initial situation is similar to the neutral environment where the warm bubble moves up without any barrier. In the stable case, however, the warm bubble at first starts to rise, and after a few risings, the upper strong stable layer resists its rising, and it starts to penetrate the upper stable environment. Due to this penetration, internal waves are generated which transfer energy to the free atmosphere. The energy curves presented in Figure 4.13 are correlated with internal waves, which is an indication of energy transfer due to internal waves.

4.4 Summary

In this chapter, penetrative convection has been investigated for the neutrally stratified environment and stably stratified environment. The neutral case shows chaotic mixing at smaller eddy viscosities; however, the main characteristics of the flow do not depend on eddy viscosities. The chaotic mixing of this case is a representative of turbulent mixing. In the stable case, stability kills turbulence and the internal waves appear in the stable atmosphere. Waves die out when the bulk Richardson number Ri_b is larger than the critical value $Ri_b = 0.25$, and when Ri_b is less than the critical value, waves can propagate in the upper layers in the atmosphere. In both cases, energy is conserved and in the stable environment energy is transferred to the upper layer of the atmosphere due to the internal waves.

In the next chapter, the same numerical model is implemented to investigate the penetration of turbulence for a large horizontal area due to the differential heating of the earth's surface.

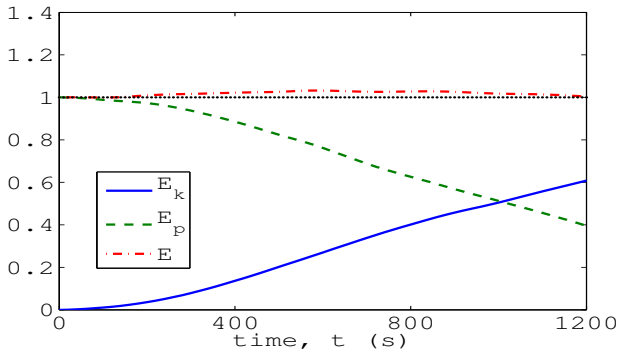

(a)

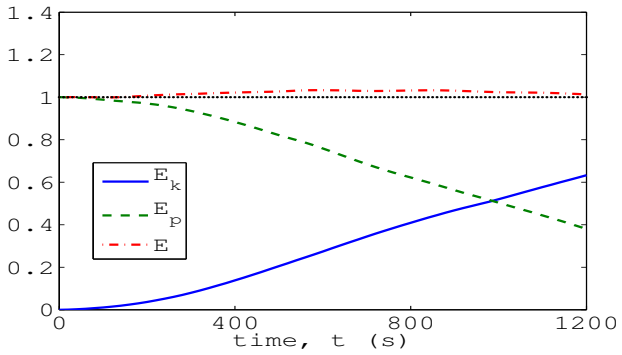

(b)

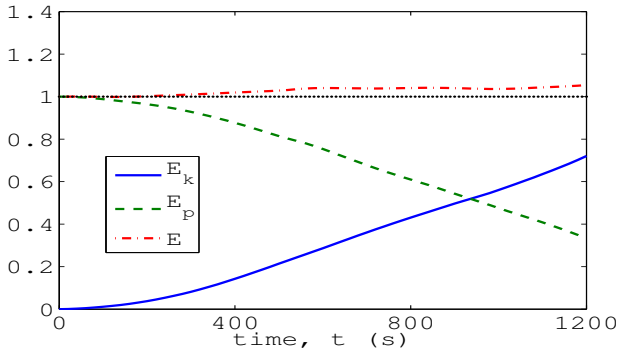

(c)

Figure 4.12: Energy balance, showing that total energy (E) is conserved, where potential energy (E_p) is converted to kinetic energy (E_k) for $\theta_0 = 300$ K, (a) $K_M = 10$ m^{2}s^{-1}, (b) $K_M = 5$ m^{2}s^{-1} and (c) $K_M = 1$ m^{2}s^{-1}. Black dotted line represents $E = 1$.

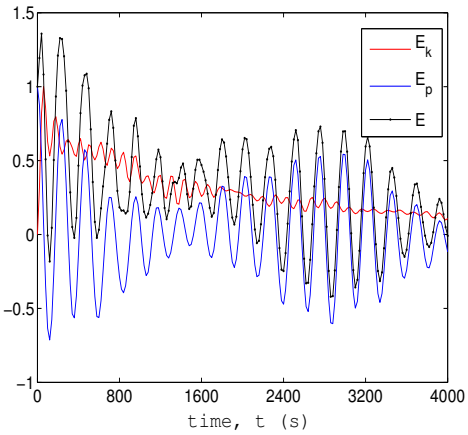

(a) $N = 2.5 \times 10^{-2}$ s^{-1}

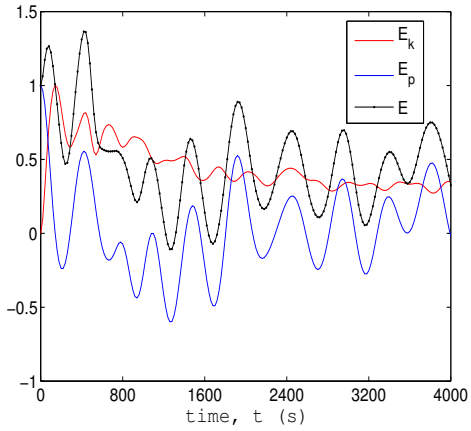

(b) $N = 1.25 \times 10^{-2}$ s^{-1}

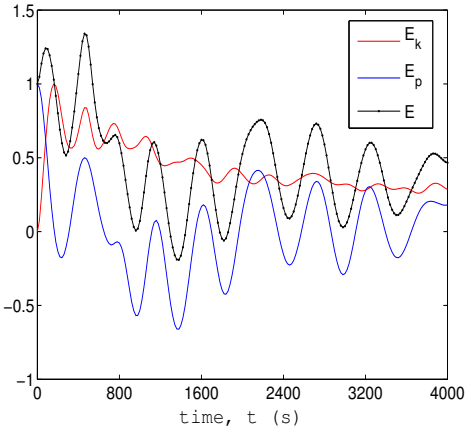

(c) $N = 1.12 \times 10^{-2}$ s^{-1}

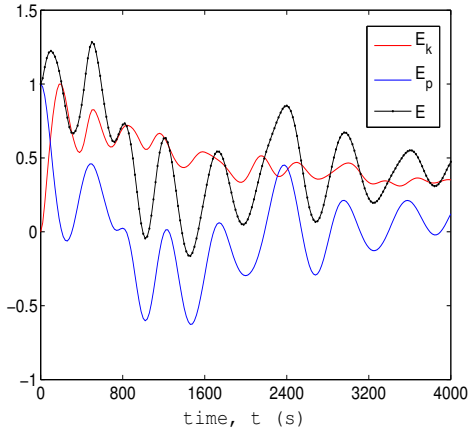

(d) $N = 1.0 \times 10^{-2}$ s^{-1}

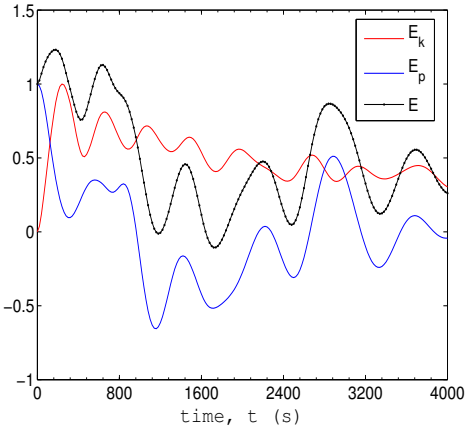

(e) $N = 7.9 \times 10^{-3}$ s^{-1}

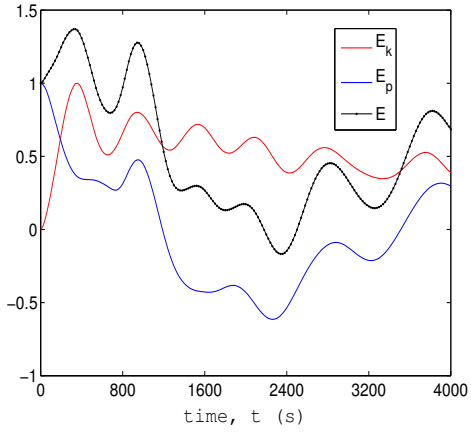

(f) $N = 5.6 \times 10^{-3}$ s^{-1}

Figure 4.13: Energy curves for the stable environment where (a) $N = 2.5 \times 10^{-2}$ s^{-1}, (b) $N = 1.25 \times 10^{-2}$ s^{-1}, (c) $N = 1.12 \times 10^{-2}$ s^{-1}, (d) $N = 1.0 \times 10^{-2}$ s^{-1}, (e) $N = 7.9 \times 10^{-3}$ s^{-1} and (f) $N = 5.6 \times 10^{-3}$ s^{-1}.

Chapter 5

Penetrative turbulence for a differentially heated horizontal area

This chapter presents a form of the penetrative turbulence in a dry atmosphere, where a turbulent convective air covers a large horizontal area due to the differential heating and gradually incorporates a stable layer above it. This phenomenon is usually observed during the daytime when the sun heats the earth's surface. This surface heating leads to a convective motion, which also leads to significant turbulence that mixes the air within the above stable layer for large surface heat flux. Due to this penetration, internal waves are generated above the mixed layer in the atmosphere. To investigate this phenomenon, an urban heat island (UHI) circulation is considered as a model for this form of penetrative turbulence in the atmosphere. The design of this simulation is analogous to the simulation used by Nino & Mori (2005), Dubois & Touzani (2009) and Zhang *et al.* (2014).

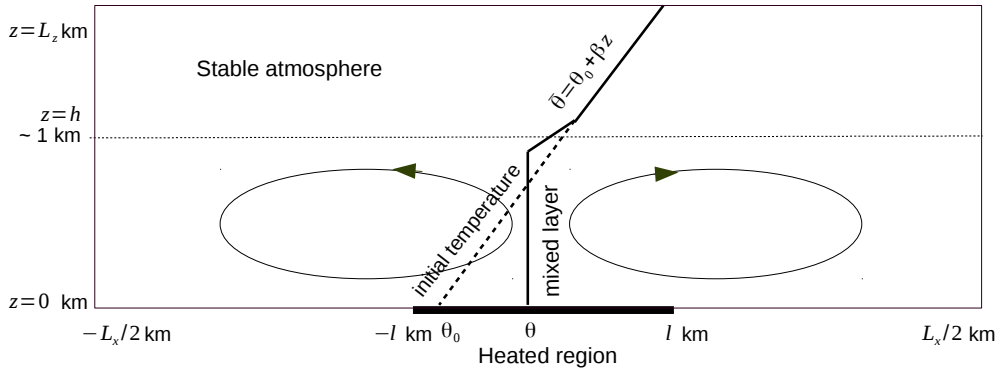

Figure 5.1: Schematic representation of potential temperature profiles in an unstable atmospheric boundary layer. The thick black horizontal line represents the urban heated area.

5.1 Model description

A stably stratified atmosphere is considered in which average potential temperature $\bar{\theta}$ increases linearly with height i.e $\bar{\theta} = \theta_0 + \beta z$, where θ_0 is the potential temperature at the surface and β is a constant vertical gradient of the potential temperature. The heating of the surface owing to the sun in the morning generates a heat flux toward the air. The nocturnal stable boundary layer tends to diminish due to this surface heat flux as well as above airflow. Finally, a mixed layer (h) is produced due to turbulence by means of high intensity heat flux and mixed air flow which is shown in Fig. 5.1.

The domain of the present simulation is considered $[-\frac{L_x}{2},\ \frac{L_x}{2}] \times [0,\ L_z]$ and the domain of the heated region is considered $[-l,\ l]$ which is shown in Figure 5.1. Consider the heat island region $[-l,\ l]$ in which the surface temperature is $\Delta\theta$ higher than the surrounding rural region. Considering the ground surface is flat and the influence of the terrain is ignored, the flow is uniform along the width, and the Coriolis force is negligible. The boundary

conditions at the surface, $z = 0$, are: $u = w = 0$. The potential temperature perturbation θ over the ground area ($z = 0$) is defined by

$$\theta(x,t) = a\left(\tanh\left(\frac{bx+1}{\xi}\right) - \tanh\left(\frac{bx-1}{\xi}\right)\right),$$

where $a = 0.5,\ b = 1$ and $\xi = 0.01$ are constants. At $x = \pm L_x/2$, $\frac{\partial\theta}{\partial x} = 0$ and at $z = L_z$, $\frac{\partial\theta}{\partial z} = 0$.

Two types of boundary conditions are considered for velocity components in other faces of the simulation domain. For Type I, there is no mass flux across the simulation domain ($\mathbf{u}.\hat{\mathbf{n}} = 0$), and the shear stress vanishes in all other faces except the earth's surface i.e. at $x = \pm L_x/2$, $u = 0$ and $\frac{\partial w}{\partial x} = 0$ and at $z = L_z$, $w = 0$ and $\frac{\partial u}{\partial z} = 0$. For Type II, open boundary conditions have been chosen over all other faces at $x = \pm L_x/2$, $\frac{\partial u}{\partial x} = 0$ and $\frac{\partial w}{\partial x} = 0$ and at $z = L_z$, $\frac{\partial w}{\partial z} = 0$ and $\frac{\partial u}{\partial z} = 0$. The boundary conditions of both cases are shown in Figure 5.2 and 5.3. In Dubois & Touzani (2009), a local damping technique is applied at the vertical boundaries; however, the present model can handle the simulation without any artificially imposed layer along the boundaries.

This phenomenon can be modeled by combining only three external parameters: 1) the characteristic diameter of the city: $[-l\ \mathrm{km}, l\ \mathrm{km}]$, 2) the thermal stratification, characterized by its buoyancy frequency: $N = \left(\frac{g\beta}{\theta_0}\right)^{1/2}$ (s^{-1}), and 3) the difference in surface heat flux between the city and the rural areas: H_0 (Wm^{-2}).

The simulation domain is considered as 100 km in the horizontal direction, 2 km in the vertical direction and 10 km or 20 km for the heated region. The heated region is considered 10 km for numerical verification with Dubois & Touzani (2009), and 20 km for all other simulations.

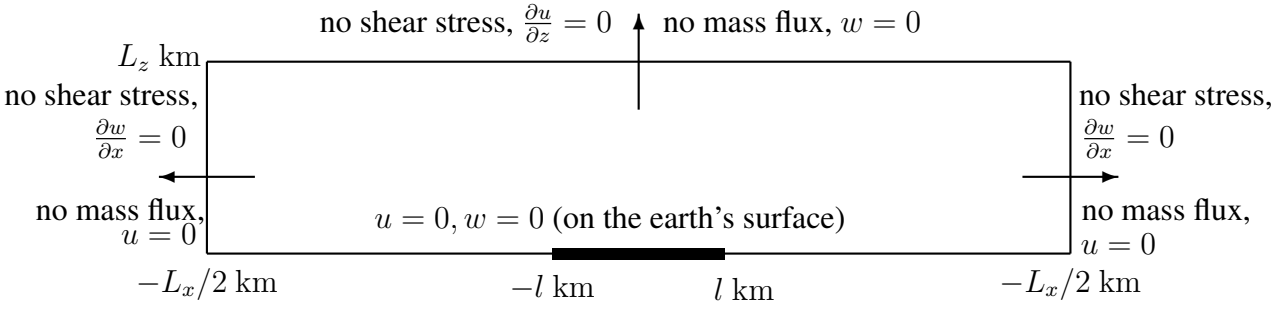

Figure 5.2: Type I boundary conditions.

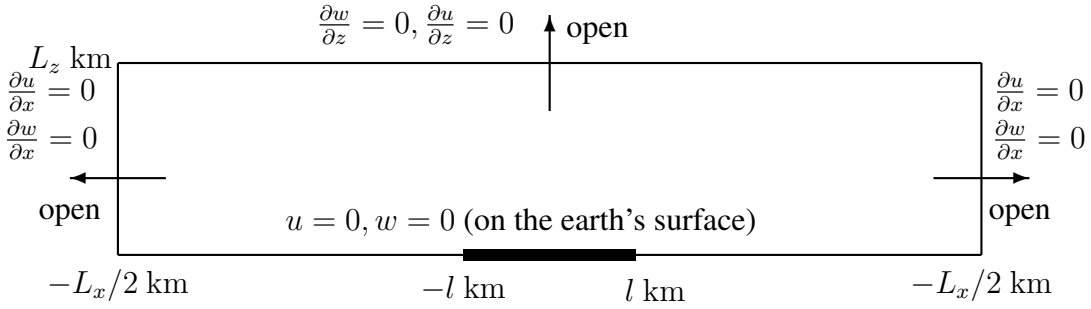

Figure 5.3: Type II boundary conditions.

5.2 Results and Discussion

5.2.1 Dependence of flow characteristics for lower surface heat flux

This section deals with the steady flow of urban heat island circulation for lower surface heat flux, and the comparison with the stationary solutions presented in Dubois & Touzani (2009). They considered no-slip boundary conditions, a large elongated domain and a thermal sponge layer added at the vertical boundaries. In the present model, Type I boundary conditions are used for this comparison which can handle this model without any extra artificial settings near the vertical boundaries. For this comparison, length of the heated region is considered as 10 km at the center of the domain.

The flow regime is highly dependent on surface heat flux. For the surface heat flux $H_0 \leq 115.74\ \mathrm{Wm}^{-2}$ in the heated region, the flow is fully developed within 2 h, and after

that the flow regime becomes steady. To observe the flow regimes, different surface heat fluxes are chosen as a factor of 2 which are analogous with the Rayleigh number as a factor of 10. The steady flow for $H_0 = 28.93, 57.87$ and $115.74\ \mathrm{Wm}^{-2}$ is compared with the stationary solutions of Dubois & Touzani (2009) for Rayleigh number $Ra \leq 10^5$.

From Figure 5.4 to 5.6, the profiles of horizontal velocity, vertical velocity and temperature variation are presented which agree with Dubois & Touzani (2009) (D & T), and these comparison results are presented in nondimensional form. For each figure, a solid line, dashed line and dashed-dotted line represent the profiles for $H_0 = 28.93, 57.87$ and $115.74\ \mathrm{Wm}^{-2}$, respectively. The temperature perturbation, vertical velocity and horizontal velocity decay rapidly with respect to the elevation z, as shown in Figures 5.4a, 5.5a and 5.6a, respectively. The vertical propagation of perturbations is controlled by the vertical stratification. In the horizontal direction, the vertical velocity vanishes rapidly outside the heated region, which is observed in Figure 5.5b. The temperature perturbation and horizontal velocity have similar behaviour along the horizontal direction and are shown in Figures 5.4b and 5.6b. In Figure 5.4a and 5.5a, it is clear that the mixed layer height appears between $z = 1.2$ to 1.5 km, and this height is reduced when surface heat flux becomes larger.

For the purpose of comparison, the nondimensionalized extreme values of the stationary solutions such as horizontal velocity u, vertical velocity w, the temperature variation θ, the vorticity $\omega = \partial w/\partial x - \partial u/\partial z$ and the Nusselt number Nu of both Dubois & Touzani (2009) method (D & T method) and the present method are shown in Table 5.1. The magnitude of the extreme values of u, w, ω and Nu are increased as a function of surface heat flux. The Nusselt number is defined by

$$Nu = -\frac{1}{L_x}\int_{-L_x/2}^{L_x/2} \frac{\partial \theta}{\partial z}(x, z = 0)\, dx$$

The value of this number measures the intensity of heat transfer and it increases with the

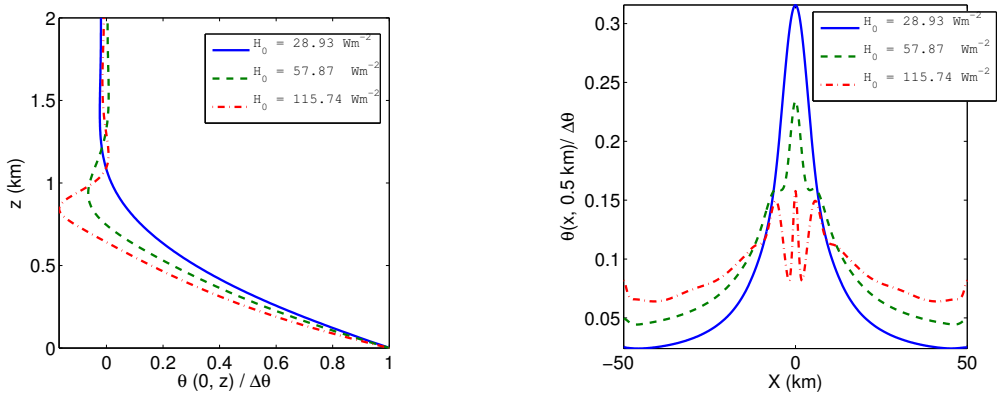

(a) (b)

Figure 5.4: Profiles of the temperature variation θ at (a) $x = 0$ km, (b) $z = 0.5$ km for stationary solution.

surface heat flux.

In §4.3.4, convective velocity (w) was not influenced by eddy viscosity as well as the Rayleigh number because there was no differential heating in the surface so that the surface heat flux was constant all over the surface. However, in Table 5.1 the intensity of the vertical velocity increases significantly as a linear relationship, and it is clear that the surface heat flux is a limiting factor to accelerate convective velocity (w).

For better illustration, contour plots of horizontal velocity, vertical velocity, temperature perturbation and vorticity are shown in Figure 5.7 and 5.8 for $H_0 = 28.93, 57.87$ and 115.74 Wm^{-2}. Contour plots of temperature perturbation and vorticity have a good agreement with Dubois & Touzani (2009). Finally, the agreement between the present simulations and the simulations presented by Dubois & Touzani (2009) is excellent.

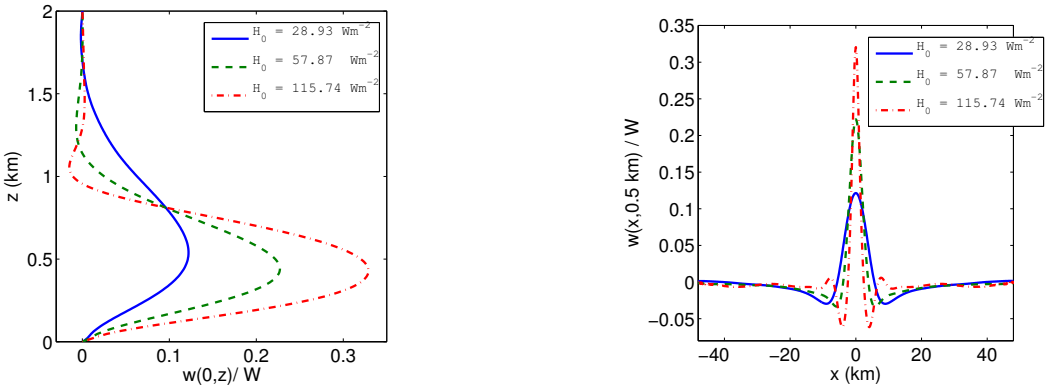

(a) (b)

Figure 5.5: Profiles of the vertical velocity at (a) $x = 0$km (b) $z = 0.5$ km for stationary solution.

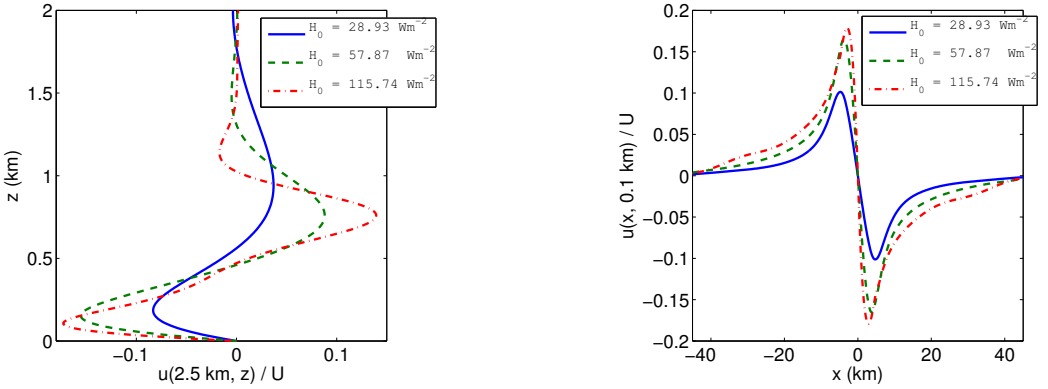

(a) (b)

Figure 5.6: Profiles of the horizontal velocity at (a) $x = 2.5$ km, (b) $z = 0.1$ km for stationary solution.

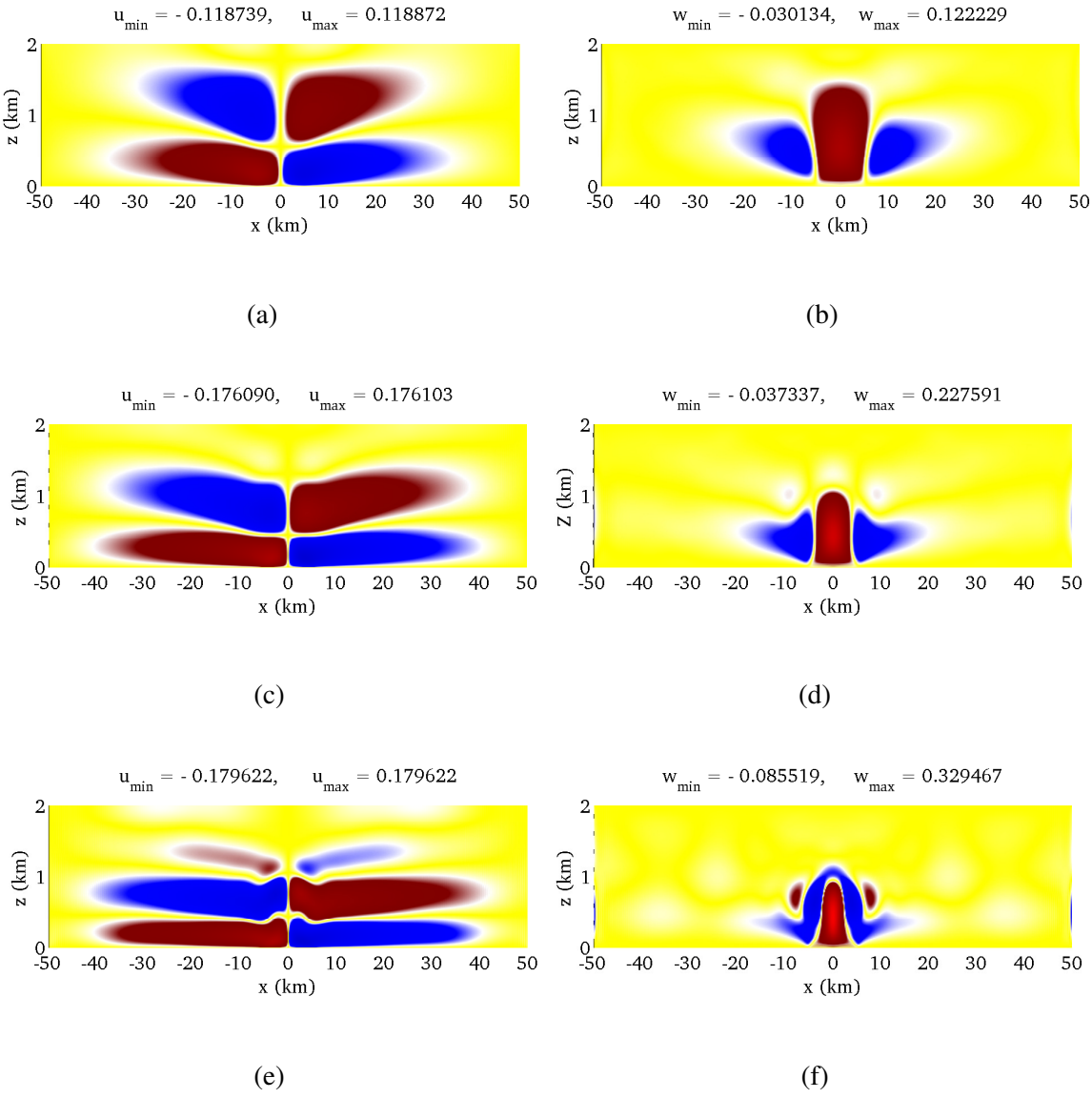

Figure 5.7: Contour plots of Horizontal velocity (left) and vertical velocity (right) for (a), (b) $H_0 = 28.93\ \mathrm{Wm}^{-2}$, (c), (d) $H_0 = 57.87\ \mathrm{Wm}^{-2}$ and (e), (f) $H_0 = 115.74\ \mathrm{Wm}^{-2}$ for stationary solution.

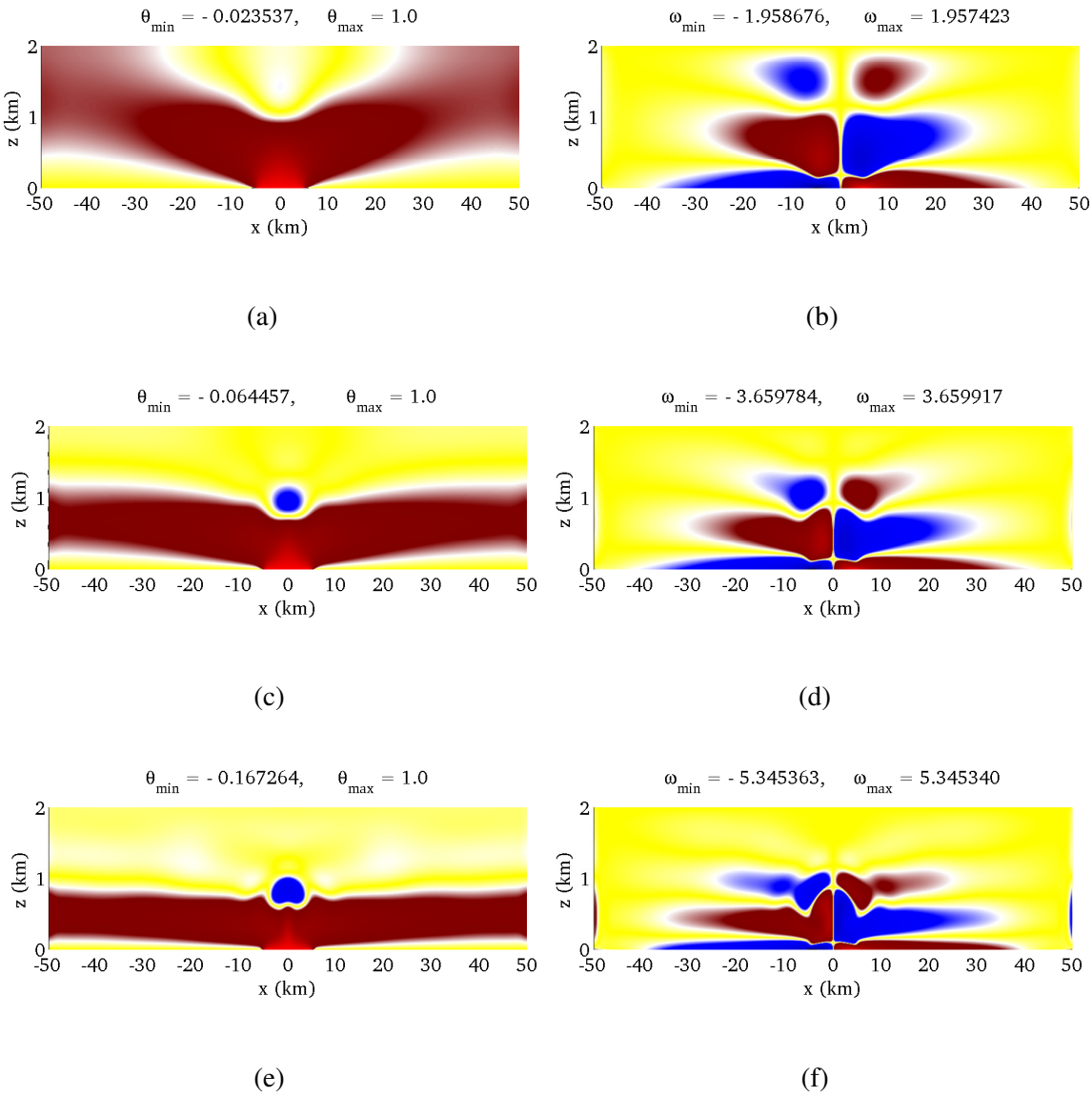

Figure 5.8: Contour plots of potential temperature perturbation (left) and vorticity (right) for (a) $H_0 = 28.93\ \mathrm{Wm}^{-2}$, (b) $H_0 = 57.87\ \mathrm{Wm}^{-2}$ and (c) $H_0 = 115.74\ \mathrm{Wm}^{-2}$ for stationary solution.

H_0	28.93 Wm^{-2}		57.87 Wm^{-2}		115.74 Wm^{-2}	
	Present	D & T	Present	D & T	Present	D & T
$\theta_{\min}$	-0.023537	-0.024823	-0.064457	-0.071289	-0.167264	-0.166316
$\theta_{\max}$	1.0	1.0	1.0	1.0	1.0	1.0
$u_{\min}$	-0.118739	-	-0.176090	-	-0.179622	-
$u_{\max}$	0.118872	0.118887	0.176103	0.174844	0.179622	0.179054
$w_{\min}$	-0.030134	-0.030470	-0.037337	-0.039291	-0.085519	-0.079265
$w_{\max}$	0.122229	0.125594	0.227591	0.228250	0.329467	0.322483
$\omega_{\min}$	-1.958676	-	-3.659784	-	-5.345363	-
$\omega_{\max}$	1.957423	2.06900	3.659917	3.951325	5.345340	5.921375
Nu	0.147744	0.148605	0.326211	0.295132	0.689294	0.643594

Table 5.1: Comparison of extreme values with Dubois & Touzani (2009) (D & T) method.

5.2.2 Experimental investigation for penetrative convection

This section is designed in such a way that the flow regime of the present numerical simulations agrees with the experimental results presented by Kimura (1975) that found the nice circulation patterns of the urban heat island in the laboratory and numerical experiments. Kimura (1975) observed from experiments that heat island circulation has two types of flow regimes. When the differential heating is weak, the centre of the circulation is located at the edges of the heat island and the up-draft prevails all over the heat island; this type of circulation is called type E (Fig. 5.9a). On the other hand, when the differential heating is strong, a strong narrow up-draft is concentrated above the centre of the island, which is called type C (Fig. 5.9c).

In this present numerical experiment, the heat island region is $[-10\ \mathrm{km},\ 10\mathrm{km}]$, and the flow regime as well as location of the centre of the circulation depends on the initial

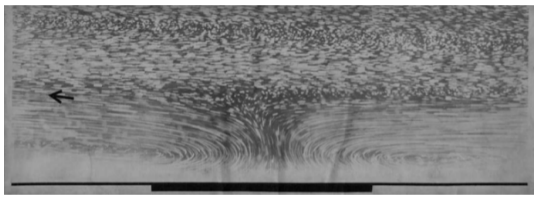

(a) Type E flow regime

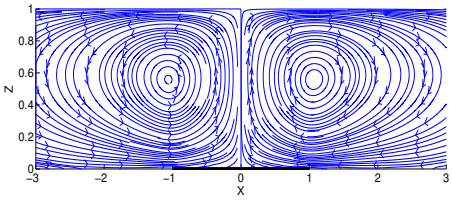

(b) $H_0 = 28.93\ \mathrm{Wm}^{-2}$, $\beta = 1\ \mathrm{K/km}$

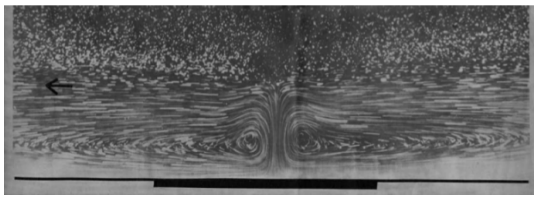

(c) Type C flow regime

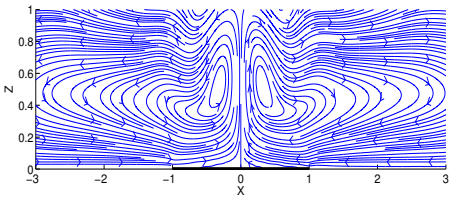

(d) $H_0 = 115.74\ \mathrm{Wm}^{-2}$, $\beta = 10\ \mathrm{K/km}$

Figure 5.9: (Left) Two types of flow regimes found in a laboratory experiment on the UHI circulation (Kimura, 1975). (a) Type E is obtained for low differential heating, (c) Type C is obtained for strong differential heating. (Right) Numerically experimented results (b) $H_0 = 28.93\ \mathrm{Wm}^{-2}$, $\beta = 1\ \mathrm{K/km}$ (d) $H_0 = 115.74\ \mathrm{Wm}^{-2}$, $\beta = 10\ \mathrm{K/km}$. The thick black horizontal line represents the heat island.

surface heat flux. When the surface heat flux increases, the center of the circulation moves toward the center of the island. For heat flux, $28.93\ \mathrm{Wm}^{-2} \leq H_0 \leq 115.74\ \mathrm{Wm}^{-2}$ the solution is stationary. The simulations of stationary solutions are described in §5.2.1. For a fixed initial heat flux, the heat intensity of the heat island depends on a constant vertical potential temperature gradient. Similar numerical results are shown in Figure 5.9b and 5.9d. In Fig. 5.9b, initial surface heat flux $28.93\ \mathrm{Wm}^{-2}$, a constant vertical potential temperature gradient $\beta = 1\ \mathrm{K/km}$ and in Fig. 5.9d, initial surface heat flux $115.74\ \mathrm{Wm}^{-2}$, $\beta = 10\ \mathrm{K/km}$, so the center of the circulation of Fig.5.9d is close to the center of the island, and a strong updraft is observed. However, in Fig. 5.9b the center of the circulation is far away from the center of the island and the up-draft prevails due to weak heating.

Finally, there is an excellent agreement between the present simulations and the experimental results presented by Kimura (1975).

5.2.3 Dependence of flow patterns of boundary conditions

In this section, the flow patterns are observed for two types of boundary conditions which are described in §5.1. To analyze the results of both types of boundary conditions, surface heat flux $H_0 = 115.74\ \mathrm{Wm}^{-2}$ with a constant vertical gradient of potential temperature $\beta = 10\ \mathrm{K/km}$ is considered, and the presented results are taken at time $t = 6.5\ \mathrm{h}$ when the flow is fully generated.

The horizontal velocity profile for both types of boundary conditions is similar to the heated region and the surrounding region. However, near the vertical boundaries horizontal velocity becomes zero for Type I boundary condition. Moreover, in the case of the Type II boundary condition, inward and outward flow exist in the boundary though it is far away from the heated region since Type II is open boundary. The horizontal velocity profiles for Type I and Type II boundary conditions are shown in Figure 5.10a and Figure 5.10b,

respectively. The maximum inward horizontal velocities for Type I and Type II are 5.52 ms^{-1} and 5.86 ms^{-1}, respectively. Since for the Type II boundary condition, the flow can cross the vertical boundaries, so in Type II the magnitude of the horizontal velocity is slightly larger than in Type I.

Vertical velocity is almost identical in both types of boundary conditions and the vertical velocity is concentrated in the heated region. The maximum downward velocities for Type I and Type II are 0.26 ms^{-1} and 0.27 ms^{-1}, and the maximum upward velocities are 0.84 ms^{-1} and 0.96 ms^{-1}, respectively. In order to observe the flow pattern more clearly, the stream lines of both types are shown in Figure 5.10g and 5.10h. Since Type II is open boundary conditions, air parcel can move in or move out through the boundaries except the earth's surface; however, for Type I flow is restricted by the boundaries. Due to these two types of flow pattern, temperature perturbation profiles are different near the vertical boundaries, which are shown in Figure 5.10e and 5.10f.

5.2.4 Dependence of flow patterns on surface heat flux (H_0)

In order to study how a heat island circulation is affected by varying surface heat flux, simulations have been conducted for $28.93\ \mathrm{Wm}^{-2} \leq H_0 \leq 925.92\ \mathrm{Wm}^{-2}$. For $H_0 = 28.93, 57.87$ and $115.74\ \mathrm{Wm}^{-2}$ flow patterns are discussed in §5.2.1 along with the comparison of Dubois & Touzani (2009). Figure 5.7 and 5.8 shows the horizontal velocity, vertical velocity, potential temperature perturbation and vorticity field for smaller surface heat flux. Flow characteristics for larger surface heat flux are analyzed in this section.

Figures 5.11, 5.12 and 5.13 show horizontal velocity, vertical velocity and the potential temperature perturbation, respectively, for larger surface heat flux, $H_0 = 231.48, 462.96$ and $925.92\ \mathrm{Wm}^{-2}$ at $t = 6.5$ h and $\beta = 10\ \mathrm{K/km}$. For $H_0 \leq 115.74\ \mathrm{Wm}^{-2}$, the flow pattern is steady and symmetric about the center of the heat island. For larger surface heat

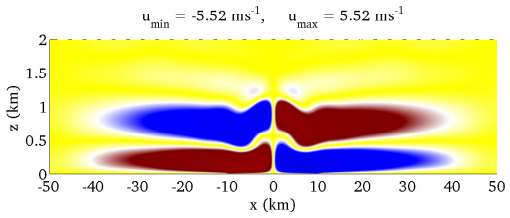

(a) Horizontal velocity

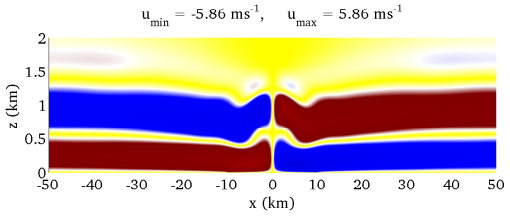

(b) Horizontal velocity

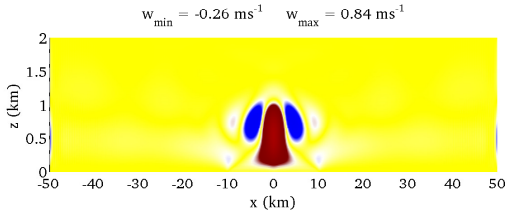

(c) Vertical velocity

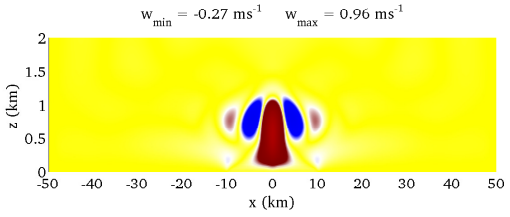

(d) Vertical velocity

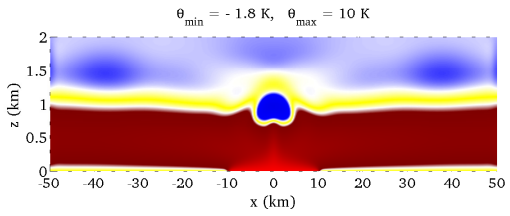

(e) Potential temperature

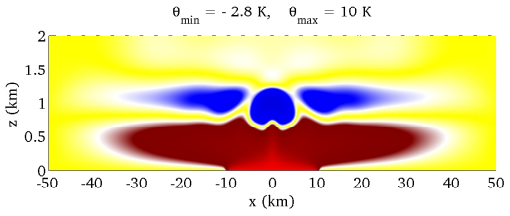

(f) Potential temperature

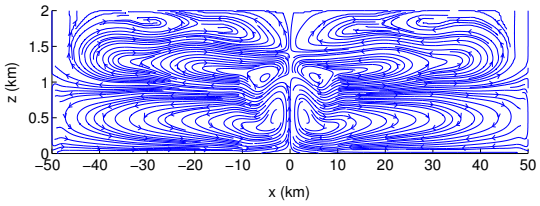

(g) Stream lines

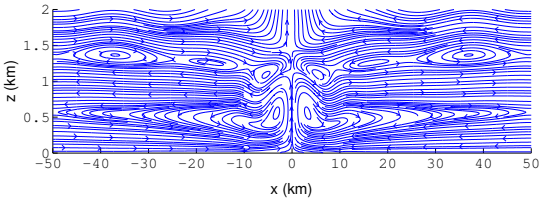

(h) Stream lines

Figure 5.10: (a), (c), (e) and (g) for Type I and (b), (d), (f) and (h) for Type II boundary conditions which are described in §5.1 at $t = 6.5$ h .

flux ($H_0 \geq 231.48\ \mathrm{Wm}^{-2}$) the flow pattern is not steady and symmetric. Urban heat island circulation is a horizontally dominated circulation. Horizontal velocity is symmetric along the center of the heat island for $28.93 \leq H_0 \leq 231.48\ \mathrm{Wm}^{-2}$. For $H_0 \geq 462.96\ \mathrm{Wm}^{-2}$ the symmetry of the horizontal velocity is broken and turbulent flow is visible in heat island and its vicinity. For $28.93 \leq H_0 \leq 231.48\ \mathrm{Wm}^{-2}$, vertical velocity is concentrated only on the heat island region (Fig. 5.7(right) and 5.12a). On the other hand, for larger surface heat flux, $H_0 \geq 231.48\ \mathrm{Wm}^{-2}$ vertical velocity appears throughout the urban and rural region (Fig. 5.12b and 5.12c). The thermal plume cannot develop in a stratified medium. In Figure 5.8(left) and 5.13, the length of the developed thermal plume decreases as surface heat flux increases and a thermal sink characterized by the negative temperature perturbation is observed for the effect of vertical stratification.

The large UHI heat intensity causes stronger convergence and divergence wind over the urban area and both the horizontal and vertical wind speeds with the UHI intensity. The outward wind speed is much higher than the inward wind speed in the convective boundary layer and the vertically upward wind speed is higher than the downward wind speed. The maximum outward wind speeds for $H_0 = 231.48$, 462.96 and 925.92 W m^{-2} are 5.19, 6.78 and 8.21 m s^{-1}, respectively, whereas the maximum inward wind speeds are 3.37, 4.43 and 5.36 m s^{-1}, respectively. Similarly, the maximum upward wind speeds for $H_0 = 231.48$, 462.96 and 925.92 W m^{-2} are 1.08, 1.16 and 1.31 m s^{-1}, respectively, whereas the maximum downward wind speeds are 0.49, 0.73 and 0.85 m s^{-1}, respectively.

The required minimum grid size corresponding surface heat flux of these simulations are shown in Table 5.2. From this Table it is observed that a large grid size is required for the simulation of a large surface heat flux.

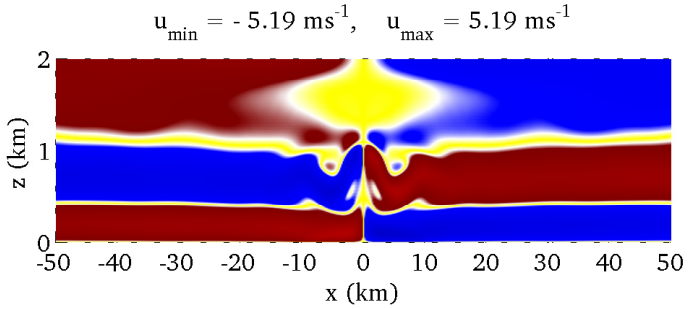

(a) $H_0 = 231.48\ \mathrm{Wm}^{-2}$

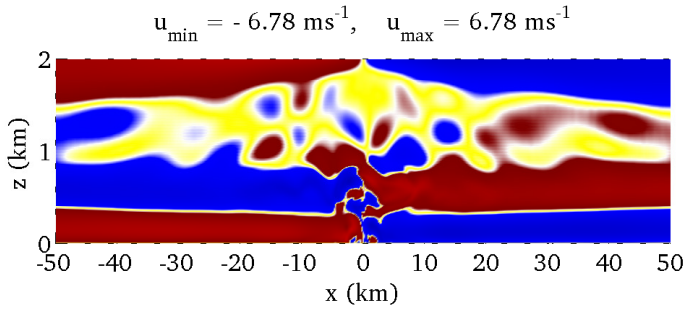

(b) $H_0 = 462.96\ \mathrm{Wm}^{-2}$

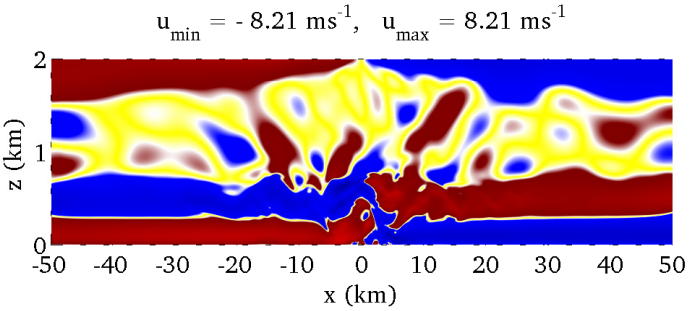

(c) $H_0 = 925.92\ \mathrm{Wm}^{-2}$

Figure 5.11: Horizontal velocity for (a) $H_0 = 231.48\ \mathrm{Wm}^{-2}$, (b) $H_0 = 462.96\ \mathrm{Wm}^{-2}$ and (c) $H_0 = 925.92\ \mathrm{Wm}^{-2}$ at $t = 6.5\ \mathrm{h},\ \beta = 10\ \mathrm{K/km}$ using Type II boundary conditions.

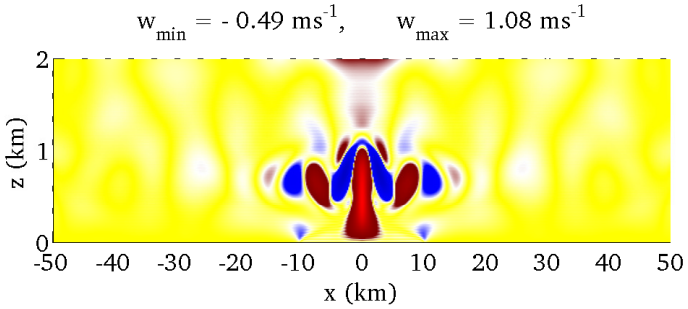

(a) $H_0 = 231.48\ \mathrm{Wm}^{-2}$

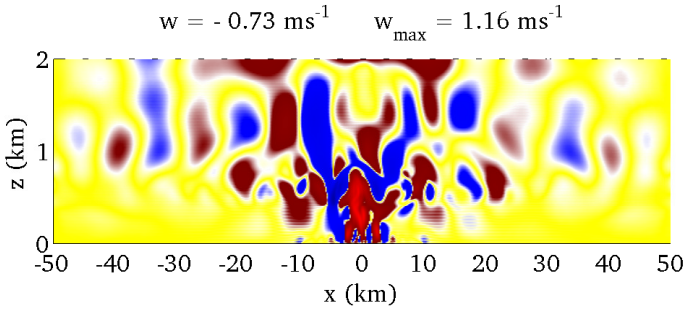

(b) $H_0 = 462.96\ \mathrm{Wm}^{-2}$

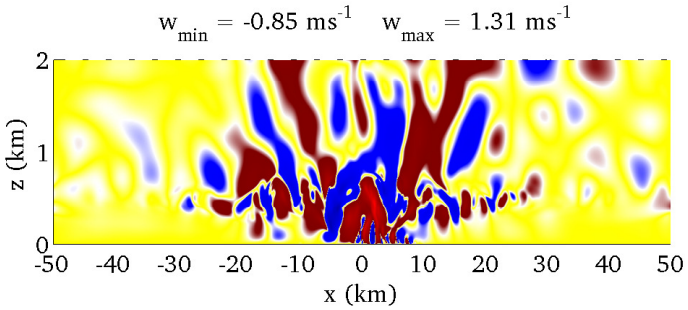

(c) $H_0 = 925.92\ \mathrm{Wm}^{-2}$

Figure 5.12: Vertical velocity for (a) $H_0 = 231.48\ \mathrm{Wm}^{-2}$, (b) $H_0 = 462.96\ \mathrm{Wm}^{-2}$ and (c) $H_0 = 925.92\ \mathrm{Wm}^{-2}$ at $t = 6.5\ \mathrm{h},\ \beta = 10\ \mathrm{K/km}$ using Type II boundary conditions.

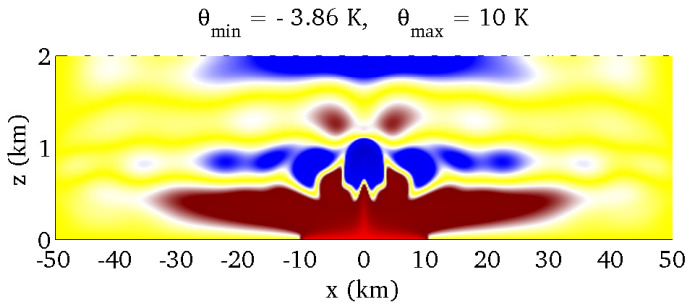

(a) $H_0 = 231.48\ \mathrm{Wm}^{-2}$

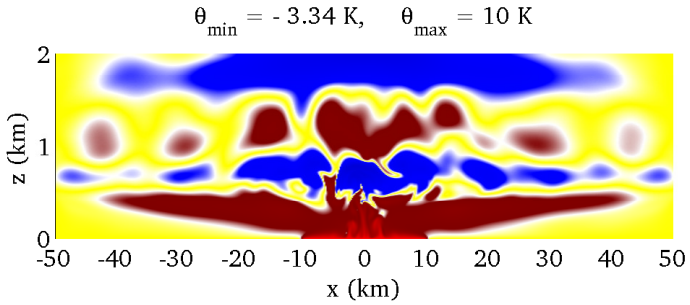

(b) $H_0 = 462.96\ \mathrm{Wm}^{-2}$

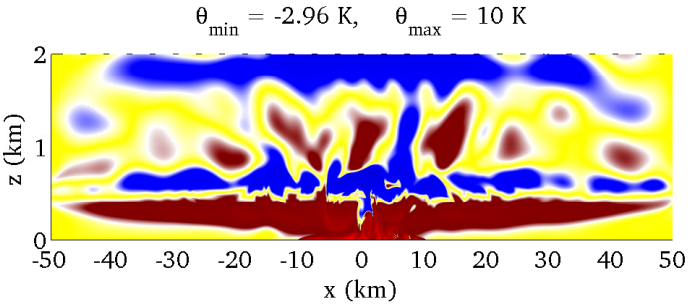

(c) $H_0 = 925.92\ \mathrm{Wm}^{-2}$

Figure 5.13: Temperature perturbation for (a) $H_0 = 231.48\ \mathrm{Wm}^{-2}$, (b) $H_0 = 462.96\ \mathrm{Wm}^{-2}$ and (c) $H_0 = 925.92\ \mathrm{Wm}^{-2}$ at $t = 6.5$ h, $\beta = 10\ \mathrm{K/km}$ using Type II boundary conditions.

H_0 (Wm^{-2})	Minimum grid size
28.93	65×33
57.87	65×65
115.74	129×65
231.48	257×129
462.96	513×257
925.92	1025×513

Table 5.2: Minimum grid size corresponding to the surface heat flux for $\beta = 10\ \mathrm{K/km}$.

5.2.5 Coherent turbulent structure

In this section, vorticity is depicted to analyze the coherent structure of turbulent flow. Figure 5.14 shows how coherent vorticities decrease in size and increase in number while surface heat flux increases. This changes shows that the flow is laminar for $28.93\ \mathrm{Wm}^{-2} \leq H_0 \leq 115.74\ \mathrm{Wm}^{-2}$, laminar-turbulent transition for $231.48\ \mathrm{Wm}^{-2} \leq H_0 \leq 462.96\ \mathrm{Wm}^{-2}$, and fully turbulent for $H_0 = 925.92\ \mathrm{Wm}^{-2}$. In Figure 5.15, the vorticity field shows eddy turnover time at (a) $t = 0.5$ h, (b) $t = 1$ h, (c) $t = 1.5$ h, (d) $t = 2$ h, (e) $t = 2.5$ h and (f) $t = 3$ h where $H_0 = 925.92\ \mathrm{Wm}^{-2}$, $\beta = 10\ \mathrm{K/km}$. Figures 5.15a and 5.15b shows the initial turbulent eddies are created in the urban-rural interface, and they turn-over in this interface. After a time eddies are created in the whole urban area (Fig. 5.15c - 5.15d) and the turbulent mixing spreaded near the rural areas (Fig. 5.15e - 5.15f). The turbulent mixing also depends on the thermal stratification which is characterized by a constant vertical temperature gradient β. The vorticity for $\beta = 10,\ 2$ and $1\ \mathrm{K/km}$ at $t = 6.5$ h, $H_0 = 925.92\ \mathrm{Wm}^{-2}$ are shown in Figure 5.16. These figures show the coherent vorticities decrease in size and increase in number while β increases.

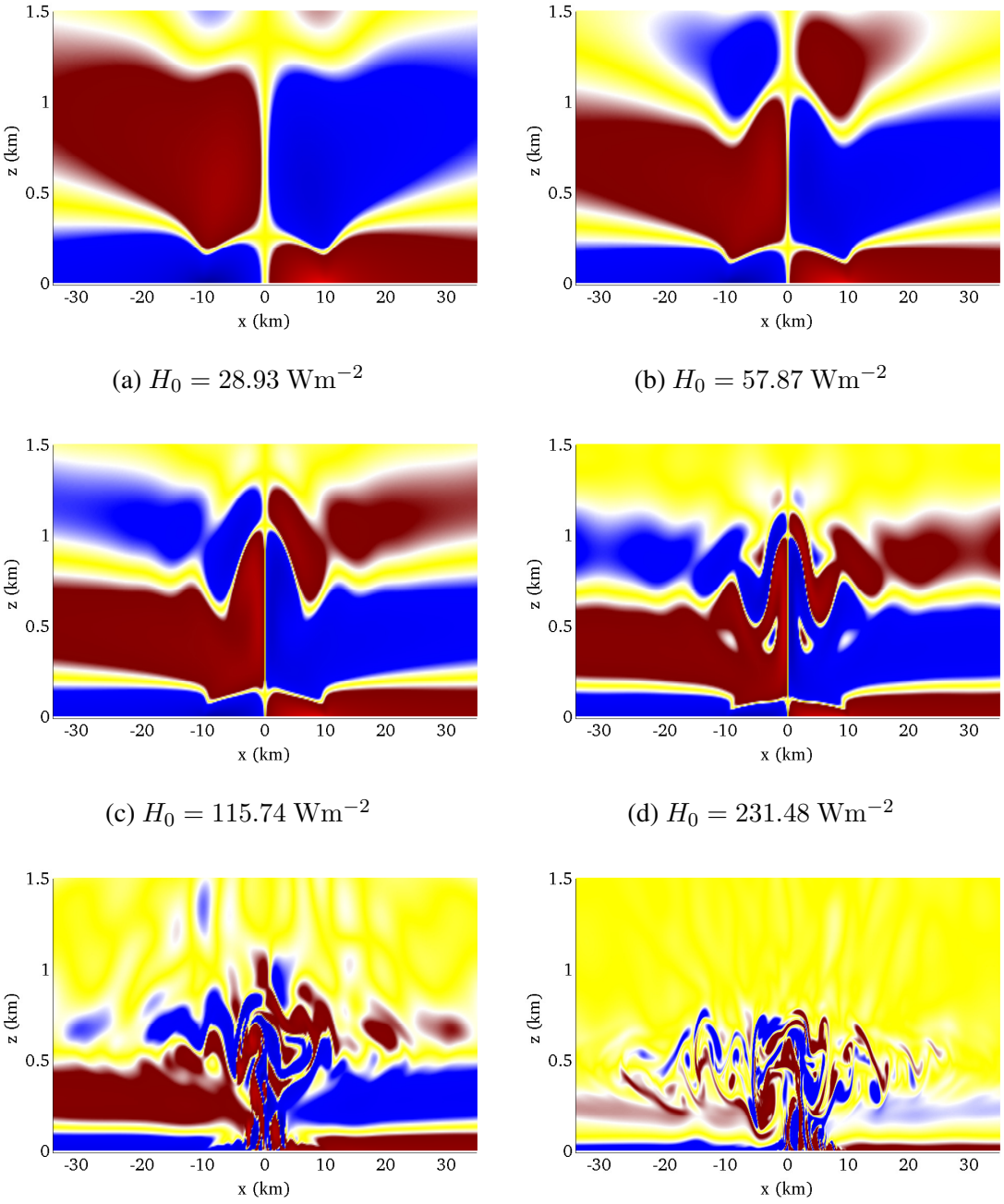

(a) $H_0 = 28.93\ \mathrm{Wm}^{-2}$

(b) $H_0 = 57.87\ \mathrm{Wm}^{-2}$

(c) $H_0 = 115.74\ \mathrm{Wm}^{-2}$

(d) $H_0 = 231.48\ \mathrm{Wm}^{-2}$

(e) $H_0 = 462.96\ \mathrm{Wm}^{-2}$

(f) $H_0 = 925.92\ \mathrm{Wm}^{-2}$

Figure 5.14: The vorticity field at $t = 6.5$ h for $\beta = 10\ \mathrm{K/km}$ and (a) $H_0 = 28.93\ \mathrm{Wm}^{-2}$, (b) $H_0 = 57.87\ \mathrm{Wm}^{-2}$, (c) $H_0 = 115.74\ \mathrm{Wm}^{-2}$, (d) $H_0 = 231.48\ \mathrm{Wm}^{-2}$, (e) $H_0 = 462.96\ \mathrm{Wm}^{-2}$, (f) $H_0 = 925.92\ \mathrm{Wm}^{-2}$.

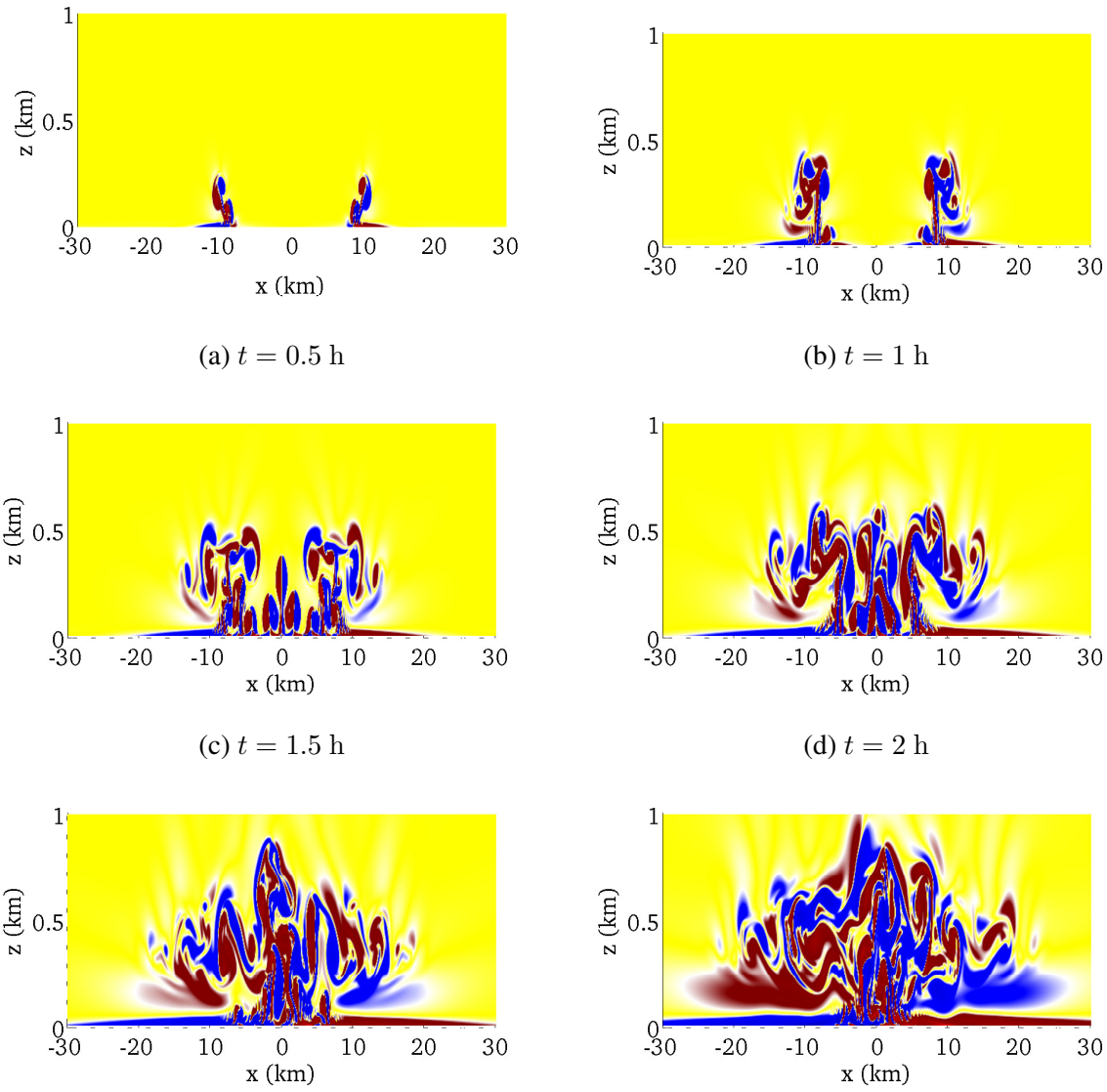

(a) $t = 0.5$ h

(b) $t = 1$ h

(c) $t = 1.5$ h

(d) $t = 2$ h

(e) $t = 2.5$ h

(f) $t = 3$ h

Figure 5.15: The vorticity field for $H_0 = 925.92$ Wm^{-2}, $\beta = 10$ K/km at (a) $t = 0.5$ h, (b) $t = 1$ h, (c) $t = 1.5$ h, (d) $t = 2$ h, (e) $t = 2.5$ h and (f) $t = 3$ h.

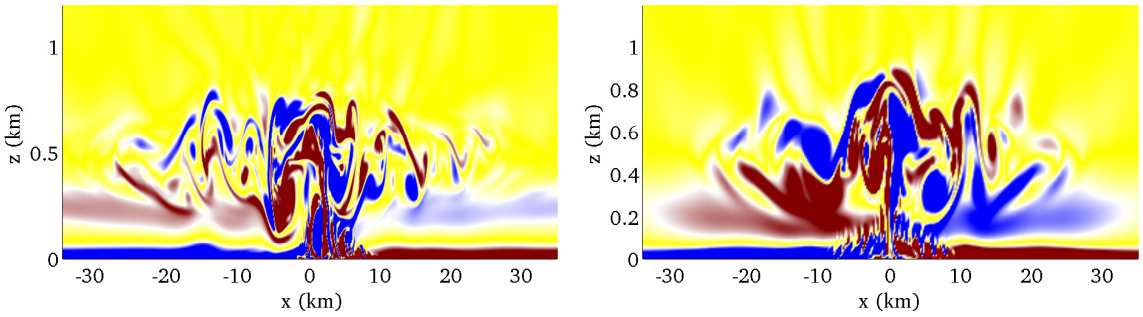

(a) $\beta = 10$ K/km

(b) $\beta = 2$ K/km

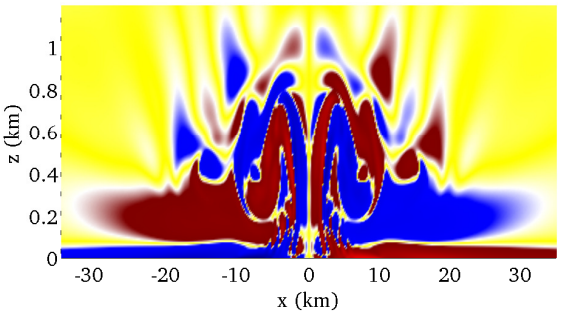

(c) $\beta = 1$ K/km

Figure 5.16: The vorticity for (a) $\beta = 10$ K/km, (b) $\beta = 2$ K/km and (c) $\beta = 1$ K/km at $t = 6.5$ h, $H_0 = 925.92$ Wm^{-2}.

5.2.6 Profiles of potential temperature

Vertical profiles of potential temperature are an important characteristic to understand the mixed layer height of the atmospheric boundary layer (ABL). Due to the turbulent mixing, perturbed potential temperature fluctuates in the ABL. At first, the fluctuations of the potential temperature are observed using a time series. In Figure 5.17, the temperature time series from the center of the heat island at four different heights, $z = 0.0625,\ 0.125,\ 0.25$ and 0.5 km are presented. For comparison, the results of two different initial heat flux, $H_0 = 462.96\ \mathrm{Wm}^{-2}$ [Fig. 5.17 (left)] and $H_0 = 925.92\ \mathrm{Wm}^{-2}$ [Fig. 5.17 (right)] are shown. For each position, the temperature perturbation of $H_0 = 925.92\ \mathrm{Wm}^{-2}$ is more fluctuated than $H_0 = 462.96\ \mathrm{Wm}^{-2}$. Fluctuations also depend on the height. Fluctuations of the lower height are larger than the upper height.

The profile of the mean temperature perturbation $\Theta(z)$ are calculated from the time series $\theta_i(z)$ by

$$\Theta(z) = \frac{1}{N}\sum_{i=1}^{N}\theta_i(z).$$

The temperature can be further characterized by calculating the profile $\sigma(z)$ of the standard deviation. The dimension of these quantities is kelvin and are defined as

$$\sigma(z) = \left(\frac{1}{N}\sum_{i=1}^{N}\left(\theta_i(z) - \Theta(z)\right)^2\right)^{1/2}.$$

For $H_0 = 462.96\ \mathrm{Wm}^{-2}$ and $H_0 = 925.92\ \mathrm{Wm}^{-2}$, the standard deviations of the heights $z = 0.0625,\ 0.125,\ 0.25$ and 0.5 km are $1.645, 1.295, 0.923$ and 0.811 K, and $1.595, 1.485,$ 1.050 and 0.633 K, respectively. The total potential temperature for both $H_0 = 462.96$ Wm^{-2} and $H_0 = 925.92\ \mathrm{Wm}^{-2}$ are shown in Figure 5.18. The mixed layer height for $H_0 = 462.96\ \mathrm{Wm}^{-2}$ and $H_0 = 925.92\ \mathrm{Wm}^{-2}$ are about 0.8 km and 0.7 km, respectively, and the inversion layer appears about $0.8 - 1.0$ km and $0.7 - 0.8$ km, respectively. The mixed layer height decreases as surface heat flux increases.

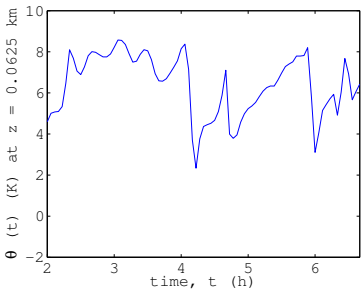

(a) $z = 0.0625$ km

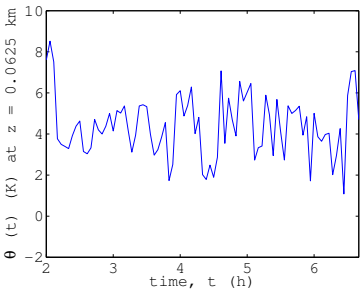

(b) $z = 0.0625$ km

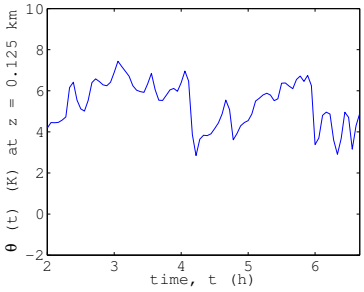

(c) $z = 0.125$ km

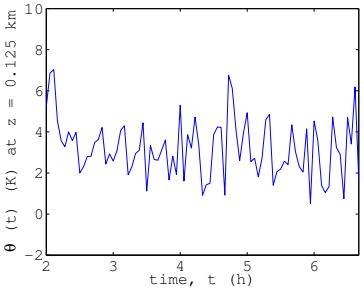

(d) $z = 0.125$ km

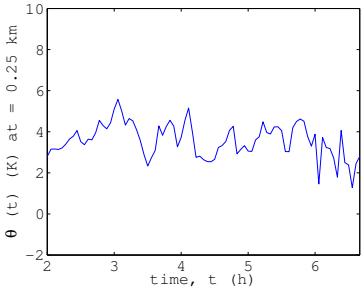

(e) $z = 0.25$ km

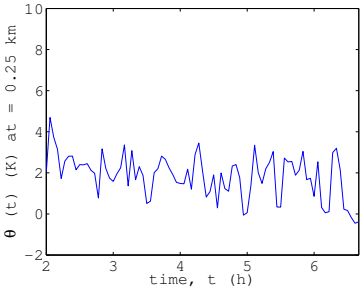

(f) $z = 0.25$ km

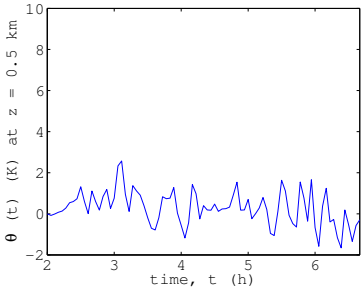

(g) $z = 0.5$ km

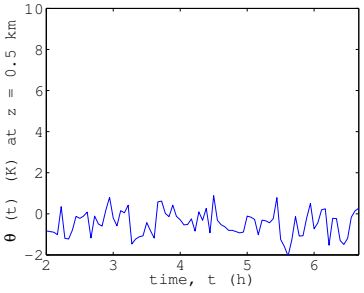

(h) $z = 0.5$ km

Figure 5.17: Temperature time series from the center of the heat island at four different heights (z) for $H_0 = 462.96$ Wm^{-2} (left) and $H_0 = 925.92$ Wm^{-2} (right).

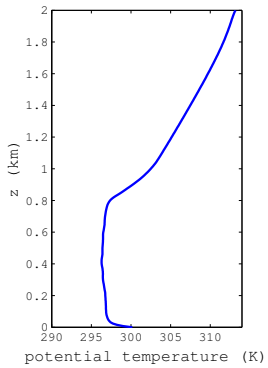

(a) $H_0 = 462.96\ \mathrm{Wm}^{-2}$

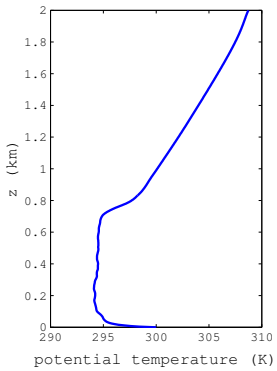

(b) $H_0 = 925.92\ \mathrm{Wm}^{-2}$

Figure 5.18: Average potential temperature along the center of the heat island for (a) $H_0 = 462.96\ \mathrm{Wm}^{-2}$ and (b) $H_0 = 925.92\ \mathrm{Wm}^{-2}$ at $t \in [3\ \mathrm{h}, 6.5\ \mathrm{h}]$.

5.2.7 Internal wave generation

In this section, the internal waves due to penetrative convection are investigated in the stable atmosphere which is overlying the mixed layer during the daytime. Vertical velocity is fluctuated inside the mixed layer and this fluctuation penetrates the upper stable atmosphere which creates internal waves in the stable atmosphere. In Figure 5.19a and 5.19c, the evolution of vertical velocity at different heights of the center of the heat island is presented for $H_0 = 462.96\ \mathrm{Wm}^{-2}$ and $H_0 = 925.92\ \mathrm{Wm}^{-2}$, respectively. Vertical velocity is fluctuated inside the mixed layer and penetrates the upper stable layer, which creates internal waves in the free atmosphere. A better illustration of the internal waves generated by penetrative convection is shown in Figure 5.19b and 5.19d for $H_0 = 462.96\ \mathrm{Wm}^{-2}$ and $H_0 = 925.92\ \mathrm{Wm}^{-2}$, respectively.

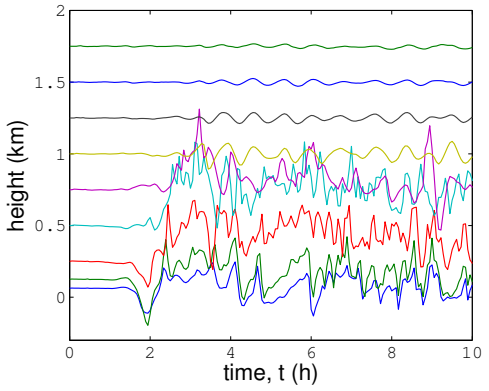

(a) $H_0 = 462.96\ \mathrm{Wm}^{-2}$

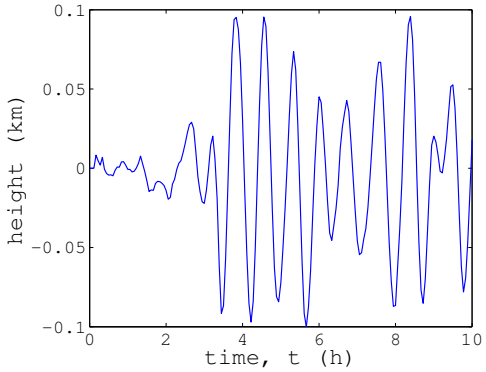

(b) $H_0 = 462.96\ \mathrm{Wm}^{-2}$, $z = 1.5$ km

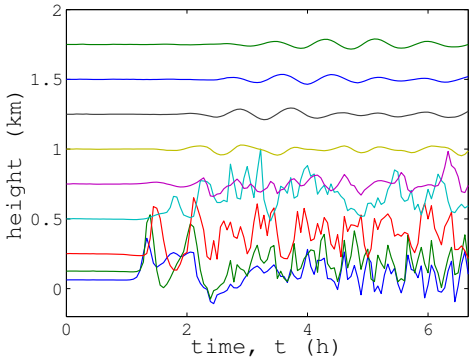

(c) $H_0 = 925.92\ \mathrm{Wm}^{-2}$

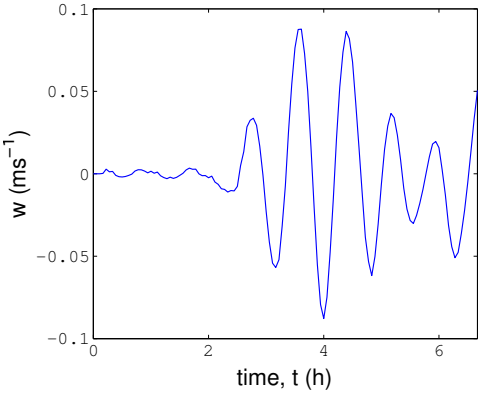

(d) $H_0 = 925.92\ \mathrm{Wm}^{-2}$, $z = 1.5$ km

Figure 5.19: Generation of internal waves. (Left) Evolution of vertical velocity at different heights along the center of the heat island. (Right) Internal wave at height $z = 1.5$ km where (a) (b) $H_0 = 462.96\ \mathrm{Wm}^{-2}$ and (c) (d) $H_0 = 925.92\ \mathrm{Wm}^{-2}$.

5.2.8 Energy balance

The normalized energy curves are presented in this section. Energy curves of the case of surface heat fluxes, $H_0 = 28.93, 57.87, 115.74, 231.48, 462.96$ and $925.92\ \mathrm{Wm}^{-2}$ are shown in Figure 5.20. In each curve, kinetic energy initially increases to peak and carry vertically away from the mixed layer by the internal waves. Since the earth's surface is continuously being heated during the daytime, the system gains energy as well. As a result, potential energy also increases upto a certain time and it reaches a peak, and in time it is converted to the kinetic energy. The normalized kinetic and potential energy curves of $H_0 = 28.93, 57.87, 115.74$, $231.48, 462.96$, and $925.92\ \mathrm{Wm}^{-2}$ are first intersect at $2.13, 2.97, 3.36,\ 4.82, 5.66, 5.97$ h, respectively. The total energy curve is also shown in Figure 5.20. After around two hours, the heat island circulation is fully generated then the total energy is balanced for $H_0 \leq 231.48\ \mathrm{Wm}^{-2}$. For the larger surface heat flux $462.96\ \mathrm{Wm}^{-2}$, the conversion of potential energy is higher than the case of small surface heat flux after reaching the peak.

5.3 Summary

Penetrative turbulence has been investigated for a differentially heated large horizontal area for $28.93\ \mathrm{Wm}^{-2} \leq H_0 \leq 925.92\ \mathrm{Wm}^{-2}$. Flow regimes are strongly dependent on the difference of surface heat flux between the city and the rural surroundings. Analyzing the coherent vorticities, it can be concluded that the flow is laminar for $28.93\ \mathrm{Wm}^{-2} \leq H_0 \leq 115.74\ \mathrm{Wm}^{-2}$, laminar-turbulent transition for $H_0 = 231.48 - 462.96\ \mathrm{Wm}^{-2}$, and fully turbulent for $H_0 = 925.92\ \mathrm{Wm}^{-2}$. Flow regimes are also strongly dependent on the thermal stratification. The flow becomes more turbulent for a large constant vertical potential temperature gradient. Flow regimes have been simulated without any artificial

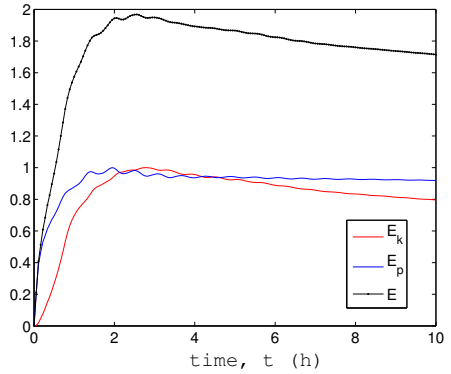

(a) $H_0 = 28.93\ \mathrm{Wm}^{-2}$

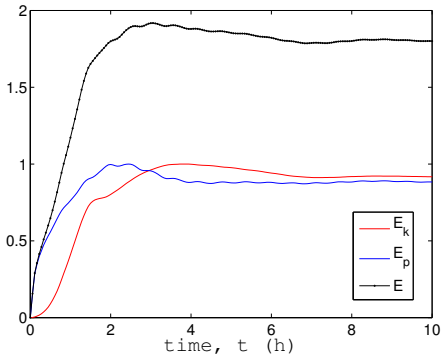

(b) $H_0 = 57.87\ \mathrm{Wm}^{-2}$

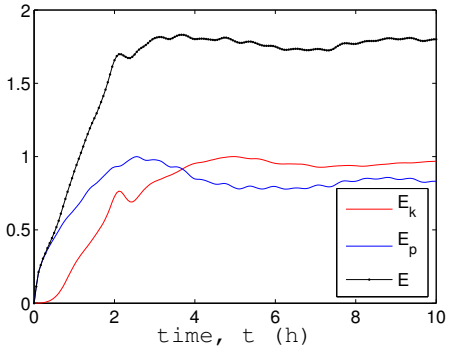

(c) $H_0 = 115.74\ \mathrm{Wm}^{-2}$

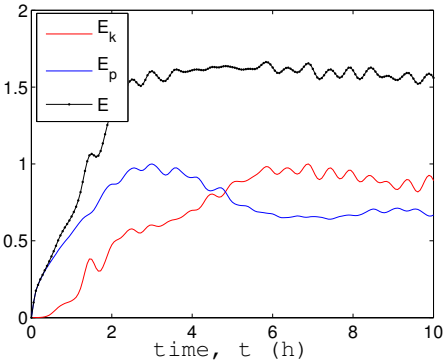

(d) $H_0 = 231.48\ \mathrm{Wm}^{-2}$

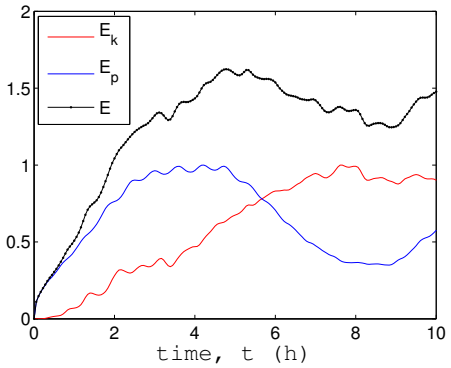

(e) $H_0 = 462.96\ \mathrm{Wm}^{-2}$

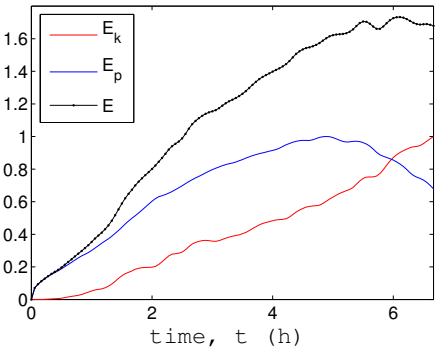

(f) $925.92\ \mathrm{Wm}^{-2}$

Figure 5.20: Energy curves for (a) $H_0 = 28.93\ \mathrm{Wm}^{-2}$, (b) $H_0 = 57.87\ \mathrm{Wm}^{-2}$, (c) $H_0 = 115.74\ \mathrm{Wm}^{-2}$, (d) $H_0 = 231.48\ \mathrm{Wm}^{-2}$, (e) $H_0 = 462.96\ \mathrm{Wm}^{-2}$ and (f) $925.92\ \mathrm{Wm}^{-2}$ at $\beta = 10\ \mathrm{K/km}$ and $t \in [0, 10\ \mathrm{h}]$.

treatment at the boundaries, and two types of boundary conditions and their effects have been described. For the turbulent mixing, a time series of potential temperature has been investigated and the vertical profiles of potential temperature have been depicted in which mixed layer heights appear at that place where the flow is turbulent. Due to the penetration of turbulence in the stable layer, internal waves appear in the stable atmosphere which transfer energy from ABL to the free atmosphere.

In the next chapter, the present research is summarized, and the future research directions are described, where this present work can be extended and implemented.

Chapter 6

Concluding remarks and future work

In this final chapter, the results of this thesis are reviewed and an outline is given for some future directions that can extend the ideas presented in this thesis.

6.1 Conclusion

The main conclusions can be divided into two parts: the development of a numerical and mathematical model, and the investigation of penetrative turbulence with this model.

A novel approach to filtering mesoscale dynamics based on Deslauriers-Dubac wavelet is studied in this thesis. A novel numerical methodology is developed to investigate nonhydrostatic mesoscale atmospheric phenomena where partial derivatives have been discretized with a weighted residual collocation method that is based on the interpolating scaling functions and wavelets, and a fully implicit time integration scheme has been studied. The numerical model has been validated through the solution of the advection-diffusion equation, which exhibits no visible oscillation. We have published this computational methodology for two-dimensional fluid flow (see, Alam *et al.*, 2014). In the present model, atmospheric phenomena have been investigated without using any artificial treatment near the bound-

aries. All numerical simulations support large CFL numbers.

In Chapter 4 and 5, the developed numerical model for investigating nonhydrostatic atmospheric phenomena has been implemented to investigate penetrative turbulence, which is validated through benchmark simulations. This atmospheric phenomenon has been investigated in two ways. In Chapter 4, penetrative turbulence has been investigated for a relatively isolated buoyant element, and in Chapter 5, it has been investigated for a differentially heated large horizontal area. In Chapter 4, it has been observed that the convective velocity of the flow does not depend on eddy viscosity. However, in Chapter 5 it has been observed that the convective velocity of the flow depends on the difference of surface heat flux between the urban and the rural areas. It has been concluded that the flow is stationary, laminar, symmetric, and no turbulent effect is visible for low surface heat flux ($28.93\ \mathrm{Wm}^{-2} \leq H_0 \leq 115.74\ \mathrm{Wm}^{-2}$), laminar-turbulent transition for $H_0 = 231.48 - 462.96\ \mathrm{Wm}^{-2}$, and for large surface heat flux ($H_0 = 925.92\ \mathrm{Wm}^{-2}$), airflow shows vertical turbulent mixing in the UHI region and then spreads in the rural areas. This turbulent flow has been observed from the coherent structure of vorticities, and mixed layer height has been observed in the turbulent region. On the other hand, thermal bubble rising in a neutrally stratified atmosphere exhibits chaotic mixing which is a representative of turbulent mixing. Furthermore, the thermal bubble placed in the stable atmosphere cannot exhibit turbulence due to the stability of the atmosphere, which kills turbulence.

Another important investigation in this study is the conservation of energy. Excellent energy conservation has been observed with the simulation of a penetrative convection flow for a neutrally stratified environment. Energy conservation has also been observed for a stably stratified environment and the energy curves are correlated with internal waves in which a portion of the kinetic energy has been transferred to the upper layer of the atmosphere due to internal waves.

Finally, the generation of internal waves has been investigated for the stable atmo-

sphere, which appears to be due to the penetrative convection for both forms of penetrative turbulence. A warm thermal perturbation in the stable atmosphere overshoots the air parcel in the atmosphere, which generates internal waves and, according to linear theory, those waves are characterized by evanescent wave. These waves are damping oscillatory and the damping factor depends on the buoyancy frequency. These internal waves die out when the bulk Richardson number Ri_b is larger than the critical value $Ri_b = 0.25$, and when Ri_b is less than the critical value, waves can propagate in the upper layers in the atmosphere.

Note that I have compromised the three-dimensional simulation with a two-dimensional one due to the high computational cost of 3D simulations. The development of 3D code is in progress, with parallel programming. Moreover, the presented two dimensional simulations have excellent agreement with benchmark simulations in which energy containing large eddies is captured.

6.2 Future research directions

This thesis provides potential feedback on constructing fast multiresolution algorithms for simulating nonhydrostatic mesoscale flows in a dry atmosphere.The next extension of this present work is to extend the discretization methodology to three-dimensional fluid flows as well as to extend it for moist atmospheric flow in any complex terrain and large scale atmospheric circulation. However, an advanced data structure, a parallel computing algorithm and a multilevel solution methodology are needed for three-dimensional simulations.

Bibliography

ALAM, J. & ISLAM, M. R. 2015 A multiscale eddy simulation methodology for the atmospheric ekman boundary layer. *Geophysical & Astrophysical Fluid Dynamics* **109** (1), 1–20.

ALAM, J. M. 2011 Towards a multiscale approach for computational atmospheric modelling. *Mon. Wea. Rev.* **139**, 3906–3922.

ALAM, J. M., WALSH, R. P., HOSSAIN, M. A. & ROSE, A. M. 2014 A computational methodology for two-dimensional fluid flows. *Int. J. Numer. Meth. Fluids* **75(12)**, 835–859.

ANSORGE, C. & MELLADO, J. P. 2014 Global intermittency and collapsing turbulence in the stratified planetary boundary layer. *Boundary-Layer Meteorol.* **153**, 89–116.

ATKINS, N. 2006 Atmospheric instability and cloud development - convection. http://apollo.lsc.vsc.edu/classes/met130/notes/chapter6/lift_convect.html, last updated: September 13, 2006.

BAIK, J.-J., KIM, Y.-H. & CHUN, H.-Y. 2001 Dry and moist convection forced by an urban heat island. *Journal of applied meteorology* **40** (8), 1462–1475.

BAIK, J. J., KIM, Y. H., KIM, J. J. & HAN, J. Y. 2007 Effects of boundary-layer stability on urban heat island-induced circulation. *Theor. Appl. Climatol.* **89**, 73–81.

BATCHELOR, G. K. 1967 *An introduction to fluid dynamics*. Cambridge University Press.

BERRUT, J. P. & TREFETHEN, L. N. 2004 Barycentric lagrange interpolation. *SIAM Rev.* **46(3)**, 501–517.

BILLANT, P. & CHOMAZ, J. M. 2000 Experimental evidence for a new instability of a vertical columnar vortex pair in a strongly stratified fluid. *J. Fluid Mech.* **418**, 167–188.

BLUMEN, W., BANTA, R., BURNS, S. P., FRITTS, D. C., NEWSOM, R., POULOS, G. S. & SUN, J. 2001 Turbulence statistics of a kelvin-helmholtz billow event observed in the night-time boundary layer during the cooperative atmosphere-surface exchange study field program. *Dynamics of Atmospheres and Oceans* **34**, 189–204.

BRYAN, G. H. & FRITSCH, J. M. 2002 A benchmark simulation for moist nonhydrostatic numerical models. *Mon. Wea. Rev.* **130**, 2917–2928.

C3HEADLINES 2012 Turkish scientists confirm uhi effect is overstating global warming - 4 degree uhi impact documented. http://www.c3headlines.com/2012/09/turkish-scientists-confirm-uhi-effect-is-overstating-global-warming-html, accessed September 12, 2012.

CARPENTER, R. L. J., DROEGEMEIER, K. K., WOODWARD, P. R. & HANE, C. E. 1990 Application of the piecewise parabolic method(ppm) to meteorological modelling. *Mon. Wea. Rev.* **118**, 586–612.

DANILOV, S. D. & GURARIE, D. 2000 Quasi-two-dimensional turbulence. *Physics-Uspekhi.* **43(9)**, 863–900.

DEARDORFF, J. W. 1970 A numerical study of three-dimensional turbulent channel flow at large reynolds numbers. *J. Fluid Mech.* **41(2)**, 453–480.

DEARDORFF, J. W., WILLIS, G. E. & LILLY, D. 1968 Laboratory investigation of a non-steady penetrative convection. *J. Fluid Mech.* **35**, 7–31.

DEFANT, F. 1951 Local winds. *Compendium of Meteorology, Amer. Meteor. Soc.* pp. 655–672.

DELAGE, Y. & TAYLOR, P. 1970 Numerical studies of heat island circulations. *Boundary-Layer Meteorology* **1** (2), 201–226.

DESLAURIERS, G., DUBOIS, J. & DUBUC, S. 1991 Multidimensional iterative interpolation. *Canadian Journal of Mathematics* **43**, 297–312.

DESLAURIERS, G. & DUBUC, S. 1989 Symmetric iterative interpolation process. *Constructive Approximation* **5**, 49–68.

DUBOIS, T. & TOUZANI, R. 2009 A numerical study of heat island flows: Stationary solutions. *Int. J. Numer. Meth. Fluids* **59**, 631–655.

DURRAN, D. R. 1989 Improving the anelastic approximation. *J. Atmos. Sci.* **46 (11)**, 1453–1461.

FAVRE-MARINET, M. & TARDU, S. 2013 *Convective Heat Transfer*. John Wiley & Sons.

FERNANDO, H. J. S. & HUNT, J. R. 1996 Some aspects of turbulence and mixing in stably stratified layers. *Dynamics of Atmospheres and Oceans* **23**, 35–62.

FINLAYSON, B. A. 1972 *The Method of Weighted Residuals and Variational Principles*. Academic Press.

GOLDING, W. L. 2002 Turbulence and its impact on commercial aviation. *Journal of Aviation/Aerospace Education & Research* **11**, 19–29.

GRIMMOND, C. S. B. & OKE, T. R. 2002 Turbulent heat fluxes in urban areas: observations and a local-scale urban meteorological parameterization scheme (lumps). *J. Appl. Meteor* **41**, 792–810.

GURVICH, A. S. & KUKHARETS, V. P. 2008 Horizontal and oblique spectra of temperature fluctuations in a stably stratified troposphere. *Atmos. Ocean. Phys.* **44(6)**, 773–778.

HOLFORD, J. M. & LINDEN, P. F. 1999 Turbulent mixing in a stratified fluid. *Dynamics of Atmospheres and Oceans* **30**, 173–198.

KANNAN, R. & WANG, Z. J. 2012 A high order spectral volume solution to the burgers' equation using the hopf-cole transformation. *Int. J. Numer. Meth. Fluids* **69(4)**, 781–801.

KELLY, J., GIRALDO, F. & CARR, L. 2009 Fully-implicit jacobian-free newton-krylov solvers for the nonhydrostatic euler equations. In *AGU Fall Meeting Abstracts*, , vol. 1, p. 0392.

KIMURA, R. 1975 Dynamics of steady convections over heat and cool islands. *J. Meteor. Soc. Japan* **53**, 440–457.

KNOLL, D. A. & KEYES, D. E. 2004 Jacobian-free newton-krylov methods: a survey of approaches and applications. *J. Comput. Phys.* **193(2)**, 357–397.

KUNDU, P. K., COHEN, I. M. & DOWLING, D. R. 2012 *Fluid Mechanics*, 5th edn. Elsevier.

LANE, T. P. 2008 The vortical response to penetrative convection and the associated gravity-wave generation. *Atmospheric Science Letters* **9**, 103–110.

LAUER, A., BENNARTZ, R., HAMILTON, K. & WANG, Y. 2012 Modeling the response of marine boundary layer clouds to global warming: The impact of subgrid-scale precipitation formation. *J. Climate* **25**, 6610–6626.

LIAO, W. 2010 A fourth-order finite-difference method for solving the system of two-dimensional burgers' equations. *Int. J. Numer. Meth. Fluids* **64(5)**, 565–590.

LIGDA, M. G. H. 1951 Radar storm observations. in compendium of meteorology. *Amer. Meteor. Soc.* pp. 1265–1282.

LILLY, D. K. 1966 *On the application of the eddy viscosity concept in the inertial sub-range of turbulence*. National Center for Atmospheric Research.

LILLY, D. K. 1983 Stratified turbulence and the mesoscale variability of the atmosphere. *J. Atmos. Sci.* **40**, 749–761.

LIN, Y. L. 2007 *Mesoscale Dynamics*. Cambridge University Press.

LINDBORG, E. 2006 The energy cascade in a strongly stratified fluid. *Journal of Fluid Mechanics* **550**, 207–242.

LU, J., ARYA, S. P., SNYDER, W. H. & LAWSON JR, R. E. 1997*a* A laboratory study of the urban heat island in a calm and stably stratified environment. part i: Temperature field. *Journal of Applied Meteorology* **36** (10), 1377–1391.

LU, J., ARYA, S. P., SNYDER, W. H. & LAWSON JR, R. E. 1997*b* A laboratory study of the urban heat island in a calm and stably stratified environment. part ii: Velocity field. *Journal of Applied Meteorology* **36** (10), 1392–1402.

MAHRT, L. 1999 Stratified atmospheric boundary layers. *Boundary-Layer Meteorol.* **90**, 375–396.

MALLAT, S. 2009 *A wavelet tour of signal processing*. Academic Press.

MALLAT, S. G. 1989 Multiresolution approximations and wavelet orthonormal bases of ðİŘ£^{2} (ðİŚĚ). *Transactions of the American Mathematical Society* **315** (1), 69–87.

MARTIN, C. & PIELKE, R. A. 1983 The adequacy of the hydrostatic assumption in sea breeze modeling over flat terrain. *J. Atmos. Sci.* **40**, 1472–1481.

MOENG, C.-H. 1984 A large-eddy-simulation model for the study of planetary boundary-layer turbulence. *Journal of the Atmospheric Sciences* **41** (13), 2052–2062.

MORTON, B. R., TAYLOR, G. & TURNER, J. S. 1956 Turbulent and gravitational convection from maintained and instaneous sources. *Proceedings of the Royal Society of London* **A234**, 1–23.

NINO, H. & MORI, A. 2005 Flow regimes of nonlinear heat island circulation. *J. Atmos. Sci.* **63**, 1538–1547.

OGURA, Y. 1962 Convection of isolated masses of buoyant fluid: a numerical calculation. *J. Atmos. Sci.* **19**, 492–502.

OGURA, Y. & PHILLIPS, N. A. 1962 Scale analysis of deep and shallow convection in the atmosphere. *J. Atmos. Sci.* **19**, 173–179.

ORLANSKI, I. 1975 A rational subdivision of scales for atmospheric processes. *Bull. Amer. Meteor. Soc.* **56**, 527–30.

ORTEGA, J. & RHEINBOLDT, W. 1970 *Iterative solution of nonlinear equations in several variables*. Boston: Academic Press.

PIELKE, R. A. 2002 *Mesoscale Meteorological Modeling*, 2nd edn. Academic Press.

PIELKE, R. A., COTTON, W. R., WALKO, R. L., TREMBACK, C. J., LYONS, W. A., GRASSO, L. D., NICHOLLS, M. E., MORAN, M. D., WESLEY, D. A., LEE, T. J. & COPELAND, J. H. 1992 A comprehensive meteorological modeling system-rams. *Meteor. Atmos. Phys.* **49**, 69–91.

RANJAN, R. & PANTANO, C. 2013 A collocated method for the incompressible navier–stokes equations inspired by the box scheme. *Journal of Computational Physics* **232** (1), 346–382.

RICHIARDONE, R. & BRUSASCA, G. 1989*a* Numerical experiments on urban heat island intensity. *Quarterly Journal of the Royal Meteorological Society* **115** (488), 983–995.

RICHIARDONE, R. & BRUSASCA, G. 1989*b* Numerical experiments on urban heat island intensity. *Q. J. R. Meteorol. Soc.* **115**, 983–995.

SAITO, K., ISHIDA, J., ARANAMI, K., HARA, T., SEGAWA, M. T., NARITA, M. & HONDA, Y. 2007 Nonhydrostatic atmospheric models and operational development at jma. *J. Met. Soc. Japan* **85B**, 271–304.

SENOCAK, I., ACKERMAN, A., KIRKPATRICK, M., STEVENS, D. & MANSOUR, N. 2007 Study of near-surface models for large-eddy simulations of a neutrally stratified atmospheric boundary layer. *Bound. -Lay. Meteorol.* **124**, 405–424.

SKAMAROCK, W. C., KLEMP, J. B., DUDHIA, J., GILL, D. O., BARKER, D. M., WANG, W. & POWERS, J. G. 2005 A description of the advanced research wrf version 2. *Tech. Rep.*. DTIC Document.

SMAGORINSKY, J. 1963 General circulation experiments with the primitive equations: I. the basic experiment*. *Monthly weather review* **91** (3), 99–164.

STULL, R. B. 1976 Internal gravity waves generated by penetrative convection. *Journal of the Atmospheric Sciences* **33** (7), 1279–1286.

STULL, R. B. 1988 *An Introduction to Boundary Layer Meteorology*, , vol. 13. Springer.

SUBICH, C. J., LAMB, K. G. & STASTNA, M. 2013 Simulation of the navier–stokes equations in three dimensions with a spectral collocation method. *International Journal for Numerical Methods in Fluids* **73** (2), 103–129.

SWELDENS, W. 1998 The lifting scheme: A construction of second generation wavelets. *SIAM Journal on Mathematical Analysis* **29** (2), 511–546.

SWELDENS, W. & SCHRÖDER, P. 1996 Building your own wavelets at home. *ACM SIGGRAPH course notes* .

TAPP, M. C. & WHITE, P. W. 1976 A non-hydrostatic mesoscale model. *Quart. J. Roy. Meteor. Soc.* **102**, 277–296.

TAYLOR, G. I. 1915 Eddy motion in the atmosphere. *Philosophical Transactions of the Royal Society of London.* **A215**, 1–26.

TORN, R. 2014 Atm 418: Dynamic meteorology iii. http://www.atmos.albany.edu/daes/atmclasses/atm418/atmosphere_scales.png, last updated: Fall, 2006.

TRIPOLI, G. J. 1992 A nonhydrostatic mesoscale model designed to simulate scale interaction. *Mon. Wea. Rev.* **120**, 1342–1359.

TUNG, K. K. & ORLANDO, W. W. 2003 The k^{-3} and $k^{-5/3}$ energy spectrum of atmospheric turbulence: Quasigeostrophic two-level model simulation. *J. Atmos. Sci.* **60**, 824–835.

UEDA, H. 1983 Effects of external parameters on the flow field in the coastal region-a linear model. *Journal of Climate and Applied Meteorology* **22** (2), 312–321.

WAITE, M. L. & BARTELLO, P. 2004 Stratified turbulence dominated by vortical motion. *Journal of Fluid Mechanics* **517**, 281–308.

WICKER, L. J. & SKAMAROCK, W. C. 1998 A time-splitting scheme for the elastic equations incorporating second-order runge-kutta time differencing. *Mon. Wea. Rev.* **126**, 1992–1999.

WINTERS, K. B. & YOUNG, W. R. 2009 Available potential energy and buoyancy variance in horizontal convection. *J. Fluid Mech.* **629**, 221–230.

WYNGAARD, J. C. 2004 Toward numerical modeling in the terra incognita. *Journal of the atmospheric sciences* **61** (14), 1816–1826.

XIA, H., BYRNE, D., FALKOVICH, G. & SHATS, M. 2011 Upscale energy transfer in thick turbulent fluid layers. *Nature Physics* **7** (4), 321–324.

XIE, S., LI, G., YI, S. & HEO, S. 2010 A compact finite difference method for solving burgers' equation. *Int. J. Numer. Meth. Fluids* **62(7)**, 747–764.

ZHANG, N., WANG, X. & PENG, Z. 2014 Large-eddy simulation of mesoscale circulations forced by inhomogeneous urban heat island. *Boundary-Layer Meteorol.* **151**, 179–194.

ZHU, H., SHU, H. & DING, M. 2010 Numerical solutions of two-dimensional burgers equations by discrete adomian decomposition method. *Comput. Math. Appl.* **60(3)**, 840–848.